Microstructured reactors for a portable hydrogen production unit

Microstructured Reactors for a Portable Hydrogen Production Unit

PROEFSCHRIFT

ter verkrijging van de graad van doctor aan de
Technische Universiteit Eindhoven, op gezag van de
Rector Magnificus, prof.dr.ir. C.J. van Duijn, voor een
commissie aangewezen door het College voor
Promoties in het openbaar te verdedigen
op donderdag 2 juni 2005 om 16.00 uur

door

Erik René Delsman

geboren op 12 juni 1976 te Amsterdam

Dit proefschrift is goedgekeurd door de promotoren:

prof.dr.ir. J.C. Schouten
en
prof.dr. G.J. Kramer

Copromotor:
dr. M.H.J.M. de Croon

CIP-DATA LIBRARY TECHNISCHE UNIVERSITEIT EINDHOVEN

Delsman, Erik R.

Microstructured Reactors for a Portable Hydrogen Production Unit /
by Erik R. Delsman. –
Eindhoven : Technische Universiteit Eindhoven, 2005.
Proefschrift. – ISBN 90-386-3036-0
NUR 913
Trefwoorden: chemische technologie / chemische reactoren ; microreactoren / brandstofcellen / waterstofbereiding / katalytische oxidatie ; koolmonoxide / methanol / fysisch-chemische simulatie en modellering ; gasdynamica / warmteoverdracht / duurzame ontwikkeling ; hernieuwbare energie
Subject headings: chemical engineering / chemical reactors ; microreactors / fuel cells / hydrogen production / steam reforming ; methanol / catalytic oxidation ; carbon monoxide / physiochemical simulation and modelling ; gas dynamics / heat transfer / sustainable development ; renewable energy

Cover page design: Jos Noijen
Cover photographs: Energy Research Center of the Netherlands, Institut für Mikrotechnik Mainz GmbH, Madan Bindraban
Printed by: Ridderprint Offsetdrukkerij B.V.

Contents

Summary

Microreactors are miniaturized chemical reaction systems, which contain reaction channels with a typical diameter of 10 to 500 µm. The small channel dimensions lead to a relatively large surface area-to-volume ratio and increased driving forces for heat and mass transport. Therefore, microreactors are especially suited for fast reactions with a large heat effect, where they allow for nearly isothermal conditions at high reactant concentrations, or for operation in the explosive regime, which is not possible in large-scale equipment. Microreactors also show large promise in the development of miniature chemical devices, where several unit operations are integrated with microstructured sensors and actuators to form a micro chemical plant.

Microreactors can also be used to convert liquid or gaseous fuels, like methanol or methane, to a hydrogen-rich gas, which can be used in fuel cell to produce electricity. Integrated fuel processor and fuel cell systems have promising applications as power supplies for portable electronic devices, and as electricity generators in the residential and recreational sectors. The driver for research in this area is the potentially much higher energy density of fuel cell systems as compared to batteries, allowing for longer stand-alone operation times. Fuel cell systems also provide benefits over small internal combustion engines in being more efficient and producing less noise and pollution.

In this study, a 100 W-electric methanol fuel processor is designed that consists of three microstructured, heat-integrated devices in series: a vaporizer–exhaust gas cooler, a reformer–burner, and a preferential oxidation–heat exchanger device. After evaporation of the fuel, a methanol-water mixture, the methanol and water react in the reformer over a $Cu/ZnO/Al_2O_3$ catalyst to produce hydrogen and carbon dioxide. The heat required for this reaction is provided by catalytically burning the left-over hydrogen from the fuel cell. In the reformer also a small amount of carbon monoxide is formed, which is removed in the preferential oxidation–heat exchanger device, by oxidation with air over a platinum-based catalyst. The clean hydrogen-rich gas is then used in a proton exchanger membrane fuel call to generate electricity.

Two preferential oxidation–heat exchanger prototypes are designed and manufactured that both consist of two heat exchangers and a cooled reactor integrated in a single microstructured device. The devices consist of stacks of stainless steel plates, in which flow distribution chambers and parallel microchannels are etched with a diameter of about 300 µm. The improved second prototype has a volume of 60 cm^3 and is able to reduce the carbon monoxide concentration in a methanol reformate gas to the required level of 10 ppm. Due to the small reactor dimensions, heat conductivity through the reactor material is a dominant factor determining the temperature profile. Furthermore, heat transfer to adjacent device parts and heat losses to the environment are hard to avoid. A design approach is developed that aims to establish equal flow rates and temperature profiles in the parallel microchannels, resulting in an improved performance of the microdevice.

Three-dimensional fluid dynamics simulations of the fluid flow distribution over a set of parallel microchannels show that two distinct flow regimes exist in the flow distribution chambers, depending on the gas inlet velocity. At low flow rates the flow distribution is completely determined by wall friction, while at flow rates above a transitional velocity, inertia effects start to influence the flow distribution. Based on elementary statistics, equations are derived for estimating the influence of flow maldistribution and manufacturing tolerances on microreactor performance. The equations express the microreactor conversion explicitly as a function of the variance of a number of channel parameters, viz. the channel flow rate, the channel diameter, the amount of catalyst in a channel, and the channel temperature. Although the influence of small variations in the channel flow rate and channel diameter on the reactor conversion is shown to be limited, variations in the catalyst coating thickness and in the channel temperature may significantly affect the reactor conversion.

Finally, a comparative design study of conventional fixed-bed reactor technology and microreactor technology shows that, on 100 W_e and 5 kW_e power output scales, the microreactor designs of the reformer–burner reactor and the preferential oxidation device outperform the conventional designs, leading to lower reactor volumes and weights. Although validity of these results is limited, the results show that microreactor technology may be a viable alternative for conventional technology for the design of small-scale reactors in which heat exchange is important.

Samenvatting

Microreactoren zijn geminiaturiseerde chemische systemen die reactiekanalen bevatten met een typische diameter van 10 tot 500 µm. De kleine kanaaldimensies zorgen voor een relatief grote oppervlakte-volume verhouding en extra drijvende krachten voor warmte- en stoftransport. Microreactoren zijn daarom speciaal geschikt voor snelle reacties met een groot warmteeffect, waar ze nagenoeg isotherme condities toestaan bij hoge reactantconcentraties, of voor het uitvoeren van reacties in het explosieregime, hetgeen op grote schaal niet mogelijk is. Microreactoren hebben ook een veelbelovende toepassing in de ontwikkeling van geminiaturiseerde chemische apparaten, waarin verscheidene unit-operaties geïntegreerd worden met microscopisch kleine sensors en aansturingen tot een klein chemisch fabriekje.

Microreactoren kunnen ook toegepast worden om vloeibare of gasvormige brandstoffen, zoals methanol of methaan, om te zetten in een waterstofrijk gas dat in een brandstofcel gebruikt kan worden om elektriciteit op te wekken. Geïntegreerde brandstof-omvormings en brandstofcelsystemen kunnen toegepast worden als stroombron voor draagbare elektronische apparaten en als generatoren voor de residentiële en recreatieve sector. Onderzoek in dit gebied wordt gedreven door de potentieel veel grotere energiedichtheid van brandstofcelsystemen in vergelijking met batterijen, waardoor een apparaat langer kan werken zonder te hoeven worden opgeladen. Brandstofcelsystemen hebben ook voordelen boven kleine verbrandingsmotoren, aangezien ze efficiënter, geluidsarmer en schoner zijn.

In dit onderzoek wordt een methanol-omzettingseenheid ontworpen voor een 100 W brandstofcel, die bestaat uit drie warmtegekoppelde microgestructureerde apparaten in serie: een verdamper–afgas koeler, een reformer–verbrander en een preferentiële oxidatie–warmtewisselaar unit. Na verdamping van de brandstof, een methanol-water mengsel, reageren methanol en water in de reformer met behulp van een $Cu/ZnO/Al_2O_3$ katalysator tot waterstof en kooldioxide. De warmte die nodig is voor deze reactie, wordt geleverd door katalytische verbranding van de overgebleven waterstof van de brand-

stofcel. In de reformer wordt ook een kleine hoeveelheid koolmonoxide gevormd, welke in de preferentiële oxidatie–warmtewisselaar unit wordt verwijderd door middel van oxidatie met lucht over een selectieve platinakatalysator. Het schone, waterstofrijke gas kan vervolgens in een brandstofcel omgezet worden in elektriciteit.

Er zijn twee prototypes van de preferentiële oxidatie–warmtewisselaar unit ontworpen, die beide bestaan uit twee warmtewisselaars en een gekoelde reactor geïntegreerd in een enkele microgestructureerde unit. De prototypes bestaan uit een stapel roestvrijstalen plaatjes waar stromingsverdelingskamers en parallelle kanalen in zijn geëtst met een diameter van ongeveer 300 µm. Het verbeterde, tweede prototype heeft een volume van 60 cm^3 en is in staat om de koolmonoxideconcentratie in een methanol reformaatgas te verwijderen tot het vereiste niveau van 10 ppm. Vanwege de kleine reactorafmetingen is warmtegeleiding door het reactormateriaal een belangrijke factor die het temperatuurprofiel in de reactor beïnvloedt. Ook is het daardoor niet eenvoudig om warmteoverdracht tussen aangrenzende delen van de unit en warmteverliezen naar de omgeving te voorkomen. De prestaties van de microgestructureerde unit is verbeterd door gebruik te maken van een ontwerpstrategie gericht op het bereiken van een gelijke stromingsverdeling over de parallelle kanalen en een gelijk temperatuursprofiel in deze kanalen.

Dynamische, driedimensionale stromingssimulaties van de verdeling van een gasstroom over een set parallelle microkanalen tonen aan, dat er, afhankelijk van de instroomsnelheid, verschillende stromingsregimes bestaan in de stromingsverdelingskamers. Bij lage instroomsnelheden wordt de stroming volledig bepaald door wrijving met de wanden, terwijl boven een bepaalde snelheid de inertia van het gas de stromingsverdeling gaat beïnvloeden. Op basis van elementaire statistiek zijn mathematische vergelijkingen afgeleid om de invloed van een ongelijk verdeelde stroming en van toleranties in de fabricage op de prestaties van een microreactor af te schatten. Deze vergelijkingen drukken de conversie van een microreactor expliciet uit als functie van de variantie in enkele kanaalparameters, zoals de stroomsnelheid door een kanaal, de kanaaldiameter, de hoeveelheid afgezette katalysator en de kanaaltemperatuur. Hoewel de invloed van een kleine variantie in de stroomsnelheid en kanaaldiameter beperkt is, kunnen verschillen in dikte van de katalysatorcoating en in de kanaaltemperatuur een significant effect hebben op de reactorconversie.

Tenslotte wordt met een vergelijkende ontwerpstudie tussen conventionele vastbed reactortechnologie en microreactor technologie aangetoond, dat, op een 100 W_e en 5 kW_e schaal, de microreactor ontwerpen van de reformer–verbrander en de preferentiële oxidatie unit kleiner en lichter zijn dan hun conventionele equivalenten. Hoewel de geldigheid van deze resultaten beperkt is, geven deze resultaten wel aan dat microreactortechnologie een alternatief kan zijn voor conventionele technologie voor het ontwerpen van kleine reactoren waarin warmteoverdracht een belangrijke rol speelt.

1 Introduction

Abstract

This chapter starts with a short introduction to the relatively new field of microstructured reactors. The advantages and disadvantages will be briefly stated as well as the main differences between microreactors and conventional macro-scale equipment. Subsequently the reader will be introduced to the possibility to use a fuel cell in combination with a fuel processor as an alternative for battery packs to power portable electronic equipment. Microreactor technology will play a key role in the development of a small and lightweight fuel processor unit. Finally, the European cooperation project MiRTH-e, of which this research has been a part, is mentioned followed by the aim and layout of this thesis.

1.1 Microstructured reactors

Microstructured reactors, also called microreactors, are miniaturized reaction systems that are, at least partially, produced using methods of microtechnology or precision engineering [1]. Typically, microreactors contain fluid channels with a diameter between 10 and 500 µm, see Figure 1.1, which results in a relatively large surface area-to-volume ratio and increased driving forces for heat and mass transport [2, 3]. One of the first microstructured devices was reported in literature in 1989 [4]. Microreactor Engineering has been recognized as a new discipline since the first workshop on Microsystems Technology for Chemical and Biological Microreactors, held in Germany in 1995 [5]. Since then many research groups have entered the field. Several reviews of the field have already appeared in books and papers [1, 6–8].

Due to their small diameter, microchannels have very good heat and mass transfer properties. Therefore, the rate of reactions that are limited by heat or mass transfer in a conventional reactor, can be increased by performing the reaction in a microreactor, leading to process intensification [9]. Furthermore, nonuniformities in temperature (in the case of fast, highly exothermic reactions [10–12]) or concentration (when the reactants have to be mixed in the reactor [13, 14]) can be avoided in a microreactor, which can result in improved selectivity and yield. The temperature uniformity also makes microreactors well suited for measuring intrinsic reaction kinetics [11, 15].

Microchannels also have a small volume. When used as a measurement or analysis device, this leads to less consumption of space, materials, and energy, and, in combination with fast heat and mass transfer, also to a shorter analysis time [16]. These qualities resulted in a large interest in microreactors for high throughput experimentation [17, 18]. The small inventory also makes microreactors safer for handling dangerous chemicals [19]. The flame arrestor capabilities of the small channels can be used to make an intrinsically safe reactor for handeling explosive reaction mixtures [20, 21]. This enables performing reactions under conditions that used to be inaccessible and that might lead to increased selectivity and yield and can avoid the use of large diluent streams.

A third microreactor property is its modular nature. Scaling-up a process by using a large number of small units, identical to those used in the laboratory, avoids the uncertainties involved in the design of a new process or,

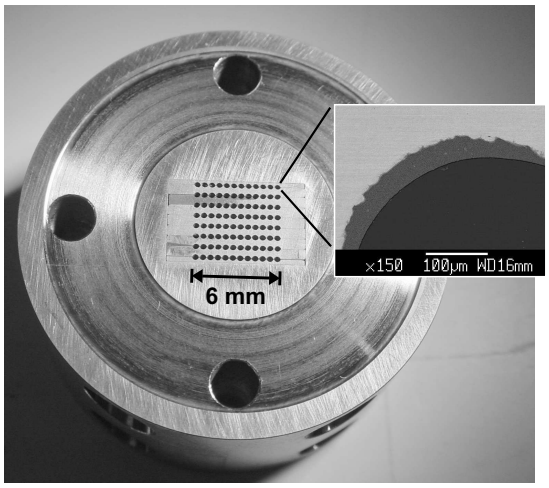

Figure 1.1: Example of a microreactor containing 96 microchannels with a diameter of 400 µm and a length of 1.5 cm. The inlay shows a detail of a single microchannel coated with a 35 µm thick catalyst layer.

in case of a pharmaceutics product, avoids a lengthy new licensing procedure, which can significantly shorten the time-to-market of a new product [6]. Furthermore, the modular nature of microreactors also facilitates distributed production, where (possibly dangerous) chemicals are being made at the place where they are needed, in this way avoiding the transportation risks and costs [22, 23].

The short residence time (milliseconds to seconds range) makes microreactors less suitable for slow reactions that require a residence time of minutes or even hours [24]. In general, microreactors are also relatively expensive, as they operate against the 'economy of scale' by replacing a large reactor by many small ones [6]. Furthermore, microreactors are more vulnerable to corrosion and erosion [5], and require very clean fluids to be used to avoid blockage of the microchannels [25].

Microreactors also differ from conventional reactors in a number of ways, which are of importance for the development of mathematical reactor models [8]. Reactor modelling is an important aspect of chemical engineering, since it is the basis for the design and optimization of chemical process equipment. Since the flow in microreactors is often laminar, the accuracy of microreactor models can be higher than of conventional reactors, which makes the design of microreactors potentially more reliable. The main differences between microreactors and macro-scale equipment are:

1. The flow in microstructures is often laminar, whereas flow in macro-scale

equipment is usually turbulent.
2. Heat and mass transfer across boundaries is very fast in microreactors, while it is often a limiting factor in conventional reactors.
3. The volume fraction of solid wall material is much higher in microreactors than in macroscopic equipment, which makes solid heat conduction an important factor in microreactors, while it can usually be neglected in conventional reactors.
4. Small reactors are more sensitive to their outside environment than larger units.
5. The large surface area-to-volume ratio of the microstructures results in an increased importance of surface effects over volumetric effects.

1.2 Fuel cells and fuel processors

Fuel cells are regarded as a promising alternative for battery packs in portable electronic devices, given the much higher energy density of fuel cell systems [26]. Fuel cells are able to convert chemical energy directly to electricity with a high conversion efficiency. The fuel cell was invented by Sir William Grove already in 1839, but its application is still confined to only a few niche markets. During the last decades, the fuel cell performance has been improved up to a level where large-scale introduction of fuel cells in the market seems to become possible. The breakthrough of fuel cell technology at the consumer market, however, will largely depend on the development of an easy, safe, and cheap way to deliver the fuel to the cell.

The best fuel for a fuel cell is hydrogen gas. However, no good solution is still available for the storage of hydrogen, either as a liquid, as pressurized gas, or in the form of metal hydrides [27]. Liquefaction of hydrogen requires a large amount of energy (about half of the energy contained by the hydrogen itself) and the need for hydrogen venting will lead to additional losses during storage. Storage as a compressed gas requires very high pressures in the order of 1000 bar, which also requires a large energy input as well as strong, lightweight storage containers. The use of metal hydrides is hindered by slow hydrogen desorption kinetics, the need for a heat input to release the hydrogen, and the large weight of the hydride materials.

The in-situ generation of clean hydrogen from a liquid fuel like methanol offers an attractive alternative to hydrogen storage [28]. Figure 1.2 shows a

typical flow sheet of a fuel processor and fuel cell system. The system consists of a fuel vaporizer and a fuel reformer, where the fuel is converted to hydrogen. Besides hydrogen usually also carbon dioxide and carbon monoxide are formed. Since carbon monoxide is a severe poison for the fuel cell anode catalyst, the formed carbon monoxide needs to be removed. This is done in the preferential oxidation reactor by oxidation with air over a selective catalyst. The clean hydrogen-rich gas then enters the fuel cell, where it reacts with oxygen to produce electricity. The left-over hydrogen from the fuel cell is used in the catalytic burner to provide heat for the vaporization and reforming steps. For portable applications the fuel-processing unit has to be small and lightweight. Therefore, in the development of such a unit, microreactor technology will play a key role [29].

1.3 The MiRTH-e project

The research described in this thesis was part of a project funded by the European Commission as part of the Fifth Framework Programme for Research and Development under the name *Micro Reactor Technology for Hydrogen and Electricity* (MiRTH-e) [30]. The project objective was to design, micro-fabricate, and test a miniaturized, integrated fuel processor for the conversion of methanol to clean, fuel cell-grade hydrogen for low-power electricity generation (20–100 W_e). The fuel processor unit should be small, light-weight, and energy efficient. The technical project targets are summarized in Table 1.1. The combination of fuel processor and fuel cell should provide a five to ten-fold improvement of the energy density, as compared to battery packs and hydrogen storage in metal hydrides. Since the units have to be used in consumer applications, high standards are set for the allowable emissions of the fuel processor and fuel cell combination. Furthermore, the units should have a sufficient life time and the production costs should be low enough to allow

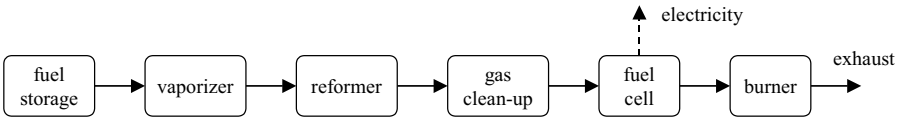

Figure 1.2: Schematics of a fuel processor – fuel cell system.

Table 1.1: Technical targets of the MiRTH-e fuel processor and fuel cell system.

Power range	20–100 W_e
Volume fuel processor	< 500 cm^3
Efficiency (methanol to electricity)	35% (at full load)
System energy density	> 3 MJ/kg (> 800 Wh/kg)
Emissions	low enough to allow for indoor use
Life time	$> 40{,}000$ hrs
Cost of fuel processor unit	$< 2{,}000$ euro (professional market)
(mass production)	< 200 euro (consumer market)

for competitive pricing.

Within the MiRTH-e project six research groups from industry and academia cooperated. The MESA$^+$ Research Institute from the Twente University and the Laboratoire des Sciences du Génie Chimique (CNRS-ENSIC) have focussed mainly on the development of a fuel vaporization unit using silicon-based technology. The Institut für Mikrotechnik Mainz GmbH (IMM), the Netherlands Energy Research Foundation (ECN), and the Eindhoven University of Technology (TU/e) have focussed on the development of the catalytic reformer and gas clean-up units using stainless steel as reactor material. Shell Global Solutions was involved as project coordinator.

1.4 Aim and lay-out of the thesis

This thesis describes the research work at the TU/e related to the MiRTH-e project, which is directed at the development of a microstructured fuel cell feed gas clean-up device. Besides the actual designing and experimental characterization of the gas clean-up device, the research is also concerned with developing guidelines for the design of microstructured reactors. Each chapter is written as a research paper and can be read separately from the rest of this thesis. Consequently, some information will be presented multiple times throughout the thesis.

Chapter 2 provides an introduction to fuel processor systems and the use of methanol as a fuel for such systems. Subsequently, an optimized system design is made of a 100 W_e methanol fuel processor and fuel cell (FP-FC) system. An exergy analysis is performed on the FP-FC system to determine the

system efficiency and to indicate possibilities for improving the system. Finally, the efficiency of the FP-FC system is compared to battery systems and combustion engines in terms of system efficiency.

In Chapters 3 and 4 two prototype gas clean-up units, the preferential oxidation (Prox) microdevices, are discussed. The Prox devices consist of two microstructured heat exchangers and a preferential oxidation microreactor that are integrated in a single miniaturized device. The design of the microdevices is based on a separate modelling of the fluid flow distribution and the heat and mass transfer in the device. The heat and mass transfer calculations are simplified using volume averaging over the reactor volume. The microdevice prototypes are tested in an experimental setup for their performance in terms of carbon monoxide conversion and heat recovery efficiency.

The design of the flow distribution chambers is discussed in detail in Chapter 5. Based on computational fluid dynamics modelling, the distribution chamber geometry is optimized to establish an even distribution of fluid flow over the microchannels. An even flow distribution is important to ensure a high performance of the microdevice.

Subsequently, in Chapter 6 mathematical correlations are derived that express the effect of differences between microchannels, in terms of fluid flow rate, channel diameter, and catalyst coating thickness, on the reactor conversion and selectivity. The correlations are useful for quantification of the effect that channel differences have on microreactor performance, and for defining appropriate manufacturing tolerances for microreactor design.

Finally, in Chapter 7 a methanol reformer and gas clean-up unit are designed using both microreactor technology and conventional fixed-bed technology. These designs are then compared on system volume and weight for a 100 W_e and a 5 kW_e system. This exercise gives information on differences between the technologies and whether the use of microtechnology does indeed result in smaller, more intensified chemical reactors.

Bibliography

[1] W. Ehrfeld, V. Hessel, and H. Löwe. *Microreactors: new technology for modern chemistry*. Wiley-VCH, Weinheim, Germany, 2000.

[2] H. Löwe and W. Ehrfeld. State-of-the-art in microreaction technology:

concepts, manufacturing and applications. *Electrochim. Acta*, 44:3679–3689, 1999.

[3] K. F. Jensen. Microreaction engineering — is small better? *Chem. Eng. Sci.*, 56:293–303, 2001.

[4] K. Schubert, W. Bier, G. Linder, and D. Seidel. Herstellung und Test von kompakten Mikrowärmeüberträgern. *Chem. Ing. Tech.*, 61:172–173, 1989.

[5] G. Ondrey. Microreactor engineering: birth of a new discipline? *Chem. Eng.*, 102:52, 1995.

[6] W. Ehrfeld, V. Hessel, and V. Haverkamp. *Microreactors, Ullmann's encyclopedia of industrial chemistry*. Wiley-VCH, Weinheim, Germany, 1999.

[7] A. Gavriilidis, P. Angeli, E. Cao, K. K. Yeong, and Y. S. S. Wan. Technology and applications of microengineered reactors. *Chem. Eng. Res. Des.*, 80:3–30, 2002.

[8] V. Hessel, S. Hardt, and H. Löwe. *Chemical Micro Process Engineering — Fundamentals, Modelling and Reactions*. Wiley-VCH, Weinheim, Germany, 2004.

[9] A. I. Stankiewicz and J. A. Moulijn. Process intensification: transforming chemical engineering. *Chem. Eng. Prog.*, 96:22–34, 2000.

[10] H. Kestenbaum, A. Lange de Oliveira, W. Schmidt, F. Schüth, W. Ehrfeld, K. Gebauer, H. Löwe, T. Richter, D. Lebiedz, I. Untiedt, and H. Züchner. Silver-catalyzed oxidation of ethylene to ethylene oxide in a microreaction system. *Ind. Eng. Chem. Res.*, 41:710–719, 2002.

[11] E. V. Rebrov, S. A. Duinkerke, M. H. J. M. de Croon, and J. C. Schouten. Optimization of heat transfer characteristics, flow distribution, and reaction processing for a microstructured reactor/heat-exchanger for optimal performance in platinum catalyzed ammonia oxidation. *Chem. Eng. J.*, 93: 201–216, 2003.

[12] G. Kolb and V. Hessel. Micro-structured reactors for gas phase reactions. *Chem. Eng. J.*, 98:1–38, 2004.

[13] J. B. Knight, A. Vishwanath, J. P. Brody, and R. H. Austin. Hydrodynamic focusing on a silicon chip: mixing nanoliters in microseconds. *Phys. Rev. Lett.*, 80:3863–3866, 1998.

[14] S. J. Haswell, R. J. Middleton, B. O'Sullivan, V. Skelton, P. Watts, and P. Styring. The application of micro reactors to synthetic chemistry. *Chem. Commun.*, pages 391–398, 2001.

[15] R. S. Besser, X. Ouyang, and H. Surangalikar. Hydrocarbon hydrogenation and dehydrogenation reactions in microfabricated catalytic reactors. *Chem. Eng. Sci.*, 58:19–26, 2002.

[16] A. Manz, N. Graber, and H. M. Widmer. Miniaturized total chemical analysis systems: a novel concept for chemical sensing. *Sens. Actuators B*, 1:244–248, 1990.

[17] T. Zech and D. Hönicke. Efficient and reliable screening of catalysts for microchannel reactors by combinatorial methods. In J. Baselt, W. Ehrfeld, K.-P. Jaeckel, I. Rinard, and R. Wegeng, editors, *Proceedings of the Fourth International Conference on Microreaction Technology*, pages 379–

389. AIChE, New York, 2000.

[18] A. Müller, K. Drese, H. Gnaser, M. Hampe, V. Hessel, H. Löwe, S. Schmitt, and R. Zapf. Fast preparation and testing methods using a microstructured modular reactor for parallel gas phase catalyst screening. *Catal. Today*, 81:377, 2002.

[19] D. C. Hendershot. Process minimization: making plants safer. *Chem. Eng. Prog.*, 96:35–40, 2000.

[20] M. Janicke, A. Holzwarth, M. Fichtner, K. Schubert, and F. Schüth. A microstructured catalytic reactor/heat exchanger for the controlled catalytic reaction between H_2 and O_2. *Stud. Surf. Sci. Catal.*, 130:437–442, 2000.

[21] G. Veser. Experimental and theoretical investigation of H_2 oxidation in a high-temperature catalytic microreactor. *Chem. Eng. Sci.*, 56:1265–1273, 2001.

[22] R. S. Benson and J. W. Ponton. Process miniaturisation—a route to total environmental acceptability? *Chem. Eng. Res. Des.*, 71:160–168, 1993.

[23] S. K. Ajmera, M. W. Losey, and K. F. Jensen. Microfabricated packed-bed reactor for distributed chemical synthesis: The heterogeneous gas phase production of phosgene as a model chemistry. *AIChE J.*, 47:1639–1647, 2001.

[24] S. Hasebe. Design and operation of micro-chemical plants—bridging the gap between nano, micro and macro technologies. *Comput. Chem. Eng.*, pages 57–64, 2004.

[25] O. Wörz, K.-P. Jäckel, T. Richter, and A. Wolf. Microreactors—a new efficient tool for reactor development. *Chem. Eng. Technol.*, 24:138–142, 2001.

[26] C. Hebling, A. Heinzel, D. Golombowski, T. Meyer, M. Müller, and M. Zedda. Fuel cells for low power applications. In W. Ehrfeld, editor, *Proceedings of the Third International Conference on Microreaction Technology*, pages 383–393. Springer, Berlin, Germany, 2000.

[27] L. Zhou. Progress and problems in hydrogen storage methods. *Renewable Sustainable Energy Rev.*, 9:395–408, 2005.

[28] W. Dönitz. Fuel cells for mobile applications, status, requirements and future application potential. *Int. J. Hydrogen Energy*, 23:611–615, 1998.

[29] J. D. Holladay, Y. Wang, and E. Jones. Review of developments in portable hydrogen production using microreactor technology. *Chem. Rev.*, 104:4767–4790, 2004.

[30] MiRTH-e: Micro reactor technology for hydrogen and electricity. Project funded by the European Commission under the 'Energy, Environment and Sustainable Development' programme, contract number ENK6-CT-2000-00110, Dec. 2000 – Nov. 2003.

Exergy analysis of a methanol fuel processor and fuel cell system

2

This chapter is based on the papers:

E.R. Delsman, C.U. Uju, M.H.J.M. de Croon, J.C. Schouten, and K.J. Ptasinski. Exergy analysis of an integrated fuel processor and fuel cell system. *Energy J.*, submitted.

E.R. Delsman, E.V. Rebrov, M.H.J.M. de Croon, J.C. Schouten, G.J. Kramer, V. Cominos, T. Richter, T.T. Veenstra, A. van den Berg, P.D. Cobden, F.A. de Bruijn, C. Ferret, U. d'Ortona, and L. Falk. MiRTH-e: Micro Reactor Technology for Hydrogen and Electricity. In M. Matlosz, W. Ehrfeld, and J.P. Baselt, editors, *Proceedings of the Fifth International Conference on Microreaction Technology*, pages 268–274. Springer Verlag, Berlin, Germany, 2001.

Abstract

Fuel cells have great application potential as stationary power plants, as power sources in transportation, and as portable power generators for electronic devices. Most fuel cells currently being developed for use in vehicles and as portable power generators require hydrogen as a fuel. Chemical storage of hydrogen in liquid fuels is considered to be one of the options for supplying hydrogen to the fuel cell. In this case a fuel processor is needed to convert the liquid fuel into a hydrogen-rich stream. This paper presents a second-law analysis of an integrated fuel processor and fuel cell system. Several primary fuels are compared on their theoretical energy content. Subsequently, a methanol fuel processor is designed, based on a pinch analysis of the system. An exergy analysis is performed for the methanol fuel processor and fuel cell (FP-FC) system, producing 100 W of electricity. Finally, it is shown that the calculated overall exergetic efficiency of the FP-FC system is higher than that of typical combustion engines and rechargeable batteries.

2.1 Introduction

Fuel cells are expected to be a major component of future energy systems, offering increased energy efficiency and reduced environmental impact. The application potential of fuel cells ranges from stationary power plants to mobile power sources in vehicles as well as portable power generators [1]. Efficient autonomous low power generators are needed as alternative to batteries in a growing number of electric and electronic devices [2].

The Proton Exchange Membrane (PEM) fuel cell currently appears to be the preferred fuel cell for a variety of mobile applications, mainly due to its relatively low operating temperature and high efficiency. The fuel for the PEM fuel cell is hydrogen, since hydrogen has a high electrochemical reactivity and its reaction products create little environmental impact. However, the storage and transportation of hydrogen is still difficult, either in gaseous or liquid form, or when using additional storage media, like metal hydrides or carbon nanotubes [3, 4].

Chemical storage of hydrogen in liquid fuels is considered to be one of the most advantageous options for supplying hydrogen to fuel cells, especially for mobile applications. In this case a fuel processor (FP) is needed to convert the liquid fuel into a hydrogen-rich gas before it is fed to the fuel cell [5]. A variety of primary liquid fuels are considered, such as alcohols, hydrocarbons, and ammonia. The process of hydrogen generation from alcohols and hydrocarbons usually involves catalytic steam reforming or catalytic partial oxidation, whereas in the case of ammonia a catalytic cracking step is needed. Methanol or some other fuels, such as formic acid or medium-size hydrocarbons, can also be used directly in fuel cells, i.e. without a fuel processor. However, the power density and efficiency of these direct fuel cells is lower.

The purpose of this paper is to present a second-law analysis of an integrated FP-FC system. In the next section the maximum amount of electrical work available from a FP-FC system is evaluated for a number of primary fuels. Thereafter, the choice for methanol as primary fuel is explained. Subsequently, based on a pinch analysis, a system design is made for a methanol fuel processor integrated with a PEM-FC, of which, in Section 2.5, an exergy analysis is performed. Finally, the exergetic efficiency of the FP-FC system is compared with that of typical alternative power sources, such as rechargeable batteries and combustion engines.

2.2 Hydrogen generation from primary fuels

Figure 2.1 shows a block diagram of a fuel processor with methanol as the primary fuel. An aqueous solution of methanol from the storage tank is evaporated in the vaporizer. In the reformer, methanol reacts with steam in the presence of a catalyst to produce a hydrogen-rich gas, which also contains CO_2 and a small amount of CO. CO is a poison for the PEM-FC anode catalyst and its concentration in the PEM-FC feed gas should not be higher than 10–100 ppm [6]. Methanol itself and carbon dioxide also affect the fuel cell catalyst, but not as severe as carbon monoxide [7, 8]. In the gas clean-up step, CO is removed and the hydrogen-rich gas enters the fuel cell, where electricity is generated. The gas stream leaving the fuel cell usually still contains some hydrogen, which is combusted in the burner to deliver the heat needed in the vaporizer and the reformer.

The thermodynamic evaluation of the FP-FC system involves the calculation of the maximum amount of work available from this system. The maximum amount of work gives the theoretical energy density of a fuel in an ideally operating FP-FC system. The maximum amount of work available from the various fuels is equal to their Gibbs free energy change. Separately, the entropy change of the fuel oxidation is important, as it determines the heat effect in an ideal FP-FC system. However, the heat effect of an ideal conversion system is small compared to the maximum amount of work for all investigated fuels.

Table 2.1 presents the maximum amount of work available from the considered primary fuels, expressed in different units. The maximum amount of work available from the FP-FC system shows different values for various fuels when it is represented per mol, per kg, or per L of fuel. However, in the case of carbon containing compounds, the maximum amount of work per kmol C present in a fuel is approximately similar. Moreover, when the maximum amount of work produced in the FP-FC system is expressed per mol of

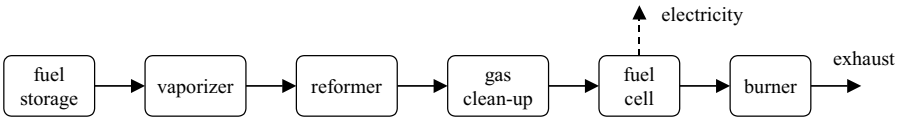

Figure 2.1: Schematics of a fuel processor – fuel cell system.

Table 2.1: Maximum amount of work for the conversion of primary fuels to electricity expressed in various units.

Fuel	Maximum amount of work				
	MJ/ mol fuel	MJ/ mol C in fuel	MJ/ mol H_2 via reforming	MJ/ kg fuel	MJ/ L fuel
Methanol (l)	-0.69	-0.69	-0.23	-22	-17[a]
Ethanol (l)	-1.30	-0.65	-0.22	-28	-22[a]
n-Octane (l)	-5.21	-0.65	-0.21	-46	-32[a]
Ammonia (l)	-0.33		-0.22	-19	-10[a]
Methane (g)	-0.80	-0.80	-0.20	-50	-3.9[b]
Hydrogen (g)	-0.23		-0.23	-113	-0.89[b]

[a]The density of the liquid fuels is calculated at 298 K and 1 bar, for ammonia at 10 bar.
[b]The density of the gaseous fuels is calculated at 298 K and 100 bar.

H_2 generated via steam reforming in the case of alcohols and hydrocarbons, and via catalytic cracking in the case of ammonia, it is approximately the same for each fuel. The practical efficiency of the FP-FC system will be lower. A comparison between various FP-FC systems has shown that the efficiency is about 40% and approximately equal for the hydrocarbon fuels and alcohols [9].

The maximum amount of work, shown in Table 2.1, also represents the theoretical energy density of a fuel, i.e. in an ideally operating FP-FC system. Pure hydrogen shows the highest value of the gravimetric energy density (113 MJ/kg fuel) followed by methane and n-octane (50 MJ/kg and 46 MJ/kg, respectively), and the remaining fuels have an energy density in the range of 19–28 MJ/kg. The corresponding energy density for state-of-the-art batteries such as Li-ion or Zn-air is much lower, about 1 MJ/kg [2]. Similarly, the volumetric energy density of typical fuels, such as n-octane and methanol (32 MJ/L fuel and 17 MJ/L, respectively) exceeds those of batteries (lower than 2 MJ/L). However, the volumetric energy density of the gaseous fuels is significantly lower than that of liquid fuels, which limits their use in mobile or portable systems.

2.3 Methanol as fuel

A suitable primary fuel for a mobile FP-FC system (for automotive or low-power applications) has to fulfill several selection criteria. The fuel should have a high energy content, be easy to handle (be liquefiable at moderate pressures), and be cheap. Furthermore, the fuel of choice should provide easy refueling, create little health, safety and environmental hazards, whereas the conversion process must be robust and easy to down-size [10].

Although the energy density of methanol is lower than that of gasoline or diesel fuels, methanol is a a promising liquid fuel candidate, since it can be reformed into hydrogen at a relatively low temperature ($\sim$ 250 °C), compared to 450–900 °C for all other common fuels, such as gasoline, ethanol etc. [11]. Since the composition of the product gas is affected by the water-gas shift equilibrium, operating at a lower temperature also decreases the CO formation during the reforming. This averts the use of a large water-gas-shift reactor, to reduce the CO content of the reformate gas, for methanol-based systems.

Furthermore, being a pure chemical fuel, methanol contains essentially no sulfur or other catalyst poisons. Methanol is also considered to be safer and more environmentally benign than gasoline, due to its rapid biodegradation [12]. Methanol can be produced from renewable sources (biomass), in which case it also is a sustainable fuel [13]. Drawbacks of methanol are the lack of infrastructure and its water solubility in combination with its toxicity [11].

For portable fuel cell applications, methanol is in direct competition with hydrogen stored in cylinders or as metal hydride [14]. The direct use of hydrogen eliminates the need for a reforming system, which considerably reduces the complexity of the system. However, the low (volumetric) energy density of stored hydrogen is a disadvantage. Furthermore, compression and liquefaction of gaseous hydrogen, as well as the release of hydrogen from a metal hydride, all require a large additional energy input, which reduces the system efficiency [4]. Liquefaction, for example, requires an amount of work equal to almost half of the lower heating value of hydrogen.

Much effort is currently also being put into the development of a direct methanol fuel cell (DMFC), which combines the better storage properties of methanol with the reduced system complexity of a direct fuel cell without the need for a reforming system. However, such direct operating fuel cells are

at the moment limited by the unwanted effects of fuel cross-over, poor long-term stability due to CO production in the FC, and lower power density and efficiency, as compared to a hydrogen fuelled proton exchange membrane fuel cell (PEMFC).

2.4 Methanol reforming system

A pinch analysis is made of a methanol fuel processor–fuel cell system, to study the system's feasibility and to point out the energy bottlenecks of the system. The analysis is based on the general process scheme in Figure 2.1. The methanol fuel processor consists of a vaporizer and three catalytic reactors. The vaporized methanol and water react in the reformer reactor at 250 °C using a Cu-based catalyst according to the following reactions:

$$CH_3OH + H_2O \rightarrow CO_2 + 3\,H_2 \qquad \Delta H = +48.8\ \text{kJ/mol} \tag{2.1}$$

$$CH_3OH \rightarrow CO + 2\,H_2 \qquad \Delta H = +89.2\ \text{kJ/mol} \tag{2.2}$$

$$CO + H_2O \rightleftarrows CO_2 + H_2 \qquad \Delta H = -41.0\ \text{kJ/mol} \tag{2.3}$$

Reaction (2.1) is the steam reforming reaction, reaction (2.2) is the methanol decomposition reaction, and reaction (2.3) is the water-gas shift reaction.

The hydrogen-rich gas from the reformer contains about 0.5% of CO, which has to be removed to avoid poisoning of the fuel cell's anode catalyst. This is accomplished in the preferential oxidation (Prox) reactor by oxidation with air over a supported noble metal catalyst at 150 °C. Two reactions take place, each with a selectivity of about 50%:

$$CO + \tfrac{1}{2}\,O_2 \rightarrow CO_2 \qquad \Delta H = -283\ \text{kJ/mol} \tag{2.4}$$

$$H_2 + \tfrac{1}{2}\,O_2 \rightarrow H_2O \qquad \Delta H = -242\ \text{kJ/mol} \tag{2.5}$$

Although in this process the amount of hydrogen that is removed is approximately equal to the amount of CO, this is acceptable as long as the amount of CO in the reformate gas remains low.

The CO-free hydrogen-rich gas is oxidized in the fuel cell to produce electricity. The leftover hydrogen from the fuel cell is combusted in the catalytic burner to provide the energy required for the endothermic reforming reaction and the vaporization. For the construction of the energy diagram, the electri-

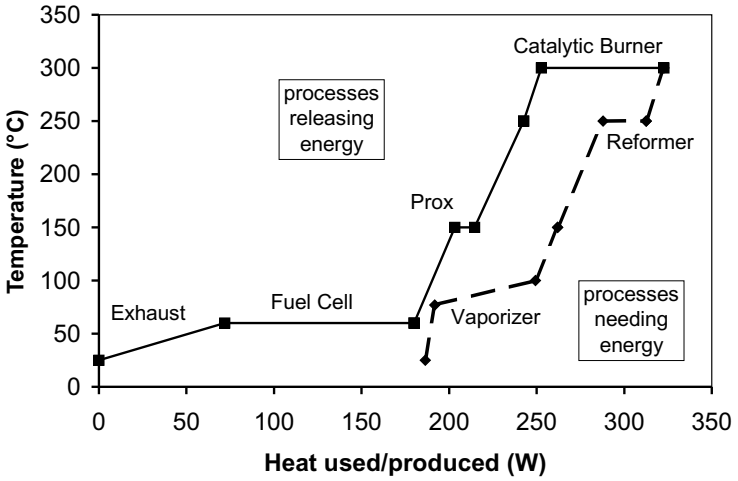

Figure 2.2: Pinch diagram of an integrated system consisting of a methanol fuel processor and a PEM fuel cell. The dashed line indicates endothermic processes, i.e. the feed vaporization and the reforming as well as several heating steps. The full line indicates exothermic processes: the catalytic burning, the preferential oxidation, the fuel cell conversion, and cooling steps. The leftmost part of the full line indicates the energy still present in the exhaust gas.

cal power output is set to 100 W_e with a fuel cell efficiency of 50%. An excess of water is used in the process to reduce the carbon monoxide formation in the reformer reactor and to avoid dehydration of the fuel cell. Water is not recycled in the system, but is introduced into the system together with the methanol. Although this dilution of the feed reduces its energy density, it also reduces the system's complexity, since it eliminates the need for a condenser in the system.

In the resulting pinch diagram, Figure 2.2, the amount of heat needed or produced in a specific process step is plotted against the temperature of that specific step, which is a measure for the quality of the energy. Processes that require heat are separated from processes that produce heat to determine whether the former processes can be supported by the latter. The conclusions to be drawn from this diagram are twofold. Most importantly, the system is feasible, i.e. enough energy is available at a high enough temperature to drive all endothermic processes. Secondly, most of the energy losses occur in the fuel cell. Unfortunately, this energy cannot be used in the process, since the fuel cell operates at a low temperature of 60 °C.

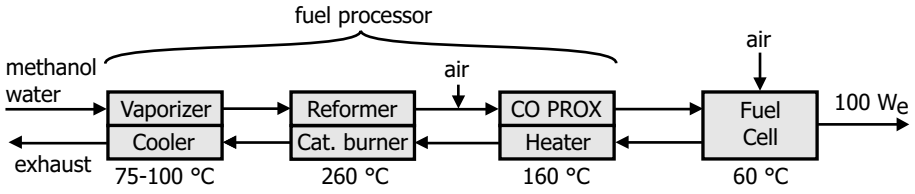

Figure 2.3: Energy integrated system lay-out of the methanol fuel processor – fuel cell system. The process is divided into three binary combinations of reactors and heat exchangers, which all operate at different temperatures.

The pinch diagram, Figure 2.2, also shows the most efficient way to couple the energy flows in the system, which is coupling the processes of comparable temperature. This leads to the division of the fuel processor into three separate units, as is shown in Figure 2.3. In this process scheme, the vaporizer is heated by the hot off-gases of the catalytic burner. The catalytic burner itself is coupled to the methanol reformer, to efficiently deliver the energy needed for the reforming reaction. The heat released from the preferential oxidation reaction is recovered by preheating the catalytic burner feed. The resulting design thus consists of three separate heat-integrated devices placed in series.

2.5 Exergy analysis

A detailed exergy analysis is performed for a methanol fuel processor integrated with a PEM fuel cell, for application as a portable power generator. The FP-FC system, which produces 100 W of electricity, has been simulated using the flow-sheeting program Aspen Plus. First, the process has been modelled and simulated for a standard set of conditions. Subsequently, the process conditions have been modified to determine the influence of the operating conditions on the overall efficiency of the system. Figure 2.4 shows the flow sheet of the FP-FC system (Figure 2.3) using elementary process units.

An aqueous solution of methanol (the molar ratio of methanol to water is 1:2 for the standard case) is evaporated in the vaporizer (VAP) at 150 °C. The vaporized methanol and water react in the reformer reactor (REF) at 250 °C using a Cu-based catalyst according to reactions (2.1)–(2.3). The steam reforming is an endothermic reaction and therefore an external heat supply is needed. The steam reformer is modelled as a Gibbs reactor, which assumes

chemical equilibrium between the species at the outlet of the reactor. At the reforming temperature of 250 °C the equilibrium conversion of methanol is almost 100%. The selectivity of methanol to CO_2 is about 97%, and to CO about 3%.

The H_2-rich gas from the reformer is mixed in the mixer (MIX) with a small quantity of air, which is needed for the oxidation of CO present in the product gas from the reformer reactor. To this end the gas mixture enters the preferential CO oxidation reactor (PCO). In this reactor oxygen reacts with both CO and hydrogen, reactions (2.4) and (2.5), over a Pt-based catalyst at 150 °C. The PCO reactor is modelled as a stoichiometric reactor where 50% of the supplied O_2 from the air is used for a complete oxidation of CO and the remaining 50% of O_2 reacts with H_2. Finally, the CO-free H_2-rich gas is oxidized in the PEM fuel cell (FC). The excess of O_2 from air used in the cell is assumed to be 80% with respect to reacting H_2.

The operating temperature of the PEM-FC is about 60 °C as calculated from a balance between water entering the fuel cell and formed in the cell, and water leaving the fuel cell as saturated vapor. The water flow rates into and out of the fuel cell have to be balanced, to avoid dehydration or flooding of the fuel cell. Water enters the fuel cell as part of the reformate gas and it is formed in the cathode reaction. The amount of water vapor leaving the cell is directly related to the operating temperature of the cell, when equilibrium is assumed between the exhaust gas and liquid water present in the cell. The conversion of H_2 in the cell is calculated based on the generation of 100 W of electricity and a LHV efficiency of the fuel cell of 50%. The fuel cell part of the FP-FC system is not modelled in detail. Instead a fixed efficiency is assumed.

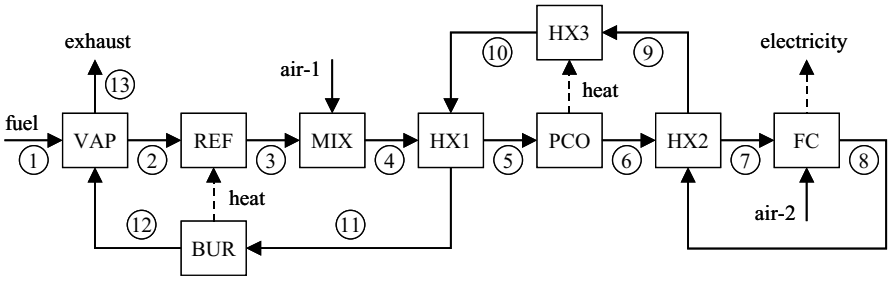

Figure 2.4: Flow sheet of the integrated fuel processor – fuel cell system (see the text for the abbreviations).

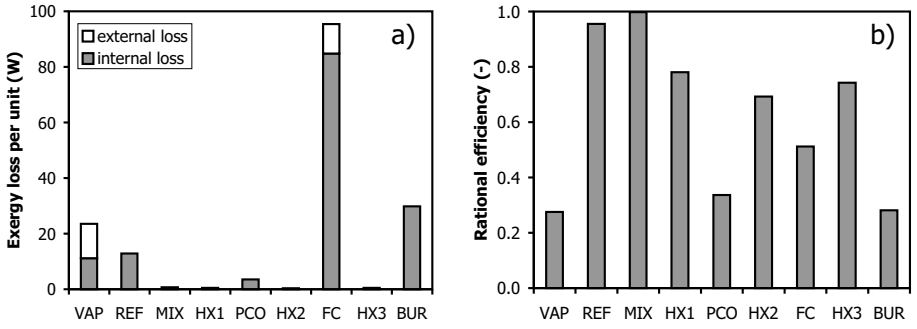

Figure 2.5: Exergy analysis results for the process units in the methanol FP-FC system. a) Internal and external exergy losses. b) Rational efficiencies.

Table 2.2: Heat and work transfer rates for the 100 W_e methanol FP-FC system at standard conditions (see also Figure 2.4).

Transfer rate of	VAP	REF	HX1	PCO	HX2	FC	HX3	BUR
Heat (W)	53	27	6	-6	5	-97	6	-27
Work (W)						-100		

The heat integration system consists of a catalytic burner reactor (BUR) and three heat exchangers (HX1, HX2, HX3). In the catalytic burner reactor the unconverted hydrogen is combusted to produce the heat necessary for the vaporizer and the reformer. In this case the FP-FC system operates autothermally.

The temperature, molar flow rate, and exergy flow rate, are calculated according to Szargut et al. [15], for the standard case. The amount of heat and work transferred in the various units is listed in Table 2.2. The results of the exergy analysis are presented in Figure 2.5. The total exergy loss is about 167 W and the contribution of internal and external exergy losses is 144 W and 23 W, respectively. The overall efficiency of the FP-FC system is 37%. This corresponds to a required methanol feed rate of 1 ml min^{-1}.

Figure 2.5a shows the internal and external exergy losses for all process units, which is an absolute measure to compare the losses per process unit. The external exergy losses only take place in the vaporizer (stream 13) and the fuel cell (heat losses); heat losses in the other process units are neglected. The main exergy losses occur in the fuel cell, burner, reformer, and vaporizer units. The exergy losses in the fuel cell are caused by activation polarization,

Table 2.3: Definition of the rational efficiency for all process units. E_i is the exergy flow rate represented by stream i (see Figure 2.4), E^{Q}_{unit} is the exergy content of the transferred heat to/from the unit (see Table 2.2), and W_{FC} is the electrical work produced in the fuel cell.

unit	VAP	REF	MIX	HX1	PCO
efficiency	$\frac{E_2 - E_1}{E_{12}}$	$\frac{E_3}{E_2 + E^{Q}_{\text{REF}}}$	$\frac{E_4}{E_3}$	$\frac{E_{11} - E_{10}}{E_4 - E_5}$	$\frac{E^{Q}_{\text{PCO}}}{E_5 - E_6}$

unit	HX2	FC	HX3	BUR
efficiency	$\frac{E_9 - E_8}{E_6 - E_7}$	$\frac{W_{\text{FC}}}{E_7 - E_8}$	$\frac{E_{10} - E_9}{E^{Q}_{\text{HX3}}}$	$\frac{E^{Q}_{\text{BUR}}}{E_{11} - E_{12}}$

ohmic losses, and concentration polarization [16]. In the vaporizer only physical exergy accounts for the losses there, mainly due to the high temperature difference between the hot and cold sides of the heat exchanger. In the reformer and burner both chemical and physical exergy losses occur. The sum of the exergy losses in the mixer, the PCO reactor, and the heat exchangers HX1, HX2, and HX3 is less than 5% of the total loss.

Figure 2.5b shows the rational efficiency of each process unit. The rational efficiency is defined as the ratio between the desired output of a process unit and the necessary input to this unit [17]. The performance expressed in terms of rational efficiency only shows the relative efficiency of individual system units and it is sensitive to the definition of the input and output streams. The used definitions for the unit efficiency are listed in Table 2.3.

The results show that the reformer and mixer perform very good in terms of relative efficiency, followed by the heat exchangers HX1, HX2, and HX3. The exergetic efficiency of the fuel cell is close to the LHV efficiency, which is 50% in this calculation, since the Gibbs free energy and the enthalpy change upon combustion are almost identical, as is the case for most fuels. The efficiency of the burner and PCO reactor is lower, since in both cases chemical exergy is converted to heat of a moderate temperature. The vaporizer efficiency is low, since in the vaporizer heat is transferred between two media with a relatively large temperature difference, and since the vaporizer efficiency also includes the external exergy loss by the exhaust gas. The exhaust gas exergy is mainly determined by the 20% of water vapor that is present. The use of a

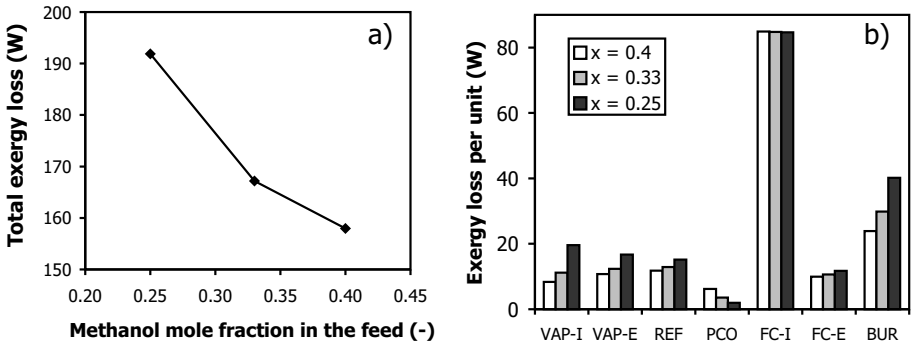

Figure 2.6: The influence of the methanol concentration in the feed on the exergy losses in the FP-FC system. a) total exergy loss, b) exergy losses per unit (I - internal, E - external).

Table 2.4: Effect of changes in various operating conditions on the total exergy losses in the FP-FC system.

Operating condition	Change	Total exergy loss
Methanol mole fraction in the feed	25 $\Rightarrow$ 40 %	192 $\Rightarrow$ 158 W
Reformer temperature	230 $\Rightarrow$ 270 °C	167 $\Rightarrow$ 157 W
Fuel cell temperature	60 $\Rightarrow$ 77 °C	167 $\Rightarrow$ 169 W
Fuel cell LHV efficiency	40 $\Rightarrow$ 60 %	234 $\Rightarrow$ 122 W

condenser and recycling of the water would reduce this exergy loss.

Based on the absolute exergy losses shown in Figure 2.5a, only the reformer, burner, vaporizer, and especially the fuel cell should be considered when optimizing the efficiency the overall FP-FC system. Therefore, the influence is studied of the following operating conditions on the overall exergy loss of the FP-FC system: the methanol concentration in the feed, the reformer temperature, the fuel cell temperature, and the LHV efficiency of the fuel cell. Figure 2.6a demonstrates that the total exergy loss decreases with an increasing methanol concentration in the feed. Almost all units contribute to this improvement (see Figure 2.6b), with the exception of the PCO reactor (the exergy losses in the fuel cell are assumed to be independent of the methanol feed concentration). When the methanol concentration is increased, the amount of water that has to be vaporized decreases and consequently also the amount of heat that has to be generated in the catalytic burner decreases.

The effects of changing several operating conditions of the FP-FC system

on the total exergy losses in this system are summarized in Table 2.4. The total exergy loss is hardly dependent of the reformer temperature in the range 230–270 °C and of the fuel cell temperature in the range 60–77 °C. Increasing the LHV-based efficiency of the fuel cell from 40 to 60% results in a substantial decrease of the total exergy loss from 234 to 123 W. Increasing the efficiency of the PEM-FC can be realized at the expense of a lower power density. In that case a larger fuel cell is needed, which is not practical for a small-scale application.

2.6 Comparison with batteries and combustion engines

Small FP-FC systems can find many applications as efficient and clean autonomous portable power generators. Applications of such systems include powering of portable electric and electronic devices, such as laptop computers and cell telephones. Currently, rechargeable batteries are the predominant technology in such applications. Another potential application of FP-FC systems is a mobile power generation for residential and recreational purposes, in which case FP-FC systems replace combustion engines, for example diesel generators on board of (sailing) yachts.

Different criteria can be used to compare FP-FC systems with rechargeable batteries and combustion engines. An important aspect, in addition to environmental impact, safety, and life-cycle cost, is efficient fuel utilization, especially for larger FP-FC systems. For small systems the energy density is also important, being higher for fuel cells than for batteries. Moreover, FP-FC systems have additional advantages over combustion engines, such as less sound generation and less pollution. In this section a comparison of the second-law efficiency is presented between the FP-FC system, rechargeable batteries, and small combustion engines, for the conversion of a chemical fuel to electrical and mechanical work. A value of 37% is used for the exergetic efficiency of the fuel-to-electricity conversion in a FP-FC system, as calculated in the previous section.

The exergetic efficiency of the energy conversion in rechargeable batteries has been evaluated for typical batteries, including Ni-MH, Ni-Cd, Li-ion, and lead-acid batteries. Battery efficiency has been calculated as the ratio of the

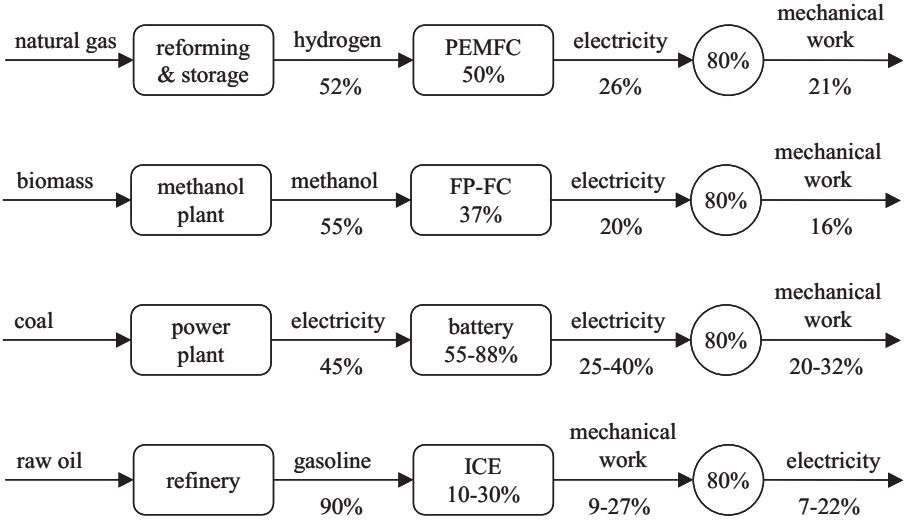

Figure 2.7: Comparison of the exergetic efficiency between a hydrogen PEM fuel cell system, a methanol FP-FC system, rechargeable batteries, and internal combustion engines (ICE's).

amount of energy released from the battery while discharging to the amount of energy delivered to the battery during charging. This results in a range of efficiencies between 55 and 88% (the lowest value for a Ni-Cd, the highest for a Li-ion battery) [18]. The exergetic efficiency of small-scale combustion engines, such as used for electricity generation, has been evaluated as a ratio between the engine power (mechanical work production) and the chemical exergy of the fuel. Typical fuels used in the considered combustion engines are gasoline and diesel. The calculated efficiency ranged between 10% for small engines (< 1 kW) to 30% for larger ones (~ 100 kW) [18].

Figure 2.7 shows a comparison between fuel cell systems, rechargeable batteries, and combustion engines for the energy conversion from primary fuels to electrical and mechanical work. Assumptions are made for the conversion efficiency of the primary to the secondary fuels or electricity. For the conversion of natural gas to hydrogen an efficiency of 78% is assumed [19] and for hydrogen storage 67% [4]. The efficiency of the production of methanol from biomass is 55% [13]. The efficiency of a power plant is 45% and of a refinery 90% [20]. The conversion efficiency between mechanical and electrical work is assumed to be 80%.

The results show that the battery systems have the highest fuel-to-electricity and fuel-to-mechanical energy efficiency compared to fuel cells and combustion engines. The combustion engine has the lowest efficiency for electricity generation, especially for smaller scales. The fuel cell system working on stored hydrogen performs better than the methanol FP-FC system, which is mainly due to the higher efficiency of the hydrogen production process compared to the methanol production process. Improvements still have to be made to the fuel cell systems and the production methods of hydrogen and methanol, before fuel cell systems are able to outperform the other systems on primary fuel efficiency. However, the differences between the systems are not dramatic and the ultimate choice between these systems for specific applications and scales will also depend on other factors, like energy density, system transient behavior, and costs.

2.7 Conclusions

Integrated fuel processor and fuel cell (FP-FC) systems have promising applications, particularly as man-portable power supplies in electronic and electric devices, as well as in residential and recreational sectors. Hydrogen is the superior fuel for fuel cells having the highest energy density per unit mass, but it is difficult to store. Various primary fuels like alcohols and hydrocarbons can be processed to obtain a hydrogen-rich gas. The maximum amount of work produced from various fuels is different, but it is approximately the same for each fuel when it is expressed per mol of hydrogen generated via steam reforming.

A system design is made of a 100 W_e methanol fuel processor and fuel cell system, consisting of three heat-integrated devices in series. An exergy analysis of the FP-FC system shows that the largest exergy losses occur in the fuel cell, the burner, the vaporizer, and the reformer. The overall exergetic efficiency of the system is about 37%. The total exergy loss depends predominantly on the methanol concentration in the feed and the fuel cell performance; the temperature in reformer and fuel cell have a much smaller effect. The calculated overall exergetic efficiency of the primary fuel-to-electricity conversion is higher for batteries than for fuel cell systems, which in turn have a higher efficiency than combustion engines.

Bibliography

[1] W. Dönitz. Fuel cells for mobile applications, status, requirements and future application potential. *Int. J. Hydrogen Energy*, 23:611–615, 1998.

[2] A. Mitsos, I. Palou-Rivera, and P.I. Barton. Alternatives for micropower generation processes. *Ind. Eng. Chem. Res.*, 43:74, 2004.

[3] J. M. Ogden. Prospects for building a hydrogen energy infrastructure. *Ann. Rev. Energy Environ.*, 24:227–279, 1999.

[4] L. Zhou. Progress and problems in hydrogen storage methods. *Renewable Sustainable Energy Rev.*, 9:395–408, 2005.

[5] C. Song. Fuel processing for low-temperature and high-temperature fuel cells. challenges and opportunities for sustainable development in the 21^{st} century. *Catal. Today*, 77:17–49, 2002.

[6] H.-F. Oetjen, V. M. Schmidt, U. Stimming, and F. Trila. Performance data of a proton exchange membrane fuel cell using H_2/CO as fuel gas. *J. Electrochem. Soc.*, 143:3838, 1996.

[7] K. R. Weisbrod and N. E. Vanderborgh. Effect of operating parameters and anode gas impurities upon polymer electrolyte fuel cells. In *Proceedings of the 29^{th} Intersociety Energy Conversion Engineering Conference (IECEC-94)*, pages 855–860. AIAA, Washington DC, USA, 1994.

[8] F. A. de Bruijn, D. C. Papageorgopoulos, E. F. Sitters, and G. J. M. Janssen. The influence of carbon dioxide on PEM fuel cell anodes. *J. Power Sources*, 110:117–124, 2002.

[9] C. Qi and J. Cross. Integrated fuel processor and PEM fuel cell system simulation and optimization. In *Proceedings of AIChE's Spring 2000 National Meeting*, pages 142–148. AIChE, Atlanta, USA, 2000.

[10] B. Lindström and L. J. Pettersson. Hydrogen generation by steam reforming of methanol over copper-based catalysts for fuel cell applications. *Int. J. Hydrogen Energy*, 26:923–933, 2001.

[11] L. F. Brown. A comparitive study of fuels for on-board hydrogen production for fuel-cell-powered vehicles. *Int. J. Hydrogen Energy*, 26:381–397, 2001.

[12] R. A. Lewis and G. Dolan. Challenges and opportunities in choosing methanol for fuel cell vehicles. In *Proceedings of AIChE's Spring 2000 National Meeting*, pages 136–141. AIChE, Atlanta, USA, 2000.

[13] C. N. Hamelinck and A. P. C. Faaij. Future prospects for production of methanol and hydrogen from biomass. *J. Power Sources*, 111:1–22, 2002.

[14] M. A. J. Cropper, S. Geiger, and D. M. Jollie. Fuel cells: a survey of current developments. *J. Power Sources*, 131:57–61, 2004.

[15] J. Szargut, D. R. Morris, and F. R. Steward. *Exergy analysis of thermal, chemical, and metallurgical processes*. Hemisphere, New York, 1988.

[16] R. Cownden, M. Nahon, and M. A. Rosen. Exergy analysis of a fuel cell power system for transportation applications. *Exergy Int. J.*, 1:112–121, 2001.

[17] The exergy method of thermal plant analysis. *The properties of gases and*

liquids. Krieger, Malabar, 1995.

[18] C. U. Uju. Exergy analysis and optimization of electricity generation from hydrogen and liquid fuels. Master's thesis, Eindhoven University of Technology, 2002.

[19] M. A. Rosen. Thermodynamic comparison of hydrogen production processes. *Int. J. Hydrogen Energy*, 21:349–365, 1996.

[20] W. van Gool. *Exergie en Energie – Toepassingen van het exergieconcept in procesanalyse en energiebeleid*. Van Gool ESE Consultancy, Driebergen, Netherlands, 1998. In Dutch.

Experiments and modelling of an integrated preferential oxidation–heat exchanger microdevice

3

This chapter has been published as:

E.R. Delsman, M.H.J.M. de Croon, G.J. Kramer, P.D. Cobden, C. Hofmann, V. Cominos, and J.C. Schouten. Experiments and modelling of an integrated preferential oxidation–heat exchanger microdevice. *Chem. Eng. J.*, 101:123–131, 2004.

Abstract

Microreactor technology creates opportunities for the development of miniature chemical devices, in which several unit operations are integrated. We describe in this paper the design, experimental, and modelling work concerning a microdevice for the preferential oxidation of carbon monoxide in hydrogen-rich reformate gas. The microdevice consists of two heat exchangers and one reactor, all integrated in a single stack of microstructured plates. Experiments show that the initial carbon monoxide conversion is high. However, the catalyst deactivates rapidly. It takes over one hour to reach the required reactor temperature during startup, which is too long for application in a portable fuel processor. The measured temperature gradients in the heat exchangers are twice as small as predicted by a one-dimensional heat exchange model of the microchannels. A two-dimensional model shows that large differences in temperature exist between channels close to the inlet and channels further from the inlet, causing the one-dimensional model to fail. This paper shows that for an accurate description of heat transfer in a micro heat exchanger, the complete (two-dimensional) plate geometry needs to be considered.

3.1 Introduction

In recent years microfabrication technologies are being introduced in the fields of chemistry and chemical process engineering to realize microchannel devices, e.g. mixers, heat exchangers, and reactors, with capabilities considerably exceeding those of conventional macroscopic systems [1, 2]. Microreactors have reaction channels with diameters of the order of 100–500 µm, a channel length of about 1 to 10 cm, and have an inherently large surface area-to-volume ratio. These properties offer clear advantages such as high mass and heat transfer rates, which is beneficial for attaining high selectivities and conversions and enables optimum control of temperature and residence time [3–5]. Microreactors also have a low hold-up, resulting in excellent controllability, small safety risks, and low environmental impact [6, 7]. This makes these micro reaction devices specifically suitable for highly exothermic reactions, short contact time reactions, and for the on-demand and safe production of toxic and hazardous chemicals.

Microreactors also show large promise in the development of miniature chemical devices, where several unit operations are integrated with microstructured sensors and actuators to form a micro chemical plant [8–10]. Integrating a variety of components in a small device asks for new design approaches and solutions for constructional issues, like for example connecting different kinds of materials, the integration of microstructured sensors and actuators, and the thermal separation of adjacent units, which operate at different temperatures. These miniaturized chemical devices offer opportunities for small scale fuel processing and portable power generation, for example to replace battery packs in laptops or mobile phones [11, 12]. Microreactors can be used to convert liquid or gaseous fuels, like methanol or methane, to hydrogen, which can be fed to a fuel cell to produce electricity. The challenge is to develop micro chemical systems in which all reaction and heat transport steps are optimally integrated, in combination with appropriate sensors and actuators for process monitoring and control.

Within the European Union funded project MiRTH-e [13], a miniaturized fuel-processing system is developed to generate hydrogen in-situ from a methanol–water mixture, to fuel a 100 W_e fuel cell. The fuel processing system consists of a steam reformer, which converts methanol and water to a hydrogen-rich gas, a preferential CO oxidation unit to remove the 0.5% of carbon monox-

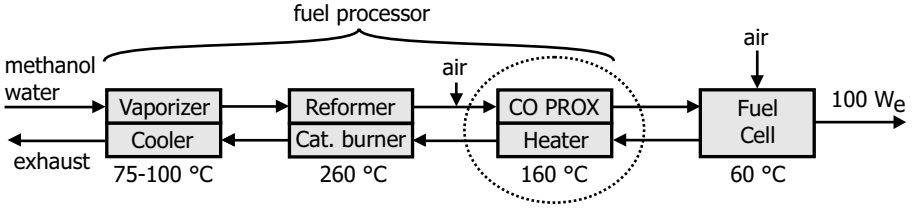

Figure 3.1: A fuel processor–fuel cell system, consisting of three integrated micro devices and a miniature fuel cell, all working at specific temperatures. The encircled unit is the integrated preferential oxidation–heat exchanger device studied in this paper.

ide present, and a catalytic burner to supply energy for the methanol–water vaporization and the endothermic methanol reforming. Based on an energy analysis of the system, the fuel processor is subdivided into three integrated microdevices operating at different temperatures, i.e. a vaporizer–cooler, a reformer–burner, and a preferential oxidation–heat exchanger unit, see Figure 3.1. The targeted volume for the portable fuel processor is 500 cm^3.

In this paper we describe the design, experimental and modelling work of the preferential oxidation–heat exchanger (ProxHeatex) microdevice, which is designed and manufactured in cooperation with the Institut für Mikrotechnik Mainz (IMM) and the Energy Research Center of the Netherlands (ECN). Main purpose of the device is to remove the carbon monoxide present in the reformate gas, since carbon monoxide is a severe poison for the fuel cell catalyst. To decrease the concentration of carbon monoxide to below 10 ppm, it is oxidized using a small quantity of air added to the reformate gas. To promote the oxidation of carbon monoxide and suppress the oxidation of hydrogen, a selective catalyst has to be used, like Pt/Al_2O_3 [14–16] or Au/Fe_2O_3 [17]. In this study a Pt-Co/α-Al_2O_3 catalyst is used, developed at ECN. The addition of cobalt to the catalyst was found to increase both activity and selectivity of the Pt/α-Al_2O_3 preferential oxidation catalyst. Since most of the fuel processor volume will be needed by the reformer unit, the aspired volume of the ProxHeatex unit amounts to 100 cm^3 including insulation material.

The ProxHeatex device also needs to recover 80% of the available heat to increase the energy efficiency of the fuel processor. Heat is released both by the oxidation reaction (11 W) and by cooling down the hot reformate gas from 250 °C to 60 °C, the operating temperature of the fuel cell, (13 W). The Prox-

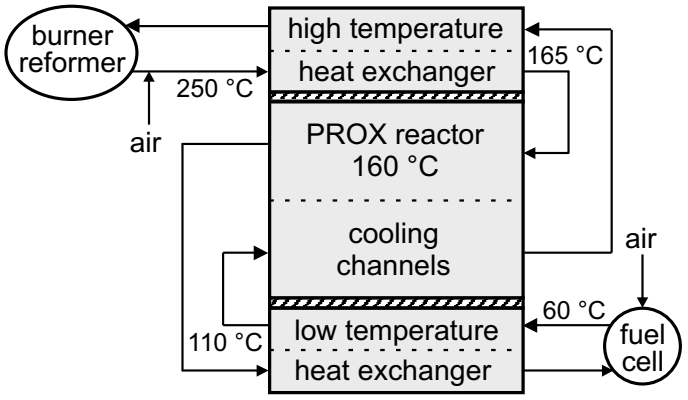

Figure 3.2: Schematic drawing of the integrated preferential oxidation–heat exchanger microdevice. The device consists of two heat exchangers and a cooled reactor. The temperatures of the reformate and coolant gas streams are also indicated.

Heatex device is designed to consist of three counter-current heat exchangers in series, see Figure 3.2, to provide an isothermal reaction zone and reach an efficient heat recovery. In the high temperature heat exchanger, the hot reformate gas is cooled down to the reaction temperature of 150 °C. The gas then enters the middle heat exchanger, which contains the preferential oxidation catalyst and serves as a cooled reactor. In the low temperature heat exchanger, the CO-free reformate gas is cooled down further to 60 °C. The recovered heat is used to preheat the combined fuel cell anode and cathode exhaust gas, which still contains about 5% of hydrogen, to about 200 °C, before it is sent to the catalytic burner.

The purpose of this work is also to study the heat transfer behavior of micro heat exchangers and the effect of integrating several heat exchangers in a single device. Micro heat exchangers differ from larger-scale heat exchangers, as axial conduction of heat through the solid material becomes more important in a microdevice [18, 19], while gas-solid heat transfer becomes less important. Therefore, in this paper we do not solely address practical issues like reactor performance, startup time, and heat recovery efficiency, but we also present a modelling study of the heat transfer in the micro heat exchangers. In the first part of the paper, we provide a detailed description of the construction of the ProxHeatex microdevice as well as the experimental setup that is used to study the performance of the device. Two heat transfer models are

developed to describe heat transfer in a microdevice, which are described in the second part of this paper. The experiments show that the one-dimensional heat exchange model is not able to predict the measured temperature gradients. The poor performance of the one-dimensional model is explained using a two-dimensional model, which also provides a clear insight into the heat transfer characteristics of the micro heat exchangers and may serve as a tool for further microreactor development.

3.2 ProxHeatex Design

The heat exchangers of the ProxHeatex device are constructed from 500 µm thick microstructured plates, as shown in Figure 3.3. The microstructured plates contain an outer groove that serves as a packing chamber, inlet and outlet flow distribution chambers, and a central part containing the actual channels. These microstructures were made in the stainless steel sheets by means of wet etching. Holes were drilled in the plates to provide inflow and outflow conduits for the two gas streams, to facilitate positioning of the plates on top of each other, and to provide a reactor bypass conduit. The bypass conduit is, however, not used in this study. The heat exchangers are formed by alternate stacking of mirror images of the plates. The exchangers are covered with an unstructured steel sheet to close the channels of the top plate. To be able to integrate the individual parts in a single stack, the plate geometry of all heat exchangers is identical, differing only in the channel cross-section and the number of channels. Graphite is used as sealing material for the reactor part and Klingersil®, a compressed fiber jointing material with a low thermal conductivity, is used in the low and high temperature heat exchangers.

The assembled device, schematically shown in Figure 3.4, contains 41 microstructured plates. The low and high temperature heat exchangers both contain six plates: two reformate side plates and four coolant plates. The reactor part consists of nineteen catalyst coated reaction plates and ten coolant plates. Three of the four walls of the reaction channels were coated at the Energy Research Center of the Netherlands with a 15 µm thick layer of a Pt-Co/α-Al_2O_3 catalyst. The total amount of catalyst in the reactor is 0.98 g. The two flanges are fixed with eight screws to compress the gaskets and make the device leaktight. Specifications of the individual units are listed in Table 3.1. The complete device measures $66 \times 53 \times 50\,mm^3$ and weights 980 g. To reduce external

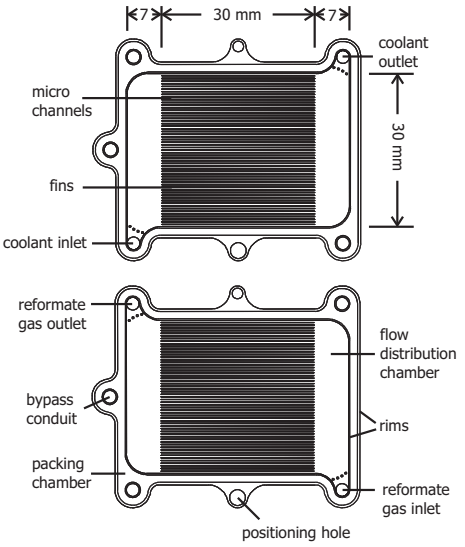

Figure 3.3: Microstructured heat exchanger plates; stacking of the two plate types creates a heat exchanger; plate dimensions (w×l) are 35 × 48 mm^2, with 58 microchannels of (w×h×l) 0.4 × 0.3 × 30 mm^3; the diameter of the inlets and outlets is 2 mm and the width of the packing chambers is also 2 mm.

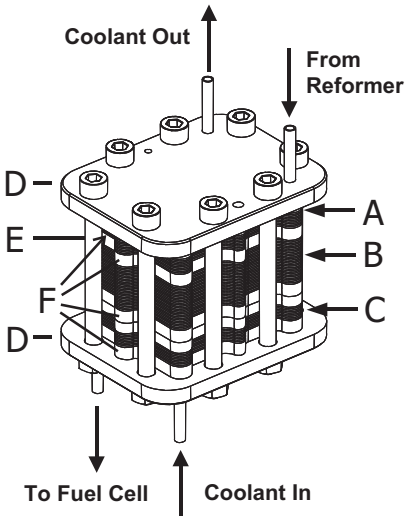

Figure 3.4: Assembled microreactor, developed in cooperation with the Institut für Mikrotechnik Mainz and the Energy research Center of the Netherlands. It consists of a high temperature heat exchanger (A), a cooled reactor (B), and a low temperature heat exchanger (C); outer dimensions are 66 × 53 × 50 mm^3; D: flanges, E: fixing screw, F: position of the four insulation plates.

heat losses from the device, the complete device is insulated by a 3 cm thick layer of HT/Armaflex® insulating material.

Insulating plates are inserted between the heat exchangers and the reactor, and between the heat exchangers and the flanges, to thermally separate the various device parts. Three different sets of insulation plates were manufactured to provide insulation between the various device parts. The first insulation plate type is a 4 mm thick stainless steel plate. A 2 mm deep air chamber was milled from the top of the plate over 90% of the plate's surface area, to increase its thermal resistance. The second insulation plate is a 2 mm thick plate cut from the same Klingersil® material as used for the seals in the

Table 3.1: Specifications of the integrated prox device.

parameter	HT exchanger[a]		prox reactor		LT exchanger	
	ref	cool	ref	cool	ref	cool
number of plates	2	4	19	10	2	4
number of channels	58	58	83	75	58	58
channel width [µm]	400	400	250	250	400	400
channel height [µm]	300	300	187	125	300	300

[a]HT = high temperature, LT = low temperature, ref = reformate side, cool = coolant side

heat exchangers. The third type of insulation plate consists of a stack of three 2 mm thick Klingersil® plates, of which two plates have a hole cut out over 90% of the plate's surface area. Two holes were drilled in each of the insulating plates to connect the inlets and outlets of the reactor and the heat exchangers. The thermal resistance (layer thickness divided by material conductivity and transfer surface area) of the three insulation layers is 0.87, 3.0, and 63 K/W, respectively.

The flow path of the reformate and coolant gas through the device is shown in Figure 3.5. In this figure also the locations of the thermocouples are indicated, which measure the inlet and outlet temperatures of the device at a position just outside the flanges, four internal temperatures at the outlets of the reactor and heat exchangers, and the temperatures of the top and bottom flanges. The four internal thermocouples measure the metal temperature instead of the gas temperature, as it was not possible to avoid contact of the thermocouples with the walls of the conduit in which they were inserted. However, at the outlet side of the reactor and heat exchangers, the difference between gas and metal temperature is expected to be small.

The reformate gas consisted of 0.5% CO, 1.6% O_2, 56% H_2, 18% CO_2, and balance helium. The reformate gas was analyzed for oxygen and CO at the inlet and outlet of the ProxHeatex device to determine conversion and selectivity. The analysis was done with a gas chromatograph equipped with a Poraplot U and a Molesieve 5A column and a micro-TCD detector using helium as carrier gas. As the reformate gas was projected to enter the ProxHeatex device at a temperature of 250 °C, the gas was first preheated to 300 °C just before entering the prox device. A cable heater was used to reduce heat losses in the tube between the preheater and the ProxHeatex device. In the exper-

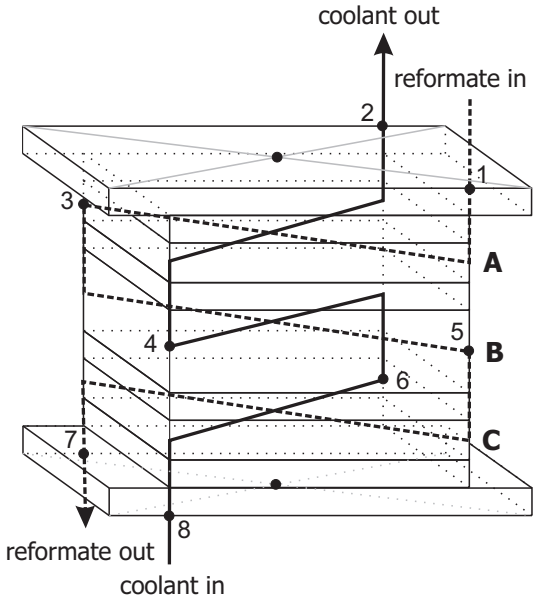

Figure 3.5: Schematic representation of the flow paths of the reformate and coolant gas through the microdevice. Temperature measurement points are indicated by black dots and are numbered for further reference. A, B, and C designate the high temperature exchanger, the reactor, and the low temperature exchanger, respectively.

iments pure nitrogen was used as coolant gas. To preheat the coolant gas to 60 °C, the coolant feed tube was heated over a distance of 1.5 m with a cable heater. No CO was fed when the temperature profile in the device was studied, since the presence of CO causes deactivation of the catalyst and the preferential oxidation reaction itself was of minor importance in this case. CO oxidation was replaced by hydrogen oxidation to mimic the heat production in the prox reactor. Although hydrogen reacts faster than CO, the total amount of heat production was considered more important than the heat production rate.

3.3 Heat Transfer Modelling

A one-dimensional heat transfer model was developed to describe the temperature profile in the microdevice. The model calculates the temperature profiles of the reformate gas (r), the coolant gas (c), and the metal of the heat exchanger

plates (m). For conventional heat exchangers the walls are usually not modelled separately, as axial conduction through the walls of the tubes can usually be neglected. However, for micro heat exchangers axial conduction is an important factor determining the heat exchanger efficiency [18, 19]. As the distance between the reformate and coolant channels is very small and the conductivity of stainless steel is two orders of magnitude larger than that of the gases, the radial temperature profile in the material between the channels was neglected. By also assuming an even flow distribution over the microchannels, heat exchange in the channel region was described by a one-dimensional model.

Plug flow was assumed for both gases and axial dispersion was neglected. Due to the fast radial heat transport, axial dispersion introduced by the laminar flow profile could also be neglected. The temperature profile of the gases is then determined by convective heat transport and heat exchange with the metal walls. When the length coordinate is made dimensionless with the length of the heat exchanger, the equations for the reformate and coolant gas become

$$\left(\dot{m}c_p\right)_{\mathrm{r}} \frac{\mathrm{d}T_{\mathrm{r}}}{\mathrm{d}\hat{x}} = -\alpha_{\mathrm{r}} A_{\mathrm{r}} (T_{\mathrm{r}} - T_{\mathrm{m}}) \tag{3.1}$$

$$\left(\dot{m}c_p\right)_{\mathrm{c}} \frac{\mathrm{d}T_{\mathrm{c}}}{\mathrm{d}\hat{x}} = -\alpha_{\mathrm{c}} A_{\mathrm{c}} (T_{\mathrm{m}} - T_{\mathrm{c}}) \tag{3.2}$$

with $(\dot{m}c_p)_i$ the heat transport capacity (mass flow rate $\times$ heat capacity) of fluid i (W K^{-1}), α_i the gas–solid heat transfer coefficients (W m^{-2} K^{-1}), and A_i the respective heat exchange surface areas (m^2). To calculate the heat transfer coefficients, entrance effects were neglected and a constant Nusselt number of 3.1 was assumed for the rectangular microchannels [20].

The model for the metal plates takes into account axial heat conduction through the plates, heat exchange with the two gases, with adjacent device parts and with the environment, and, for the reactor part, heat production due to reaction, to give

$$\begin{aligned} -\frac{\lambda_{\mathrm{m}} A_{\mathrm{m}}}{L} \frac{\mathrm{d}^2 T_{\mathrm{m}}}{\mathrm{d}\hat{x}^2} = {} & \alpha_{\mathrm{r}} A_{\mathrm{r}} (T_{\mathrm{r}} - T_{\mathrm{m}}) - \alpha_{\mathrm{c}} A_{\mathrm{c}} (T_{\mathrm{m}} - T_{\mathrm{c}}) \\ & - \alpha_{\mathrm{ex}} A_{\mathrm{ex}} (T_{\mathrm{m}} - T_{\mathrm{ex}}) - \alpha_{\mathrm{in}} A_{\mathrm{in}} (T_{\mathrm{m}} - T_{\mathrm{in}}) + \dot{Q}_{\mathrm{p}} \end{aligned} \tag{3.3}$$

with λ_{m} the conductivity of the reactor material (W m^{-1} K^{-1}), A_{m} the cross-sectional area of the reactor material perpendicular to the x-axis (m^2), and L

the heat exchanger length (m). The heat transfer coefficient for heat exchange between adjacent device parts (α_{in}) is calculated from the conductivity, thickness and cross-sectional area of the insulating layer and of the device parts themselves. The external losses are calculated with a heat transfer coefficient (α_{ex}) of 3.5 W m^{-2} K^{-1}, based on the external surface of the device without insulation, which is derived from the experimentally determined cooling curve of the device, recorded after closing the gas feeds. Heat production due to reaction ($\dot{Q}_p$) is modelled as

$$\dot{Q}_r(\hat{x}) = \dot{Q}_{tot} \cdot k e^{-k\hat{x}}. \tag{3.4}$$

with the decay factor k arbitrarily set at 10 to simulate a fast reaction.

The top and bottom flanges were also included in the model. Due to their thickness, they were modelled as being isothermal. For the flanges heat exchange with the adjacent heat exchanger and with the environment is included in the model as well as heat exchange between the two flanges through the tightening screws. Furthermore, an additional heat input from the heater cables to the flanges is included. The additional heat input was calculated, based on the steady state temperature of the flanges without flow to the device, to be 4 W at the reformate inlet, and 0.5 W at the coolant inlet. Since all parts of the device exchange heat with each other, the temperatures in the heat exchangers, the reactor, and the two flanges were calculated simultaneously in three linked one-dimensional models, using the Femlab® finite element solver [21].

Next to the one-dimensional model of the complete device also a two-dimensional model has been developed describing a single micro heat exchanger. The two-dimensional model describes the temperature fields in a plane, parallel to the microstructured plates. In the direction perpendicular to the plates, the temperatures are assumed to be constant. The model geometry consists of the channel area and the two flow distribution areas, as shown in Figure 3.6. Like in the 1D model, the 2D model takes into account convective heat transport by the flowing gases, heat transfer between gases and reactor material, heat conduction through the reactor material, and heat transfer to adjacent device parts and to the environment. The velocity field in the flow distribution areas is not calculated, but is approximated by a linearly decreasing y-velocity from the inlet to the opposite wall, and a linearly

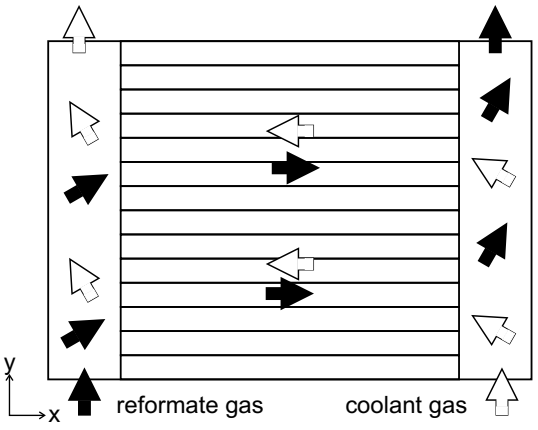

Figure 3.6: Model geometry of the two-dimensional micro heat exchanger model with the flow distribution regions and the central channel region. The flow paths of the reformate and coolant gas are indicated by the full and open arrows, respectively.

increasing x-velocity from the side wall to the channel region. In the channel region the reformate gas flows straight from left to right and the coolant gas straight from right to left. In this way the continuity equation is satisfied in the complete domain. Gas–solid heat transport is modelled with a constant Nusselt number of 3.1 for the channel region and 7.5 [20] for the flow distribution regions. For the heat conductivity of the solid material volume averaged values are used, which are different for flow distribution and channel region and, within the channel region, are different for the x- and y-direction due to the presence of the fins. Here only the equations for the left flow distribution region are presented:

$$(\dot{m}c_p)_\mathrm{r} \cdot \hat{x} \cdot \frac{\partial T_\mathrm{r}}{\partial \hat{x}} + (\dot{m}c_p)_\mathrm{r} \cdot (1-\hat{y}) \cdot \frac{\partial T_\mathrm{r}}{\partial \hat{y}} = -\alpha_\mathrm{r} A_\mathrm{r} (T_\mathrm{r} - T_\mathrm{m}), \tag{3.5}$$

$$-(\dot{m}c_p)_\mathrm{c} \cdot \hat{x} \cdot \frac{\partial T_\mathrm{c}}{\partial \hat{x}} + (\dot{m}c_p)_\mathrm{c} \cdot \hat{y} \cdot \frac{\partial T_\mathrm{c}}{\partial \hat{y}} = \alpha_\mathrm{c} A_\mathrm{c} (T_\mathrm{m} - T_\mathrm{c}), \text{ and} \tag{3.6}$$

$$\begin{aligned} -\frac{\lambda_\mathrm{m} A_{\mathrm{m}x}}{L_x} \frac{\partial^2 T_\mathrm{m}}{\partial \hat{x}^2} - \frac{\lambda_\mathrm{m} A_{\mathrm{m}y}}{L_y} \frac{\partial^2 T_\mathrm{m}}{\partial \hat{y}^2} &= \alpha_\mathrm{r} A_\mathrm{r} (T_\mathrm{r} - T_\mathrm{m}) - \alpha_\mathrm{c} A_\mathrm{c} (T_\mathrm{m} - T_\mathrm{c}) \\ &\quad - \alpha_\mathrm{ex} A_\mathrm{ex} (T_\mathrm{m} - T_\mathrm{ex}) - \alpha_\mathrm{in} A_\mathrm{in} (T_\mathrm{m} - T_\mathrm{in}), \end{aligned} \tag{3.7}$$

with $\hat{x}$ and $\hat{y}$ the dimensionless coordinates, and the other terms similar as for the one-dimensional model. The equations for the right flow distribution

region are similar, except that the factors $\hat{x}$, $(1-\hat{y})$, and $\hat{y}$ in equations (3.5) and (3.6) are replaced by $(1-\hat{x})$, $\hat{y}$, and $(1-\hat{y})$, respectively. In the channel region the gases flow straight from right to left and vice versa, which means that equations (3.5) and (3.6) simplify to equations (3.1) and (3.2). Equation (3.7) is similar in all regions, except that the constants change to reflect the differences is gas–solid heat transfer and metal cross-section.

3.4 Results and Discussion

3.4.1 Preferential oxidation activity

The performance of the ProxHeatex device is evaluated in terms of preferential oxidation activity and selectivity. The reformate gas flow rate is reduced from 2.9 to 0.8 SLM (standard liter per minute), as the amount of catalyst present in the reactor is less than is needed for full conversion of the projected amount of carbon monoxide. This also reduces the amount of heat produced in the reactor. Since the device does not contain an external heater to control its temperature, this would lead to a decreased reactor temperature. The oxygen inlet concentration is increased to 1.6% to increase the heat production in the reactor via additional hydrogen burning and increase the reactor temperature to 160 °C. Figure 3.7 shows the conversion and selectivity of the preferential oxidation reaction as a function of time. The figure shows that the initial carbon monoxide conversion is high and the CO outlet concentration is reduced to 7 ppm. However, the catalyst deactivates rapidly and the CO outlet concentration rises to 300 ppm over a period of 4 hours. While the catalyst deactivates, the selectivity remains constant at the initial value of 17%. Although catalyst deactivation is a problem for large scale operations, it is even more so for the portable ProxHeatex device, since in-situ regeneration of the catalyst or frequent replacement of the complete reactor are both unattractive options to be used for a portable fuel processor device. Therefore, it is important to improve the stability of the preferential oxidation catalyst, as well as to achieve a higher catalyst loading in the reactor.

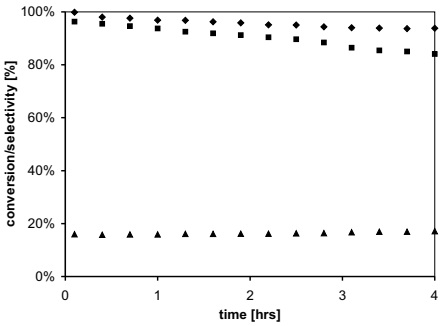

Figure 3.7: Carbon monoxide (♦) and oxygen (■) conversion, and the selectivity of oxygen towards carbon dioxide (▲), as function of time. Reformate flow rate was 800 sccm and reactor temperature was 160 °C.

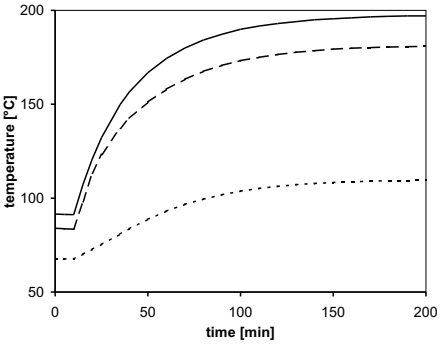

Figure 3.8: Temperature of the coolant outlet (full line), the reactor (dashed line), and the reformate outlet (dotted line) during startup of the device. Reformate and coolant flow rates were 2.9 and 6.3 SLM, respectively. Heat production was 11 W.

3.4.2 Start-up behavior

Another important factor for application of the ProxHeatex device in a portable fuel processor is its startup behavior. Figure 3.8 shows the reactor and flange temperatures as a function of time during startup of the device. The figure shows that the startup time of the device is large and that it takes over one hour to reach a reactor temperature of 160 °C. In the experiment the projected operating conditions are used, which are a reformate flow rate of 2.9 SLM, translating to a heat transport capacity (mass flow $\times$ heat capacity) of 0.07 W K^{-1}, and a coolant flow rate of 6.3 SLM (0.14 W K^{-1}). In the reactor 11 W of heat is generated by hydrogen burning. However, these numbers are small compared to the heat capacity of the device itself, which is about 460 J K^{-1}, resulting in the long startup time. The relatively large heat capacity of the device is partially a result of the large mass of the flanges and screws that were used for this first prototype, which makes up about 70% of the total mass of the device. The transient behavior can still be improved greatly by optimization of the design, for example by using welding to connect the plates instead of using a construction with gaskets and flanges.

However, start-up time can be a serious issue for gas-phase microsystems that do not operate at room temperature, especially if little reactive heat is

generated. Although fluids can be heated or cooled very rapidly in microreactors, the transient behavior of the device itself depends on the ratio of the heat capacity of all solid material (the microstructured plates, packings, flanges, screws, and insulation) and the heat transport capacity of the fluid flows. This ratio is not favorable for a gas-phase microreactor, due to the high solid fraction of a microreactor and the low heat capacity of gases. For application of microdevices in fuel processors or other dynamic processes, care has to be taken to minimize the solid fraction of a microdevice and to use light-weight materials with low heat capacity for the construction of the device. Hardt et al. [22] demonstrate ways to intensify the gas-solid heat transfer in a microstructured reactor using meandering channels or an arrangement of 100 µm long microfins, which allows for a smaller reactor volume and, consequently, a reduction in the amount of solid material. Other options to improve the transient behavior of a microsystem include using high flow rates or elevated pressures to increase the gas-phase heat transport capacity, the use of increased reactant concentrations during start-up to increase reactive heat generation, and the use of additional (electric) heating.

3.4.3 Heat transfer efficiency

Also the heat transfer efficiency of the micro heat exchangers is studied. In three experiments the influence of the type of insulation plates between the device parts is studied on the temperature profile in the heat exchanger and reactor parts and thus on the heat transfer performance of the device. In the experiments the device is re-assembled three times, each time using a different type of insulation plates. In each case the steady state temperature profile was measured at the same operating conditions as described for the startup experiment. Figure 3.9 shows the temperature profile in the ProxHeatex device with the three different types of insulation plates. The figure shows that the heat exchange performance of the device increases when the thermal resistance between the units is increased, as both the temperature difference between the device parts and the axial temperature gradient within the device parts increase. The fraction of heat, of the total amount of heat available in the reformate gas and released by the oxidation reaction, that is recovered in the device by heating-up the coolant gas, increased from 68% with the steel insulation plates to 78% with the multiple Klingersil® sheets. It is difficult

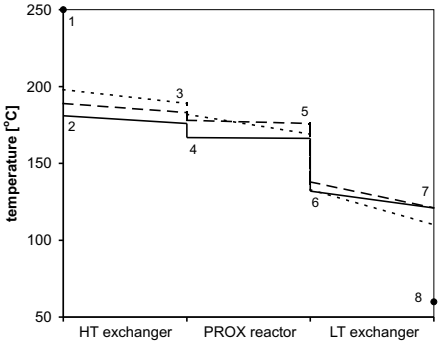

Figure 3.9: Measured temperature profiles in the ProxHeatex microdevice assembled with three different insulation layers: steel plates with air chambers (solid line), single Klingersil® sheets (dashed line), and multiple Klingersil® sheets with air chambers (dotted line). The inlet temperature of the reformate gas was 250 °C and of the coolant gas 60 °C. The numbers indicate the temperature measurement points specified in Figure 3.5.

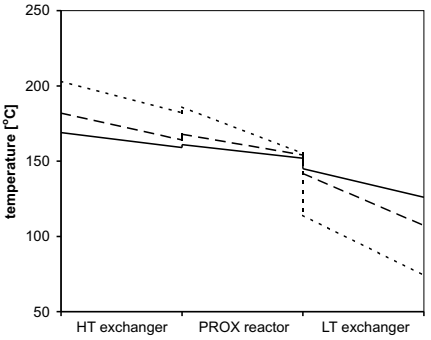

Figure 3.10: Calculated temperature profiles in the ProxHeatex microdevice assembled with three different insulation layers: steel plates with air chambers (solid line), single Klingersil® sheets (dashed line), and multiple Klingersil® sheets with air chambers (dotted line). The inlet temperatures are 250 and 60 °C for reformate and coolant gas, respectively.

to assess the performance of the individual heat exchangers, since conductive heat transfer between adjacent units, which we cannot measure, plays an important role in the integrated microdevice.

We also predicted the temperature profiles found in the experiment with the one-dimensional heat transfer model described in the section on heat transfer modelling. In Figure 3.10 the calculated temperature profiles are presented for the three cases with different insulation plates. The predicted average temperatures of the individual device parts are within 15 °C of the experimental values, except for the multiple Klingersil® sheets insulation case, where the deviation is 30 °C for the low temperature heat exchanger temperature. This is a good result taken into account that the model does not contain any fit parameters. However, the temperature gradients in the device parts are not well predicted. The predicted temperature gradients are about twice as large as is found in the experiments, which makes the model unsuited to predict the heat exchanger efficiencies. The model also predicts a clear influence of

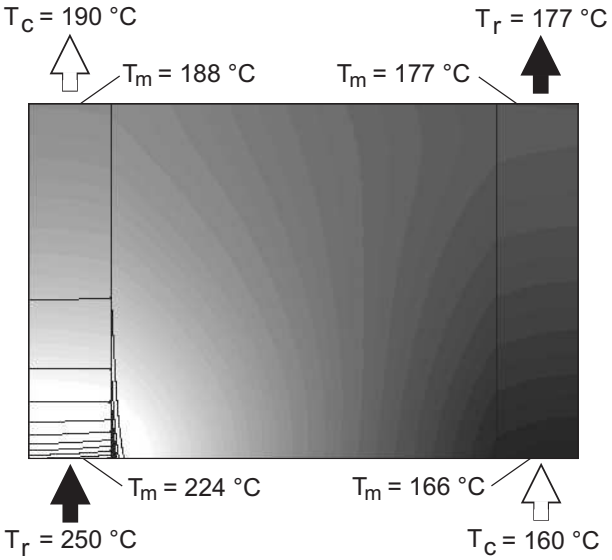

Figure 3.11: Results of the 2D calculations of the high temperature heat exchanger. The grays show the temperature distribution in the metal plates. The metal (m), reformate gas (r), and coolant gas (c) temperatures at the inlets and outlets are also indicated. The contour lines show the temperature difference between the hot reformate gas and the metal plates. The reformate gas–metal temperature difference is 26 °C at the reformate gas inlet (bottom-left) with each contour line representing approximately 2.5 °C decrease in the gas–metal temperature difference.

the type of insulation plates used, on the temperature difference between the device parts, while the experiments show almost no influence.

3.4.4 Two-dimensional model results

A two-dimensional heat transfer model was made to explain the deviations between the one-dimensional model and the experiments. The simulation results for the high temperature heat exchanger are depicted in Figure 3.11. In this figure the contour lines show the temperature difference between the hot reformate gas and the metal of the heat exchanger and the grays indicate the metal temperature. Furthermore, at the inlets and outlets the temperature of the gases and the metal is indicated. The contour lines show that the temperature equilibration between gas and metal is very fast and takes place almost completely within the first part of the flow distribution region. Although the

flow distribution chambers do not contain microchannels, the height of the distribution chambers is very small, in this case 300 µm, which means that heat transfer is already very effective in these regions of the plate. The effective heat exchange in the flow distribution chambers leads to considerable differences in temperature between the first and the last channels, which is the reason for the over-prediction of the temperature gradients by the one-dimensional channel model. It is interesting to note that the temperature of the coolant gas at the outlet is 2 °C higher than the metal temperature, due to the part of the coolant gas that flows over the hotter bottom part of the plate.

The grays in Figure 3.11 show the metal temperature of the exchanger. As the gas temperature equilibrates very fast with the metal temperature, the gas temperature is close to the metal temperature except for a small region near the inlets. The figure shows that the temperature difference between left and right side of the plate, or hot and cold side of the exchanger, is about 58 °C at the bottom side of the plate, but decreases towards the exits at the top side of the figure to 11 °C. Since the plates are almost square and a significant part of the heat transfer takes place in the flow distribution chambers, the behavior of the heat exchanger more closely resembles that of a mixed co-current and cross-flow behavior than a true counter-current behavior, leading to a low heat exchange efficiency. For the design of a micro plate heat exchanger, it is thus important to take the complete plate geometry into consideration. To increase the counter-current character of the heat exchangers and to improve the heat exchange efficiency of the ProxHeatex microdevice, the length of the exchanger plates should be increased and the width of the plates, or the distance between inlet and outlet, should be decreased.

3.5 Conclusions

A microdevice was designed and manufactured for the preferential oxidation of carbon monoxide in a hydrogen-rich reformate gas, consisting of two heat exchangers and a cooled reactor, all integrated in a single stack of microstructured plates. The device was able to reduce the carbon monoxide concentration from 0.5% to 7 ppm, but only during the first half hour of operation, after which the conversion dropped due to catalyst deactivation. Due to the large mass of the device, the startup time of the device was about one hour, which is too long for application in a portable fuel processor. The temperature profiles

in the heat exchangers were measured and a one-dimensional heat exchange model was developed to predict these profiles. A considerable deviation exists between experiments and the one-dimensional model. A two-dimensional simulation of one of the heat exchangers showed that large differences exist between channels close to the inlet and channels further from the inlet, causing the one-dimensional model to fail. This example shows that it is important to consider the complete plate geometry when designing a micro plate heat exchanger.

Based on the outcome of this study, the design of the ProxHeatex device was improved and a second prototype will be built. The new device will contain longer channels and a reduced plate width to improve the heat exchanger efficiency. To reduce the mass of the unit, the microstructured plates will be welded together instead of using gaskets to provide leak-tightness. Furthermore, a better catalyst will be applied in the reactor and also a higher catalyst loading will be used.

Acknowledgement

The authors gratefully acknowledge funding from the European Commission for the Micro Reactor Technology for Hydrogen and Electricity (MiRTH-e) project within the Fifth Framework Programme under contract number ENK6-2000-00110.

Bibliography

[1] W. Ehrfeld, V. Hessel, and H. Löwe. *Microreactors: new technology for modern chemistry*. Wiley-VCH, Weinheim, Germany, 2000.

[2] K. F. Jensen. Microreaction engineering — is small better? *Chem. Eng. Sci.*, 56:293–303, 2001.

[3] A. Kursawe, E. Dietzsch, S. Kah, D. Hönicke, M. Fichtner, K. Schubert, and G. Wießmeier. Selective reactions in microchannel reactors. In W. Ehrfeld, editor, *Proceedings of the Third International Conference on Microreaction Technology*, pages 213–223. Springer, Berlin, Germany, 2000.

[4] H. Kestenbaum, A. Lange de Oliveira, W. Schmidt, F. Schüth, W. Ehrfeld, K. Gebauer, H. Löwe, T. Richter, D. Lebiedz, I. Untiedt, and H. Züchner. Silver-catalyzed oxidation of ethylene to ethylene oxide in a microreaction system. *Ind. Eng. Chem. Res.*, 41:710–719, 2002.

[5] E. V. Rebrov, S. A. Duinkerke, M. H. J. M. de Croon, and J. C. Schouten. Optimization of heat transfer characteristics, flow distribution, and reaction processing for a microstructured reactor/heat-exchanger for optimal performance in platinum catalyzed ammonia oxidation. *Chem. Eng. J.*, 93: 201–216, 2003.

[6] M. Janicke, A. Holzwarth, M. Fichtner, K. Schubert, and F. Schüth. A microstructured catalytic reactor/heat exchanger for the controlled catalytic reaction between H_2 and O_2. *Stud. Surf. Sci. Catal.*, 130:437–442, 2000.

[7] G. Veser. Experimental and theoretical investigation of H_2 oxidation in a high-temperature catalytic microreactor. *Chem. Eng. Sci.*, 56:1265–1273, 2001.

[8] A. Lohf, W. Ehrfeld, V. Hessel, and H. Löwe. A standardized modular microreactor system. In J. Baselt, W. Ehrfeld, K.-P. Jaeckel, I. Rinard, and R. Wegeng, editors, *Proceedings of the Fourth International Conference on Microreaction Technology*, pages 441–451. AIChE, New York, 2000.

[9] A. Y. Tonkovich, J. L. Zilka, M. R. Powell, and C. J. Call. The catalytic partial oxidation of methanol in a microchannel chemical reactor. In W. Ehrfeld, I. H. Rinard, and R. S. Wegeng, editors, *Proceedings of the Second International Conference on Microreaction Technology*, pages 45–53. AIChE, New York, 1998.

[10] J. W. Ashmead, J. K. Nyquist, J. A. Perrotto, C. T. Blaisdell, M. H. Johnson, and J. F. Ryley, Jr. *Integrated chemical processing apparatus and processes for the preparation thereof*, 1997. US Patent 5,690,763.

[11] R. S. Wegeng, L. R. Pederson, W. E. TeGrotenhuis, and G. A. Whyatt. Compact fuel processors for fuel cell powered automobiles based on microchannel technology. *Fuel Cells Bulletin*, 3:8–13, 2001.

[12] J. D. Holladay, E. O. Jones, M. Phelps, and J. Hu. Micro fuel processor for use in a miniature power supply. *J. Power Sources*, 108:21–27, 2002.

[13] E. R. Delsman, E. V. Rebrov, M. H. J. M. de Croon, J. C. Schouten, G. J. Kramer, V. Cominos, T. Richter, T. T. Veenstra, A. van den Berg, P. D. Cobden, F. A. de Bruijn, C. Ferret, U. d'Ortona, and L. Falk. MiRTH-e: Micro Reactor Technology for Hydrogen and Electricity. In M. Matlosz, W. Ehrfeld, and J. P. Baselt, editors, *Proceedings of the Fifth International Conference on Microreaction Technology*, pages 268–274. Springer Verlag, Berlin, Germany, 2001.

[14] S. H. Oh and R. M. Sinkevitch. Carbon monoxide removal from hydrogen-rich fuel cell feed streams by selective catalytic oxidation. *J. Catal.*, 142:254–262, 1993.

[15] M. J. Kahlich, H. A. Gasteiger, and R. J. Behm. Kinetics of the selective CO oxidation in H_2-rich gas on Pt/Al_2O_3. *J. Catal.*, 171:93–105, 1997.

[16] C. D. Dudfield, R. Chen, and P. L. Adcock. A carbon monoxide PROX reactor for PEM fuel cell automotive application. *Int. J. Hydrogen Energy*, 26:763–775, 2001.

[17] M. J. Kahlich, H. A. Gasteiger, and R. J. Behm. Kinetics of the selective low-temperature oxidation of CO in H_2-rich gas over Au/α-Fe_2O_3. *J.*

Catal., 182:430–440, 1999.

[18] W. Bier, W. Keller, G. Linder, D. Seidel, K. Schubert, and H. Martin. Gas to gas heat transfer in micro heat exchangers. *Chem. Eng. Proc.*, 32:33–43, 1993.

[19] T. Stief, O.-U. Langer, and K. Schubert. Numerical studies on optimal thermal conductivity in microscale heat transfer structures. *Chem. Ing. Tech.*, 70:1539–1544, 1998.

[20] R. K. Shah and A. L. London. Laminar flow forced convection in ducts. In T. F. Irvine and J. P. Hartnett, editors, *Advances in Heat Transfer, Supplement 1*. Academic Press, New York, 1978.

[21] Comsol AB. *Femlab®, version 2.3b*. Stockholm, Sweden, 2003.

[22] S. Hardt, W. Ehrfeld, and V. Hessel. Strategies for size reduction of microreactors by heat transfer enhancement effects. *Chem. Eng. Comm.*, 190: 540–559, 2003.

Design and Operation of a Preferential Oxidation Microdevice for a Portable Fuel Processor

4

This chapter has been published as:

E.R. Delsman, M.H.J.M. de Croon, A. Pierik, G.J. Kramer, P.D. Cobden, Ch. Hofmann, V. Cominos, and J.C. Schouten. Design and Operation of a Preferential Oxidation Microdevice for a Portable Fuel Processor. *Chem. Eng. Sci.*, 56:4795–4802, 2004.

Abstract

Microreactor technology creates opportunities for the development of miniature chemical devices, in which several unit operations are integrated. In this paper we describe the design, model simulation, and experimental validation and operation of a microdevice for the preferential oxidation of carbon monoxide in hydrogen-rich reformate gas. The microdevice integrates two heat exchangers and one reactor, all consisting of welded stacks of microstructured plates. We show that the device is able to reduce the carbon monoxide concentration to 10 ppm in combination with a high heat recovery efficiency of 90%. The design of the microstructured plates was based on a combination of three-dimensional computational fluid dynamics simulations of the flow pattern and a two-dimensional heat transfer model, in which the flow pattern was approximated. An integral one-dimensional micro heat exchange model was then used to design the integrated device. This approach may be well suited for designing microstructured reaction systems.

4.1 Introduction

In recent years microfabrication technologies have been introduced in the field of chemical process engineering to realize microchannel devices, with channel diameters of the order of 100–500 µm [1, 2]. These devices have an inherently large surface area-to-volume ratio, offering high heat and mass transfer rates, which is beneficial for attaining high selectivities and conversions and enables optimum control of temperature and residence time [3, 4]. Microreactors also show large promise in the development of miniature chemical devices, where several unit operations are integrated with microstructured sensors and actuators to form a micro chemical plant [5].

These miniaturized chemical devices also offer opportunities for small scale fuel processing and portable power generation, for example to replace battery packs in laptops or mobile phones [6]. Within the European Union funded project MiRTH-e [7], a miniaturized fuel-processing system is developed to generate hydrogen in-situ from a methanol–water mixture, to fuel a 100 W_e fuel cell. The fuel processing system consists of a steam reformer, which converts methanol and water to a hydrogen-rich gas, a preferential CO oxidation unit to remove the 0.5% of carbon monoxide present, and a catalytic burner to supply energy for the methanol–water vaporization and the endothermic methanol reforming. Based on an energy analysis of the system, the fuel processor is subdivided into three integrated microdevices: a vaporizer–cooler, a reformer–burner, and a preferential oxidation–heat exchanger unit, see Figure 4.1. The targeted volume of the portable fuel processor is 500 cm^3.

In this paper we show the experimental and modelling results of a pref-

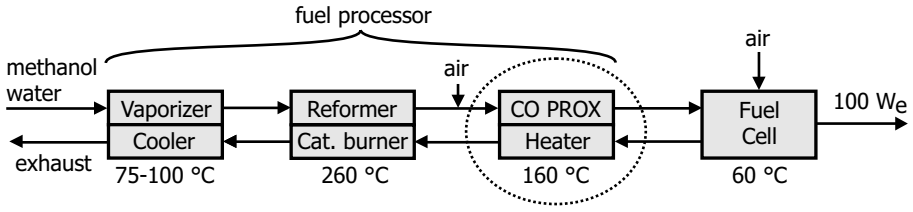

Figure 4.1: A fuel processor–fuel cell system, consisting of three integrated microdevices and a miniature fuel cell, all working at specific temperatures. The encircled unit is the integrated preferential CO oxidation–heat exchanger device studied in this paper.

erential CO oxidation–heat exchanger (ProxHeatex) microdevice. The device is an improved version of an earlier prototype [8]. The ProxHeatex device demonstrates the potential of microreactor technology to realize a compact chemical device, consisting of one reactor and two heat exchangers. The design is based on accurate fast-calculating models describing the temperature profile in the complete device. The success of the models stems from the well-defined laminar flow conditions on the microstructured plates and the high degree of repetition presented by the large number of parallel microchannels. In this paper, we first provide a detailed description of the design and construction of the ProxHeatex microdevice and of the heat transfer models used in the design process. Subsequently, the performance of the device is shown in terms of carbon monoxide conversion and heat recovery, as well as the ability of the heat transfer models to accurately describe the temperature profile in the device.

4.2 The ProxHeatex Device

4.2.1 Design and Construction

The main purpose of the preferential oxidation–heat exchanger (ProxHeatex) device is to remove the carbon monoxide present in the hydrogen-rich reformate gas by oxidation with a small quantity of air. Since carbon monoxide is a severe poison for the fuel cell catalyst, the carbon monoxide concentration must be reduced to below 10 ppm. A selective Pt-Ru/α-Al_2O_3 catalyst is used, developed at ECN [9], to promote the oxidation of carbon monoxide over the oxidation of hydrogen. Secondly, the ProxHeatex device needs to recover at least 80% of the available heat to ensure a high fuel processor efficiency. The available heat consists of 11 W generated by the preferential oxidation reaction and 13 W released by cooling down the hot reformate gas from 250 °C to 60 °C, the operating temperature of the fuel cell. The recovered heat is used to preheat the combined fuel cell anode and cathode exhaust gas, which still contains 5% of hydrogen, before it is sent to the catalytic burner.

The ProxHeatex device is designed to consist of three counter-current heat exchangers in series, see Figure 4.2. In the first (high-temperature) heat exchanger, the hot reformate gas is cooled down to the reactor temperature. The second heat exchanger is the actual preferential oxidation reactor. It contains

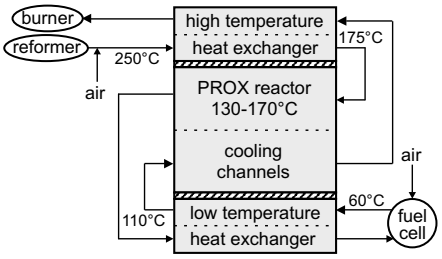

Figure 4.2: Schematic drawing of the integrated preferential oxidation–heat exchanger microdevice. The temperatures of the reformate and coolant gas streams are indicated.

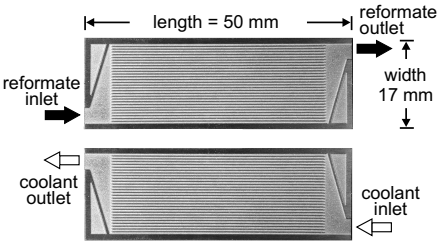

Figure 4.3: Reformate side (black arrows) and coolant side (white arrows) microstructured heat exchanger plates, each with 29 microchannels of (w×h×l) 0.4 × 0.3 × 40 mm^3.

1.5 g of catalyst applied on the walls of the reaction channels using a wash coating technique. The thickness of the coating is 50 µm. The reactor is designed to establish a decreasing temperature profile in the reaction zone from about 170 to 130 °C. In this way a high activity at the beginning of the reaction zone is combined with a high selectivity at the end of the reaction zone. In the third (low temperature) heat exchanger, the CO-free reformate gas is cooled down further to a temperature of 60 °C to extract its remaining thermal energy.

The heat exchangers and the reactor were constructed from 500 µm thick stainless steel plates, in which from both sides microchannels and flow distribution chambers were etched [10], see Figure 4.3. The microstructured plates were stacked alternatingly and were laser welded around the perimeter to form counter-current micro heat exchangers. Tubes with an inner diameter of 3 mm were welded to the stack of plates to provide gas inlets and outlets. The size and number of plates are listed in Table 4.1. Compared to the first prototype device [8], the length/width ratio of the plates was increased to improve the heat exchanger efficiency and the distribution of fluid flow over the microchannels. Stainless steel was chosen as construction material for the heat exchangers, since its low thermal conductivity enables a large temperature gradient over the length of the plate. As material for the reactor also aluminium was considered, which use would result in a smaller, more optimal temperature gradient over the reactor of 20 °C instead of 40 °C for stainless steel. However, aluminium was discarded as an option, due to practical problems concerning its welding.

Table 4.1: Specifications of the low and high temperature heat exchangers and the preferential CO oxidation reactor.

parameter	heat exchangers		PrOx reactor	
	ref[a]	cool	ref	cool
plate dimensions (w×l) [mm]	17 × 50		17 × 40	
number of plates	2	4	22	11
channels per plate	29	29	13	10
channel width [µm]	400	400	1000	500
channel height [µm]	300	300	200	250
channel length [mm]	40	40	30	30

[a] ref = reformate side, cool = coolant side

The ProxHeatex device was assembled by connecting the tubes of the heat exchangers and the reactor using short pieces of a silicon rubber hose, see Figure 4.4. Between the reactor and the heat exchangers, a 1 cm thick layer of Klingersil® insulating material was fitted. The temperatures of the reformate and coolant gases flowing into and out of the heat exchangers and reactor were measured. Also the metal temperature was measured at various locations inside the heat exchangers and the reactor using the thermocouple channels into the sides of the device. The external dimensions of the assembled ProxHeatex device are (w×l×h) 17 × 64 × 55 mm^3. Its volume without external insulation is 60 cm^3 and its weight is 150 g. The complete device was insulated by a 5 cm thick layer of glass wool material, leading to a total volume of 3 liter.

For the design of the microstructured plates and the integrated device, three separate mathematical models were used, which all focus on separate parts of the design problem. First, a three-dimensional (3D) computational fluid dynamics model of the gas flow on a single microstructured plate was used to optimize the geometry of the flow distribution chambers to ensure equal flow rates in the microchannels [11]. Second, a two-dimensional (2D) heat-transfer model was used to optimize the plate design to establish equal temperatures in the microchannels. In this model the gas flow pattern was approximated using results from the 3D model. Finally, a one-dimensional (1D) heat transfer model was used to design the complete ProxHeatex device. This 1D model was used specifically to study the interactions between the

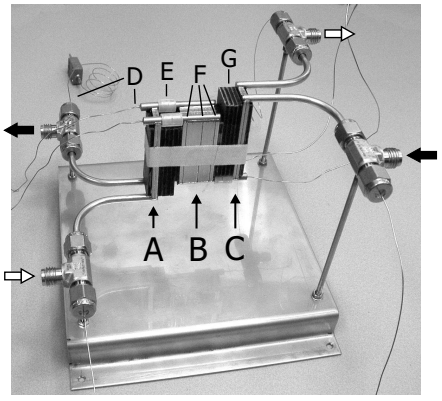

Figure 4.4: Assembled ProxHeatex microdevice consisting of a low temperature heat exchanger (A), a preferential oxidation reactor (B), and a high temperature heat exchanger (C); D: thermocouples, E: tube connection, F: thermocouple channels; G: insulating material.

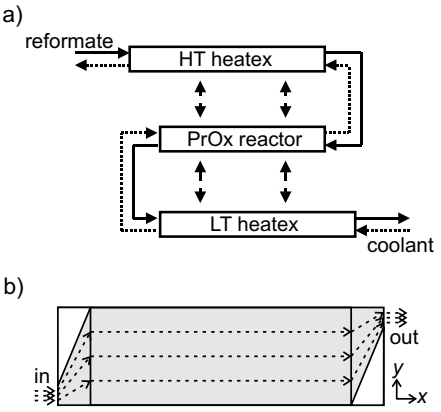

Figure 4.5: a) Schematic representation of the three linked 1D heat transfer models describing the temperature profiles in the ProxHeatex device. b) Representation of the reformate gas flow pattern in the 2D model (cf. top picture in Figure 4.3).

three parts of the device, caused by the interconnected fluid flows and by direct heat transfer through the insulation between the device parts. The heat transfer models are described in more detail in the subsequent section.

4.2.2 Experimental

The ProxHeatex device was tested in a set-up capable of feeding a reformate gas with a variable flow rate and composition and a separate flow of nitrogen to serve as the coolant gas. The reformate gas stream was first preheated to 350 °C. Due to external heat losses, it entered the ProxHeatex device at a temperature between 180 and 260 °C, depending on the gas flow rate. The temperature at the reformate gas outlet of the reactor part was controlled by varying the coolant flow. Pure nitrogen was used as coolant gas, which was preheated to 60 °C before entering the device. The standard reformate gas consisted of 0.5% CO, 0.88% O_2, 56% H_2, 18% CO_2, 10% H_2O, 0.75% N_2, and balance helium. The standard flow rate was 3 SLM (standard liter per minute), corresponding to the amount of hydrogen needed for a 100 W_e fuel cell. Experiments were performed at varying oxygen excess (expressed as a λ-value

equal to $2F(O_2)_{in}/F(CO)_{in}$), and varying reactor outlet temperature. The reformate gas was analyzed for oxygen and CO at the inlet and outlet of the ProxHeatex device to determine conversion and selectivity. The analysis was done with a gas chromatograph equipped with a Poraplot U and a Molesieve 5A column and a micro-TCD detector using helium as carrier gas.

4.3 Heat Transfer Modelling

The final design of the ProxHeatex device was made using an integral mathematical model consisting of three one-dimensional (1D) sub-models describing the temperature profiles in the reactor and the two heat exchangers. Each sub-model consists of three differential equations, which describe the temperatures of the metal plates and of the reformate and coolant gases as a function of the dimensionless coordinate $\hat{x}$:

Reformate gas:
$$\left(\dot{m}c_p\right)_{\mathrm{r}} \frac{\mathrm{d}T_{\mathrm{r}}}{\mathrm{d}\hat{x}} = -\alpha_{\mathrm{r}} A_{\mathrm{r}} (T_{\mathrm{r}} - T_{\mathrm{m}}) \tag{4.1}$$

Metal plates:
$$-\frac{\kappa_{\mathrm{m}} A_{\mathrm{m}}}{L} \frac{\mathrm{d}^2 T_{\mathrm{m}}}{\mathrm{d}\hat{x}^2} = \alpha_{\mathrm{r}} A_{\mathrm{r}} (T_{\mathrm{r}} - T_{\mathrm{m}}) - \alpha_{\mathrm{c}} A_{\mathrm{c}} (T_{\mathrm{m}} - T_{\mathrm{c}}) - \alpha_{\mathrm{in}} A_{\mathrm{in}} (T_{\mathrm{m}} - T_{\mathrm{in}}) - \alpha_{\mathrm{ex}} A_{\mathrm{ex}} (T_{\mathrm{m}} - T_{\mathrm{ex}}) + \dot{Q}_{\mathrm{p}} \tag{4.2}$$

Coolant gas:
$$\left(\dot{m}c_p\right)_{\mathrm{c}} \frac{\mathrm{d}T_{\mathrm{c}}}{\mathrm{d}\hat{x}} = -\alpha_{\mathrm{c}} A_{\mathrm{c}} (T_{\mathrm{m}} - T_{\mathrm{c}}) \tag{4.3}$$

The equations describe a counter-current heat exchanger and include terms for convection by the two gases, gas-metal heat transfer, and axial heat conductivity in the metal plates. Although the flow on the plates is laminar, the large length/diameter ratio of the microchannels results in fluid Péclet numbers well above 100, indicating that gas phase axial heat conduction can be neglected. Furthermore, internal heat transfer between the heat exchangers and the reactor, external heat transfer to the environment, and heat production due to the exothermal reaction are included in the model. The three heat exchanger sub-models had to be solved simultaneously, since the inlets and outlets of the reactor and heat exchangers are connected, as is shown in Figure 4.5a, and since the heat exchange between the units is considerable. The equations were solved using the Femlab® finite element solver [12]. The 1D model assumes equal conditions in all channels as well as true counter-current flow in the flow distribution areas. The latter is not strictly true [8], but the dis-

crepancy between a one-dimensional and two-dimensional model decreases as the length/width ratio of the heat exchanger plates is increased.

The temperature distributions in the separate heat exchangers of the device were also studied using a two-dimensional (2D) heat transfer model to verify the applicability of the 1D model. The 2D model describes the temperature fields in a plane, parallel to the microstructured plates. In the direction perpendicular to the plates, the temperature is assumed to be constant. The model geometry consists of the channel area and the two flow distribution areas, as shown in Figure 4.5b. Like in the 1D model, the 2D model takes into account convective heat transport by the flowing gases, heat transfer between gases and metal plates, heat conduction through the metal plates, and heat transfer to the environment. The flow pattern of the gases was approximated by flow lines running straight between the channel region and the inlets and outlets, as shown in Figure 4.5b. In this way the costly fluid dynamics computations, which were done separately [11], were avoided during calculation of the temperature distribution. As an illustration of the numerical representation of the flow pattern in the flow distribution chambers, the x and y-components of the mass flow in the reformate inlet chamber are presented here:

$$\dot{m}_x = \frac{w_\mathrm{p}\dot{m}_\mathrm{tot}}{w_\mathrm{i} + \frac{w_\mathrm{p}-w_\mathrm{i}}{L_\mathrm{fd}}x} \qquad \text{and} \qquad \dot{m}_y = \dot{m}_x \frac{y}{x + \frac{w_\mathrm{i}L_\mathrm{fd}}{w_\mathrm{p}-w_\mathrm{i}}}, \tag{4.4}$$

where $\dot{m}_\mathrm{tot}$ is the total mass flow of the reformate gas, and w_i, w_p, and L_fd, the widths of the inlet and the plate, and the length of the flow distribution chamber, respectively.

4.4 Results and Discussion

4.4.1 Reactor performance

During the test program the ProxHeatex device was operated continuously for five days. In this period several shorter experiments ($<$ 2 hours) were performed to scan a wide range of operating conditions as well as several longer experiments ($>$ 10 hours) to study the stability of the catalyst.

The results of the long-run experiments are shown in Figure 4.6. The figure shows the CO outlet concentration of the device and the reactor inlet and outlet temperatures. In the experiments, the reactor outlet temperature is kept

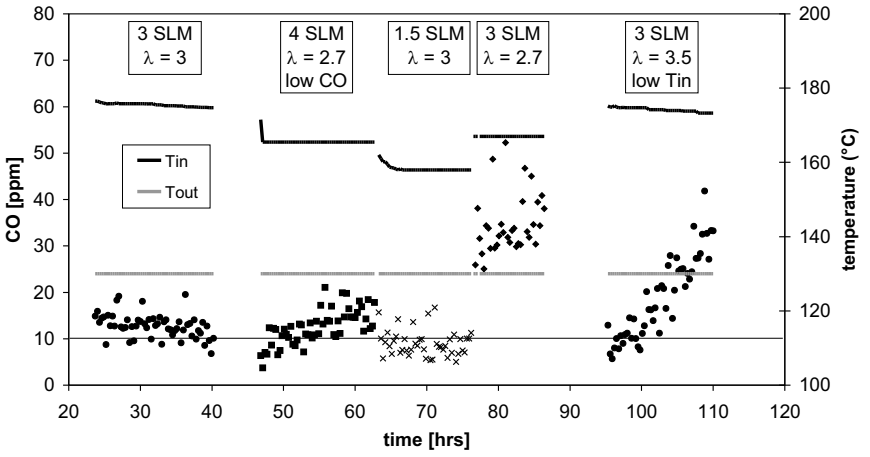

Figure 4.6: Reactor temperature and CO outlet concentration as a function of time for various flow rates and λ-values. The CO inlet concentration was 5000 ppm and in the 'low CO' experiment 3750 ppm. The 'low Tin' experiment was done at a lower inlet temperature of the reformate and coolant gas to the device (200 and 30 °C instead of 240 and 60 °C, respectively).

constant by regulating the coolant flow rate to the device. Consequently, the reactor inlet temperature changes depending on the operating conditions. The figure shows that, for several combinations of flow rate and oxygen excess, the microstructured device is capable of reducing the CO concentration in a realistic reformate gas from 5000 ppm to about 10 ppm at a flow rate of 7.4 $\mathrm{mmol_{CO}\ s^{-1}\ kg_{cat}^{-1}}$. However, the CO conversion is not always stable. Especially in the last experiment, catalyst deactivation becomes evident as the CO concentration remains close to 10 ppm in the first five hours, but then starts to rise to about 30 ppm during the next ten hours. The catalyst activity compares well with the results of Dudfield et al. [13], who reduced the CO concentration in a reformate stream from 7000 ppm to below 10 ppm in a dual-stage heat exchanger–reactor using a similar Pt-Ru/Al_2O_3 catalyst, up to a flow rate of 5.7 $\mathrm{mmol_{CO}\ s^{-1}\ kg_{cat}^{-1}}$.

Also a number of shorter experiments was done to characterize the influence of the operating conditions on the reactor behavior and to determine optimal process conditions. In Figure 4.7 the CO outlet concentration and the temperature gradient across the reactor are plotted for varying λ, flow rate,

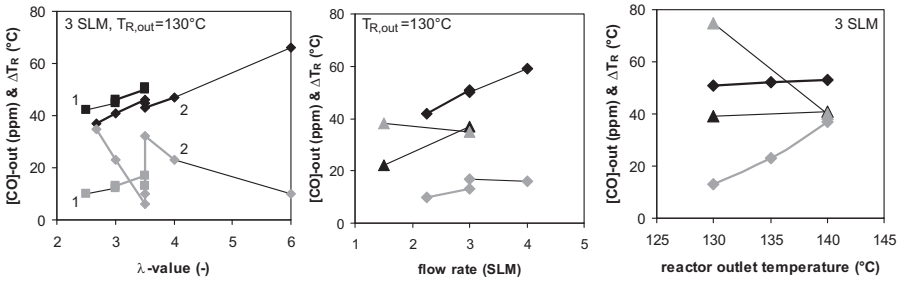

Figure 4.7: CO outlet concentration (gray line) and temperature gradient in the reactor (ΔT_R, black line) as a function of λ, flow rate, and reactor outlet temperature. The numbers in the left graph indicate two measurement series with fresh (1) and aged (2) catalyst. In the two graphs on the right, the diamonds indicate λ=3.5 and the triangles λ=2.7.

and reactor outlet temperature. Although the reactor temperature gradient shows a logical trend, it increases with increasing oxygen excess and flow rate and it is independent of the reactor outlet temperature, the relation between the operating conditions and the CO outlet concentration is less clear, as contradictory results are found depending on the time-on-stream and on the oxygen excess.

The data in the left diagram are measured during two periods: data series 1 between 15–35 hours after start-up, and data series 2 between 75–115 hours after start-up. In the first series, a lower λ-value is beneficial, due to a better selectivity resulting from the lower reactor inlet temperature. In the second series, catalyst deactivation becomes noticeable and then a higher λ is beneficial to increase the catalyst activity. The two diagrams on the right show that it depends on the oxygen excess whether the CO concentration rises or falls with increasing flow rate or reactor temperature. For a low oxygen excess, a higher reactor inlet temperature leads to an increased catalyst activity and CO conversion. For a high oxygen excess, the reactor inlet temperature is already high enough for full CO conversion and an increase in the reactor inlet temperature in this case results in a loss in selectivity and thus a lower CO conversion. It is apparent that, due to the high degree of heat integration in the microdevice, the reaction chemistry directly affects the reactor temperature and vise versa, which leads to complex reactor behavior and might complicate reactor control.

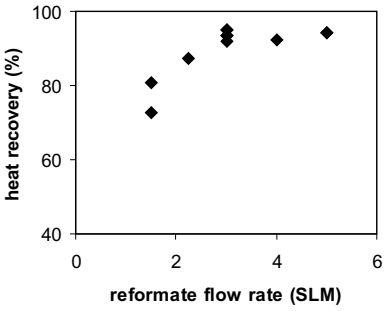

Figure 4.8: Heat recovery efficiency of the ProxHeatex device as a function of the reformate gas flow rate (λ varies between 2.5 and 6).

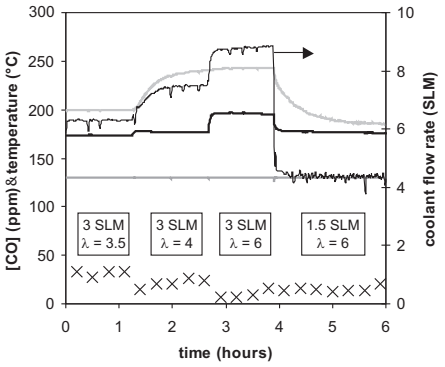

Figure 4.9: Transient respons to step changes in the operating conditions. Displayed are the reactor inlet (thick black line), reactor outlet (dark gray line), and reformate gas inlet (light gray line) temperatures, the coolant flow rate (thin black line), and the CO outlet concentration (markers).

Next to the CO conversion, also the heat recovery efficiency of the ProxHeatex device was determined from the outlet temperature of the coolant gas. The heat recovery efficiency is plotted in Figure 4.8 as a function of the reformate gas flow rate. The overall heat recovery of the device varies between 73 and 95%, with the higher numbers corresponding to higher flow rates and higher oxygen excess. The aspired heat recovery of 80% for the ProxHeatex unit is thus amply met for most operating conditions, which indicates that there is room to reduce the insulation thickness. The measured values of the heat recovery suggest that the insulation thickness can be decreased to 2 cm, which will decrease the total volume of the device including insulation to 0.6 liter, but this was not tested experimentally.

Finally, the ability of the device to respond to changes in the operating conditions was studied. The reactor temperature, coolant flow rate, and CO outlet concentration are plotted in Figure 4.9 as a function of time, to illustrate the transient behavior of the device. The figure shows that the temperature control by regulating the coolant flow rate functions well: despite drastic changes in λ and reformate gas flow rate, the reactor outlet temperature remains constant. The changes in operating conditions are reflected in the reactor inlet

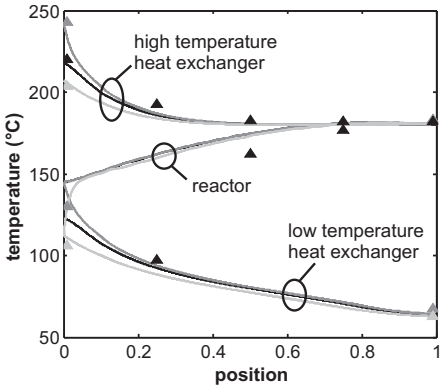

Figure 4.10: Comparison of the 1D heat transfer model (lines) with experimental data (triangles); black: metal temperature, dark gray: reformate gas (3 SLM, λ = 3.5), light gray: coolant gas (6.7 SLM).

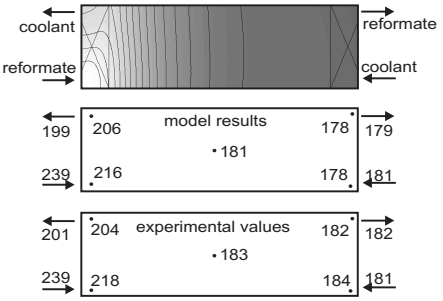

Figure 4.11: Calculated 2D profile of the metal temperature of the high-temperature heat exchanger (linear scale 178–216 °C). Model and experimental values of the metal temperature are given at five locations as well as the reformate and coolant gas inlet and outlet temperatures.

temperature and the coolant flow rate. The reactor inlet temperature reaches a new steady value within four minutes after the applied change. The reactor response is much faster than the response of the reformate gas inlet temperature of the device, which is determined by the larger time constants of the reformate gas pre-heater and the connective tubing. The effect on the CO outlet concentration cannot be seen, since the sampling frequency of the CO concentration is too low.

4.4.2 Model results

To validate the 1D model of the integrated microdevice, the calculated temperature profiles from the model are compared to the experimental values. The input parameters for the model are calculated using material properties and known engineering correlations. The external heat loss was calculated from the time required to cool down the device. Figure 4.10 shows the experimental and modelling results for standard operating conditions. In the figure, the reformate gas, coolant gas, and metal temperatures are plotted for both heat exchangers and the reactor. The temperature of the hot reformate gas enter-

ing the device is plotted in the upper-left corner and the inlet temperature of the coolant gas is plotted in the lower-right corner. The reactor temperature gradient is predicted 10 °C too low, due to the assumed uniform heat production in the reactor. However, on a whole the figure shows good agreement between model and experiments, also showing the potential of modelling for the accurate design of microstructured reactors more in general.

We also compared the 2D model of the high-temperature heat exchanger to experimental data. Figure 4.11 shows the calculated 2D temperature profile of the high-temperature heat exchanger, as well as calculated and experimental values of the metal temperature in the four corners and the center of the heat exchanger. The temperature profile shows that, except in the left inlet chamber, the temperature difference across the width of the plate is small, which justifies the use of the 1D model. Furthermore, the calculated and experimental values correspond well with each other, showing the applicability of the 2D model. In the heat exchangers, we expect no significant temperature profile perpendicular to the plates, since their height is relatively small. However, the temperature profile in the height of the reactor was measured experimentally and was found to be about 5 °C, which is within acceptable limits.

4.5 Conclusions

This study shows the design, modelling, and operation of a microstructured preferential CO oxidation–heat exchanger device for a 100 W_e portable fuel processor. The microstructured device consists of a cooled reactor, which contains 1.5 g of a Pt-Ru/α-Al_2O_3 catalyst coating, and two integrated heat exchangers. The device is able to reduce the carbon monoxide concentration of a realistic methanol reformate gas from 5000 to 10 ppm, for a period of 100 hours, in combination with a high heat recovery efficiency of 90%. Reaction experiments also reveal complex reactor behavior as a result of the high degree of heat integration in the microdevice, which might complicate reactor control.

Furthermore, a dedicated microreactor design procedure is outlined that consists of three steps. In the first step, 3D fluid dynamics simulations are used to optimize the geometry of the flow distribution chambers to ensure equal flow rates in the individual microchannels. In the second step, a 2D heat transfer model is used to verify that all microchannels also experience

equal temperature profiles. When several components operating at different temperatures are integrated into a small device, transfer of heat between the components is hard to avoid. Therefore it is not sufficient to design the individual components separately, and in the third step an integral model is developed, consisting of fast-calculating 1D sub-models of the separate units. This third model accurately described the temperature distribution in the device, as measured experimentally.

Acknowledgement

The authors gratefully acknowledge funding from the European Commission for the Micro Reactor Technology for Hydrogen and Electricity (MiRTH-e) project under the 'Energy, Environment and Sustainable Development' Programme, contract number ENK6-CT-2000-00110.

Nomenclature

A_i	surface area [m^2]
c_p	heat capacity [J kg^{-1} K^{-1}]
F	molar flow rate [mol s^{-1}]
L, w	length, width [m]
$\dot{m}$	mass flow [kg s^{-1}]
$\dot{Q}_\mathrm{p}$	heat production [W]
T_c	coolant gas temperature [K]
T_ex	temperature of external environment [K]
T_in	temperature of adjacent unit [K]
T_m	metal temperature [K]
T_r	reformate gas temperature [K]
$\hat{x}$	dimensionless heat exchanger length [-]
α_i	heat transfer coefficient [W m^{-2} K^{-1}]
κ	heat conductivity [W m^{-1} K^{-1}]
λ	oxygen excess [-]

Bibliography

[1] G. Kolb and V. Hessel. Micro-structured reactors for gas phase reactions. *Chem. Eng. J.*, 98:1–38, 2004.

[2] V. Hessel, S. Hardt, and H. Löwe. *Chemical Micro Process Engineering — Fundamentals, Modelling and Reactions*. Wiley-VCH, Weinheim, Germany, 2004.

[3] H. Kestenbaum, A. Lange de Oliveira, W. Schmidt, F. Schüth, W. Ehrfeld, K. Gebauer, H. Löwe, T. Richter, D. Lebiedz, I. Untiedt, and H. Züchner. Silver-catalyzed oxidation of ethylene to ethylene oxide in a microreaction system. *Ind. Eng. Chem. Res.*, 41:710–719, 2002.

[4] E. V. Rebrov, S. A. Duinkerke, M. H. J. M. de Croon, and J. C. Schouten. Optimization of heat transfer characteristics, flow distribution, and reaction processing for a microstructured reactor/heat-exchanger for optimal performance in platinum catalyzed ammonia oxidation. *Chem. Eng. J.*, 93: 201–216, 2003.

[5] A. Lohf, W. Ehrfeld, V. Hessel, and H. Löwe. A standardized modular microreactor system. In J. Baselt, W. Ehrfeld, K.-P. Jaeckel, I. Rinard, and R. Wegeng, editors, *Proceedings of the Fourth International Conference on Microreaction Technology*, pages 441–451. AIChE, New York, 2000.

[6] J. D. Holladay, E. O. Jones, M. Phelps, and J. Hu. Micro fuel processor for use in a miniature power supply. *J. Power Sources*, 108:21–27, 2002.

[7] E. R. Delsman, E. V. Rebrov, M. H. J. M. de Croon, J. C. Schouten, G. J. Kramer, V. Cominos, T. Richter, T. T. Veenstra, A. van den Berg, P. D. Cobden, F. A. de Bruijn, C. Ferret, U. d'Ortona, and L. Falk. MiRTH-e: Micro Reactor Technology for Hydrogen and Electricity. In M. Matlosz, W. Ehrfeld, and J. P. Baselt, editors, *Proceedings of the Fifth International Conference on Microreaction Technology*, pages 268–274. Springer Verlag, Berlin, Germany, 2001.

[8] E. R. Delsman, M. H. J. M. de Croon, G. J. Kramer, P. D. Cobden, C. Hofmann, V. Cominos, and J. C. Schouten. Experiments and modelling of an integrated preferential oxidation – heat exchanger microdevice. *Chem. Eng. J.*, 101:123–131, 2004.

[9] P. J. de Wild, M. J. F. M. Verhaak, and D. F. Bakker. *Catalysts for the selective oxidation of carbon monoxide in hydrogen-containing gases*, 2000. International Patent WO 00/17097.

[10] P. M. Martin, D. W. Matson, and W. B. Bennet. Microfabrication methods for microchannel reactors and separation systems. In W. Ehrfeld, I. H. Rinard, and R. S. Wegeng, editors, *Proceedings of the Second International Conference on Microreaction Technology*, pages 75–80. AIChE, New York, 1998.

[11] E. R. Delsman, A. Pierik, M. H. J. M. de Croon, G. J. Kramer, and J. C. Schouten. Microchannel plate geometry optimization for even flow distribution at high flow rates. *Chem. Eng. Res. Des.*, 82:267–273, 2004.

[12] Comsol AB. *Femlab®, version 2.3b*. Stockholm, Sweden, 2003.

[13] C. D. Dudfield, R. Chen, and P. L. Adcock. A carbon monoxide PROX reactor for PEM fuel cell automotive application. *Int. J. Hydrogen Energy*, 26:763–775, 2001.

Microchannel plate geometry optimization for even flow distribution at high flow rates

5

This chapter has been published as:

E.R. Delsman, A. Pierik, M.H.J.M. de Croon, G.J. Kramer, and J.C. Schouten. Microchannel plate geometry optimization for even flow distribution at high flow rates. *Chem. Eng. Res. Des.*, 82:267–273, 2004.

Abstract

Microreactors generally consist of microstructured plates containing a large number of equal channels. The small diameter of the channels enables high heat and mass transfer rates. To exploit this feature and realize a high throughput within a small volume, it is necessary to use high flow rates. However, at these high flow rates it is not straight-forward to obtain an even distribution of fluid flow over the individual microchannels. A three-dimensional computational fluid dynamics (CFD) model was used to calculate the flow distribution on a microstructured plate. Calculation time was reduced by introducing an artificial viscosity in the channel region. The calculations show that a transitional velocity exists, below which the flow distribution is independent of velocity and above which inertia effects start to influence the distribution. To optimize the flow distribution, nine different plate geometries were studied at flow rates between 0.1 and 100 m s^{-1}, or $4{\cdot}10^{-4}$ to 0.4 m^3 hr^{-1} per plate. By optimizing the plate geometry, the relative standard deviation of the flow distribution was reduced from 19 to 3%. Furthermore, it is shown that the optimal geometry depends on the flow rate, which thus needs to be taken into account in the design of microchannel plates.

5.1 Introduction

In the last years microfabrication technologies are being introduced in the fields of chemistry and chemical process engineering to realize microchannel devices, e.g. mixers, heat exchangers, and reactors, with capabilities considerably exceeding those of conventional macroscopic systems [1, 2]. Microreactors have reaction channels with diameters of the order of 10–500 μm and channel lengths of about 1 to 10 cm with an inherently large surface area-to-volume ratio. These properties offer clear advantages such as high mass and heat transfer rates, which are beneficial for high selectivities and conversions and optimum heat control [3, 4]. Furthermore, the low hold-up in a microreactor offers excellent controllability, low safety risks and low environmental impact [5, 6]. This makes these micro reaction devices specifically suitable for highly exothermic reactions, short contact time reactions, and for the on-demand and safe production of toxic and hazardous chemicals.

The high heat and mass transfer rates in microreactors offer the possibility to realize a high throughput within a small volume. To realize a high throughput in a microreactor a large number of identical microchannels is used. However, the combination of high throughput and a small volume will result in high flow velocities inside a microdevice. These high velocities result in a potentially high pressure drop over the plate and can lead to an uneven distribution of the flow between the individual microchannels [7]. As a measure of the quality of the distribution, i.e. the the evenness of the flow distribution, we use the relative standard deviation, which is defined as

$$\sigma_{\mathrm{r}} = \frac{1}{\bar{F}} \sqrt{\frac{\sum_i (F_i - \bar{F})^2}{n-1}} \tag{5.1}$$

with $\bar{F}$ the mean flow rate per channel, F_i the actual flow rate per channel, and n the number of channels. An increase in the relative standard deviation thus corresponds to a less evenly distributed flow over the channels. The uneven distribution of fluid flow over the channels introduces dispersion, leading to loss in conversion and selectivity. Moreover, an uneven flow distribution increases the pressure drop over a microstructured plate compared to an even distribution. In this case not the heat and mass transfer rates, but the quality of the flow distribution sets a limit to the throughput of the device. Therefore, it is important to design channels and flow distribution chambers in a way to

minimize pressure losses and facilitate an even flow distribution, even at high flow rates.

Distribution of fluid flow over a set of small diameter channels was studied for various applications. Bassiouny and Martin [8, 9] developed an analytical model to calculate the flow distribution over the channels in plate heat exchangers, based on velocity changes in the flow headers and wall friction in the channels, but neglecting wall friction in the flow headers. Choi et al. [10] presented a computational fluid dynamics study of the flow distribution in a cooling module for microelectronics. They found that the ratio of the flow distribution chamber cross-sectional area to the cross-sectional area of the channel region is an important parameter influencing the flow distribution.

Commenge at al. [11, 12] have developed an analytical model to predict the flow distribution on microreactor plates with inlets and outlets in the corners of the plate and flow distribution chambers with a reducing cross-section. By dividing the flow distribution chambers in a number of segments equal to the number of channels, they were able to calculate the pressure drop between inlet and outlet based on the wall friction of the fluid in the channels and in the flow distribution chambers. The flow distribution was then calculated by minimizing the total pressure drop. Since the influence of inertia forces is neglected, symmetric flow distributions are found, reflecting the symmetry of the microchannel plate geometry.

The model of Commenge is only valid for low flow rates, when inertia forces can be neglected, in their case at inlet velocities below 10 m s^{-1}. For higher flow rates, when inertia forces become important, an analytical description of the flow pattern is more difficult and full computational fluid dynamics (CFD) modelling is necessary. However, the large aspect ratio of microchannels, with a length-to-diameter ratio typically in the order of 100, causes computational grids to be excessively large. Therefore, we will incorporate a number of simplifications in the CFD modelling to reduce the calculation time.

The work presented here is part of the European Union funded project MiRTH-e [13], in which a miniaturized fuel-processing system is developed to generate hydrogen in-situ from a methanol-water mixture, to fuel a 100 W_e fuel cell. One of the fuel processing units that is developed in the project, is a preferential CO oxidation device. This device removes the CO present in the hydrogen-rich reformate gas, to avoid deactivation of the fuel cell anode cata-

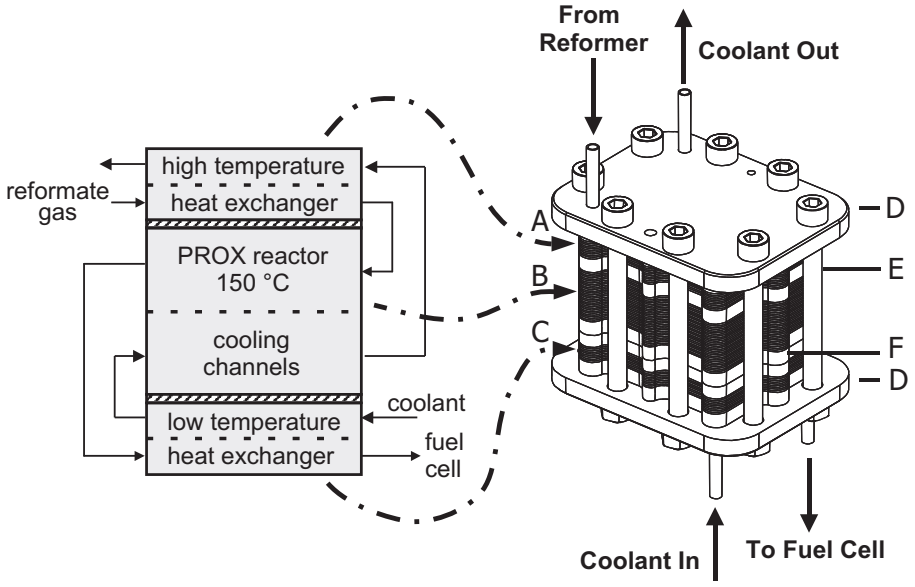

Figure 5.1: Design of the preferential CO oxidation device and the assembled microreactor, which was developed in cooperation with the Institut für Mikrotechnik Mainz GmbH (IMM, Germany) and the Energy research Center of the Netherlands (ECN). It consists of two heat exchangers (A and C), and a cooled reactor (B); outer dimensions 52 $\times$ 66 $\times$ 53 mm^3; D: flanges, E: fixing screw, F: insulation layer.

lyst, by oxidation with a small quantity of air. To realize a high fuel efficiency of the fuel processing system, the preferential oxidation device is equipped with a heat exchange system, which consists of three heat exchangers in series, Figure 5.1. The central one also serves as a cooled reactor and contains a coated Pt/Al_2O_3 preferential oxidation catalyst.

The heat exchangers consist of 500 µm thick, microstructured stainless-steel plates, Figure 5.2. The plates are fabricated by etching microchannels and flow distribution chambers in the plates with a height of 300 µm. The heat exchangers contain two types of plates, which are each others mirror image, to provide separate flow paths for the reformate and the coolant gas. The gases can be led to and from the exchangers through the four holes in the corners, which form conduits when the plates are stacked. From the inlets at the bottom side of the plates the gases are distributed over the plates and subsequently over all channels. At the other side the gases are collected and

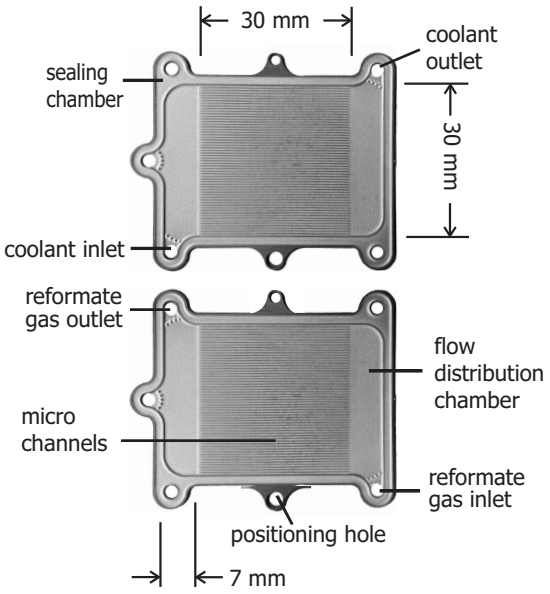

Figure 5.2: Microstructured heat exchanger plate geometry; stacking of the two plate types creates a heat exchanger; plate dimensions are (w×l) 35 × 48 mm^2, with 58 microchannels of (w×h×l) 0.4 × 0.3 × 30 mm^3; the width of the inlet and outlet is 2 mm and the width of the flow distribution chambers is 7 mm.

exit through the two outlets at the top side. Alternating stacking of the plates creates a counter-current heat exchanger. To ensure leak-tightness, graphite gaskets were inserted in-between the plates.

Each plate contains 58 microchannels with dimensions (w×h×l) of 0.4 × 0.3 × 30 mm^3. The geometry of the flow distribution chambers was based on the geometry used by Commenge et al. [12] with respect to the location of the inlets and outlets in the corners of the plate. However, the original triangular shape of the flow distribution chambers was changed to a rounded rectangular shape, which simplified manufacturing. The influence on the flow distribution was estimated to be limited, with a flow distribution relative standard deviation of 10%, which resembles the accuracy of the etching process, at a flow rate of 0.12 m^3 hr^{-1}.

In this paper we present a computational fluid dynamics (CFD) study of the flow distribution on the microstructured plates of the preferential oxidation device as well as an optimization study of the plate geometry to reach the design target regarding the quality of the flow distribution. However, although the study is based on a single case, we think that the results can be used to improve the design process of microreactors in general. In the first part of this paper, several different CFD-models are developed involving an increasing number of assumptions. These models are compared to show which

geometrical details are important to describe the flow pattern correctly and which assumptions can safely be made to reduce calculation time. From this study the best model was selected in terms of flow description and calculation time. In the second part, this model is used to study the flow distribution in more detail. In the final part the plate geometry is optimized to improve the quality of the flow distribution and to identify the geometrical factors that influence the flow distribution.

5.2 Choice of Simulation Method

In the first part of this study several flow calculation models are compared. Calculations were performed at inlet flow velocities between 0.1 and 100 m s^{-1}, resulting in volumetric flow rates between $4{\cdot}10^{-4}$ and 0.4 m^3 hr^{-1}. All calculations were performed with Fluent 6.0 CFD software on a 2.8 GHz Intel Xeon processor with 2 GB internal memory. The density and viscosity of the gas stream was set at 0.68 kg m^{-3} and $2.2{\cdot}10^{-5}$ Pa s, respectively. The no-slip boundary condition was set at all walls. It was not necessary to use slip-flow boundary conditions, as the Knudsen number calculated for the channels, $3 \cdot 10^{-4}$, is well below the critical value of 10^{-3} [14]. Furthermore, due to the small height (300 µm) of both the flow distribution chambers and the channels, the flow was laminar in all cases, with a maximum Reynolds number at the inlet of about 1600. The maximum Mach number was 0.25, based on an inlet velocity of 100 m s^{-1} and a temperature of 150 °C. Since the effect of compressibility on gaseous flows is small below a Mach number of 0.3 [15], the gas was assumed to be incompressible. However, since the maximum Reynolds and Mach numbers are close to their respective critical values, simulations at the highest flow rate were duplicated taking into account compressible flow and turbulence using the Spalart-Allmaras low-Reynolds number turbulence model. The influence of either effect on both pressure drop and flow distribution quality was below 8%.

The first model is a full three-dimensional model of the flow distribution chambers and of the 58 channels, left-hand side of Figure 5.3. The inlet and outlet tubes, which are actually perpendicular to the plate, are not included in the model. Instead, the inflow and outflow are modelled as straight surfaces in line with the plate. Without the inlet and outlet tubes, the geometry is symmetrical in a center plane between top and bottom wall, allowing simulation

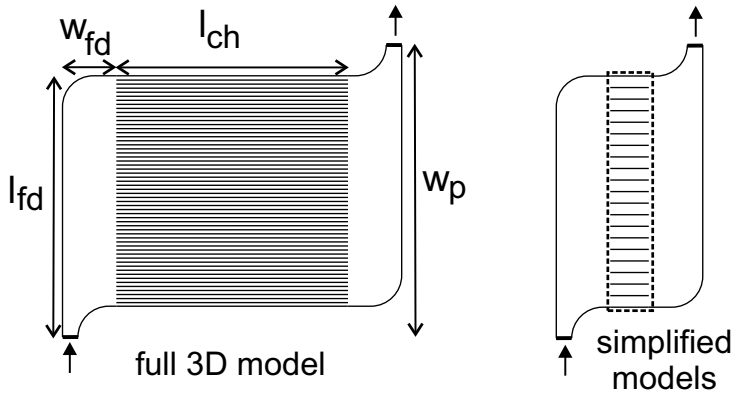

Figure 5.3: Outline geometry of the full three dimensional model (left) and the simplified 3D and 2D models (right); in the right figure the dashed box indicates the simplified channel region where the fluid viscosity is adjusted; inlets and outlets are indicated by arrows; w_{fd} and l_{fd} indicate the width and length of the flow distribution chambers, l_{ch} indicates the channel length, and w_p the plate width.

of only one half of the geometry. The model had about 500,000 computational nodes and it took about 150 minutes to reach convergence, which was reached when the scaled residuals had decreased to below 10^{-4}.

In the second model the channel region is simplified by reducing the number of channels from 58 to 20, by reducing the space between the channels to zero thereby increasing the total cross-sectional area of the channels, and by decreasing the channel length to 5 mm, right-hand side of Figure 5.3. To keep the pressure drop over the channels equal to that in the previous model, the viscosity of the gas in the channel region was increased to an artificial value. As the viscosity shows up as a constant in the momentum equations, this can be done without affecting continuity or the boundary conditions used. The simplification of the channel region resulted in a considerable reduction in the number of computational nodes. Additional advantages of this model are faster grid preparation and data analysis. Furthermore, cases with different channel geometries can be simulated without remeshing the model. The mesh was reduced to 250,000 nodes and the computation time was 20 minutes.

In the third model a 2D approximation was made to calculate the flow pattern. As the height of the channels and flow distribution regions is only 300 µm, it was assumed that the velocity profile in this direction was fully de-

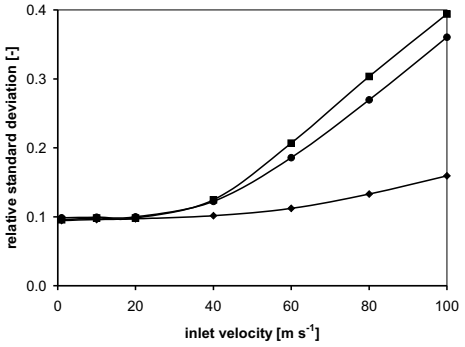

Figure 5.4: Relative standard deviation of the flow distribution as a function of the plate inlet velocity as calculated with the different CFD models: 3D model with 58 real channels (■), 3D model with 20 simplified channels (●), and the 2D model (⧫).

veloped in all locations on the plate. To calculate the pressure drop caused by friction with the top and bottom walls, the flow was approximated as flow between two infinite plates. This is allowed as the walls of the flow distribution area are far apart when compared to the distance between the top and bottom wall. The pressure drop is in this case given by

$$\nabla p = -\frac{12\mu}{{d_\mathrm{p}}^2} \cdot \mathbf{v} = -C_\mathrm{drag} \cdot \mathbf{v}, \tag{5.2}$$

where p is the pressure, μ the viscosity, d_p the distance between the plates, $\mathbf{v}$ the gas velocity, and C_drag a drag coefficient. The friction with top and bottom wall was included in the model as a drag force in a direction opposite to the flow direction. The channel region was described, as in the second model, by twenty channels with infinitely thin walls in between. The pressure drop in the channel regions was set by changing the drag force term. The mesh contained 35,000 nodes and calculation time was reduced to 55 seconds.

In Figure 5.4 the results of the three simulation models are compared. The figure shows a plot of the relative standard deviation, which is a measure of the flow distribution quality, against inlet flow velocity. In the figure two regimes can be distinguished. At low velocities, below 30 m s^{-1}, a constant relative standard deviation is found, which means that the flow distribution is independent of flow rate. In this regime all models give similar results. Also the transitional inlet velocity, above which the relative standard deviation starts to increase, is predicted equally well by all models. The two 3D models also produce comparable results at higher velocities, whereas the 2D model predicts a lower relative standard deviation. This is caused by the assumption of a developed velocity profile between top and bottom walls. This

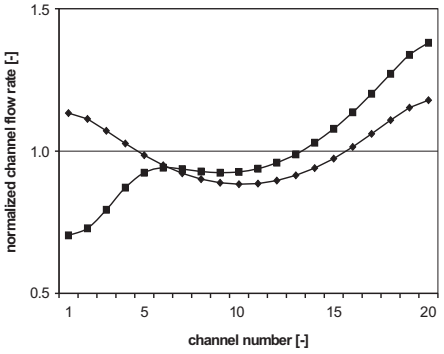

Figure 5.5: Flow distribution over the channels, calculated with the simplified 3D model, at an inlet velocity of 10 m s^{-1} (♦) and 60 m s^{-1} (■).

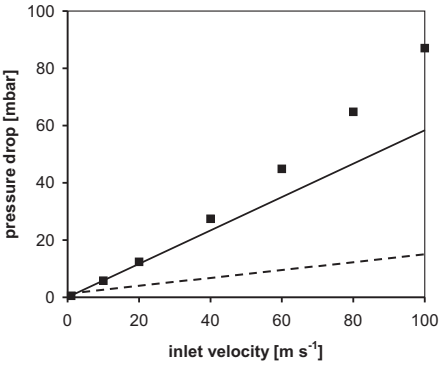

Figure 5.6: Total pressure drop over the microstructured plate as a function of the inlet velocity (■). At higher velocities the pressure drop increases more than linear with inlet velocity. The dashed line indicates the mean pressure drop over the channels alone.

assumption works well at lower velocities, but at an inlet velocity of 100 m s^{-1} the entrance length of the flow becomes considerable and can be calculated to extend more than 5 mm into the flow distribution chamber [16]. However, as it is not possible, due to the complex geometry, to predict the development of the flow profile beforehand, the 2D model could not be improved. As the differences between the two 3D models are small and the simplified 3D model is much easier to handle, this model was used for all further simulations.

5.3 Flow Distribution Results

As can be seen in Figure 5.4, two different flow regimes can be distinguished, depending on the inlet velocity, with a transition at a velocity of approximately 30 m s^{-1}. At lower velocities the flow distribution is independent of the inlet velocity, whereas at velocities above the transitional velocity the relative standard deviation of the flow distribution increases. Although flow velocities of up to 100 m s^{-1} may appear high, it is not uncommon for gas phase reactors. Indeed, using high flow rates is important for realizing a high throughput in a micro size unit. This can be done with only a moderate pres-

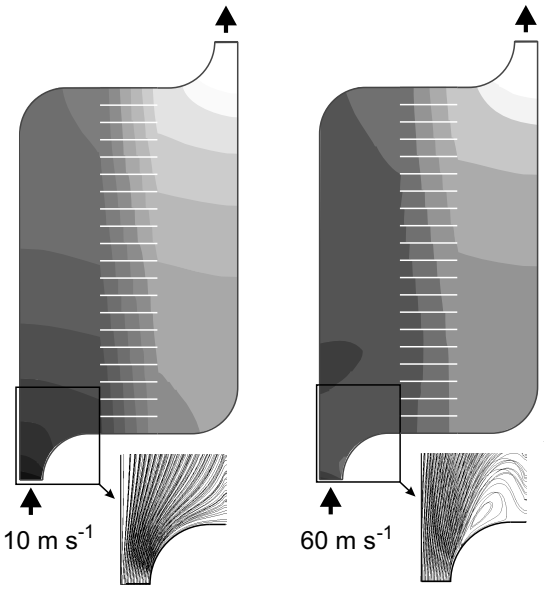

Figure 5.7: On the left-hand side the pressure profile of the complete plate (linear scale 0–6 mbar) and a particle track plot of a detail of the inlet, both at an inlet velocity of 10 m s^{-1}. At the right-hand side the pressure profile (linear scale 0–40 mbar) and particle track plot are presented at an inlet velocity of 60 m s^{-1}.

sure drop, about 90 mbar at a flow velocity of 100 m s^{-1}, as a result of the short length of the microchannels and the still laminar character of the flow.

Figure 5.5 presents the calculated flow distribution over the microchannels at velocities below (10 m s^{-1}) and above (60 m s^{-1}) the transition velocity. In the region where the flow distribution is independent of the flow rate, the flow field is completely determined by wall friction. Due to the symmetry of the plate geometry, the flow distribution profile is in this case symmetrical as well. At an inlet velocity of 60 m s^{-1}, inertia forces become important, distorting the symmetrical flow distribution profile leading to the observed increase in the relative standard deviation. The transition from a friction dominated case to a case where flow inertia becomes important is also visible in a plot of the pressure drop over the plate as function of inlet velocity, Figure 5.6. In the friction dominated regime the pressure drop increases linearly with velocity. At a velocity above 30 m s^{-1}, the inertia forces become increasingly important causing the pressure drop to increase more than linear with velocity. It can also been seen that the pressure drop over the flow distribution chambers is five times higher than the pressure drop over the channels.

The difference between the two flow regimes is also visible in the pressure profiles, Figure 5.7. At 10 m s^{-1}, left-hand side of the figure, the pressure profile is smooth and symmetrical. The inlay, showing an approximation of

the flow field, shows that no vortices are formed. At higher velocity, right-hand side of Figure 5.7, the pressure and velocity profiles are changed. The velocity profile shows that the gas flow detaches from the round wall just behind the inlet. Instead of making the bend towards the first channels, the gas flows straight into the inlet area, resulting in the formation of a vortex behind the bend. Consequently, the flow distribution becomes worse with less flow through the first channels and more through the last channels. At 60 m s^{-1} the pressure profile is not symmetrical anymore and an area of elevated pressure is formed in the inlet region just behind the bend of the inlet, caused by expansion of the gas flowing into the flow distribution chamber.

The pressure profiles of Figure 5.7 also present clues on how the flow distribution can be improved. As the flow distribution is determined by those sections of the geometry that result in the largest pressure drop, an even flow distribution can be established if the largest pressure drop is located over the channel region, assuming that all channels have equal flow resistance. However, the pressure profiles show that the largest pressure drop is located at the inlet and the outlet. Since the cross-sectional area of the inlet, 0.6 mm^2, is much smaller than of all channels together, 7 mm^2, the flow velocity is much higher at the inlet and outlet than in the channels. This results in a considerable pressure drop at the inlet and outlet, also because the difference in hydrodynamic diameter of the inlet, 0.52 mm, and of the channels, 0.34 mm, is small. To improve the quality of the flow distribution and to decrease the total pressure drop, the width of the flow distribution region and especially also the width of the inlet and outlet should be increased. Also a reduction in the length of the flow distribution area, by decreasing the width of the plate, would decrease the pressure drop over the flow distribution chambers and improve the flow distribution.

5.4 Geometry Optimization

To demonstrate the influence of the plate geometry on the quality of the flow distribution, three new cases were simulated, where the size of the flow distribution area, the length of the microchannels, and the plate height were varied. The results are presented in Figure 5.8, where the relative standard deviation of the flow distribution is plotted as a function of the volumetric flow rate. Volumetric flow rate is used instead of inlet velocity to be able to compare

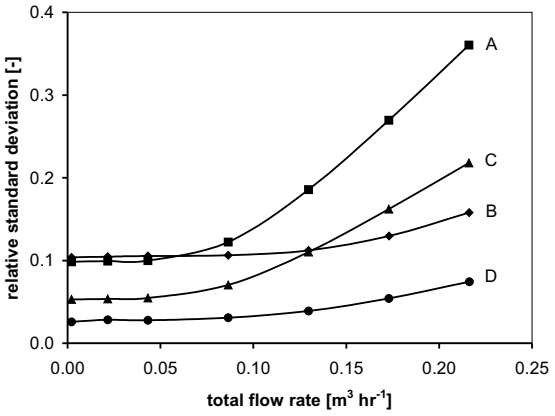

Figure 5.8: Relative standard deviation of the flow distribution as a function of the total gas flow rate for several modifications of the original plate geometry shown as case A (■): case B with a halved distance between top and bottom plate (♦), case C with doubled channel length (▲), and case D, in which the width of the flow distribution chambers, w_{fd} in Figure 5.3, is doubled (●).

cases with varying inlet cross-section. For reference the case studied in the previous section is given in the figure as case A. Decreasing the height of flow distribution chambers and channels, case B, does not improve the flow distribution quality in the shear dominated regime, but it does shift the transition velocity, where the flow distribution quality starts to decrease, to higher flow rates. However, the pressure drop is in this case six times higher than in case A. Case C shows the effect of doubling the length of the channels. At the expense of a 20% higher pressure drop, the flow distribution is improved by a factor of 1.7. The best results, however, are obtained by doubling the width of the flow distribution chambers and inlets and outlets, case D. In this case the relative standard deviation is decreased by a factor of 4 and the pressure drop is reduced by 30%.

It is thus important to increase the cross-section of the flow distribution area compared to the cross-section of the channel region, as was also shown by Choi et al. [10]. The average cross-sectional area of the flow in the flow distribution chambers depends on the width of both the inlet and outlet and the channel area, and also on the position of the inlet and outlet with respect to the channels. An inlet in the middle of the plate in line with the channels increases the average cross-sectional area, where an inlet from the side reduces it. The width of the inlet and outlet is especially important, as is also shown in the previous case by the large pressure drop located close to the inlet and outlet. Ideally, the width of the inlet should be increased to the full width of the plate. However, this is not possible for a counter-current heat exchanger,

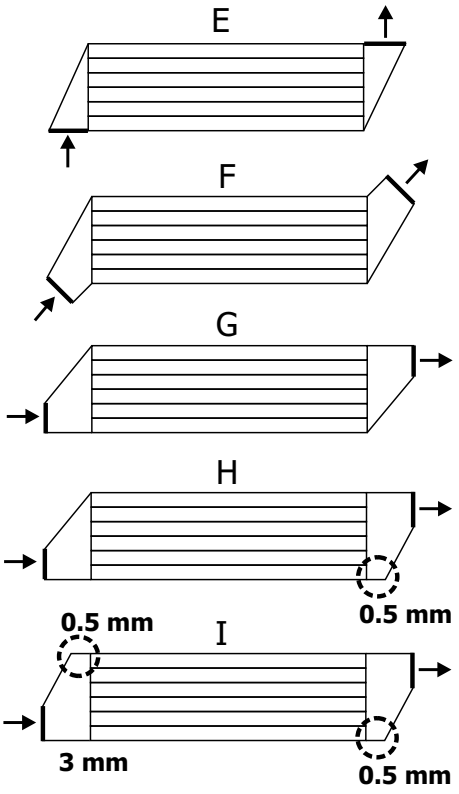

Figure 5.9: Five different geometries of which the flow distribution is studied. All geometries have equal channels (19 channels of (w×h×l) 0.4 × 0.3 × 40 mm^3), equal plate width (12 mm), equal plate height (0.3 mm), and equal inlet size (4 mm). The flow distribution regions at the inlet and outlet are symmetrical for geometries E, F, G, and I. In geometries H and I small extra spaces (0.5 mm) are introduced at the outlet of the bottom and inlet of the top channels.

as in this case space is needed for one inlet and one outlet at both sides.

In the next five cases, several different geometries of the flow distribution chambers are studied using the 3D-model with simplified channel region. Although the channel cross section is not changed, the channels are made a little longer, 40 mm, and the width of the plate is reduced to 12 mm, reducing also the number of channels to 19. In this way the pressure drop over the channels is increased, promoting an even flow distribution, while the pressure drop in the flow distribution chambers, which acts against an even flow distribution, is reduced. The studied geometrical cases are drawn in Figure 5.9. Geometry E has, as in the previous cases, an inlet and outlet located at the side of the plate, but in this case the inlet and outlet use the full width of the flow distribution area and the distribution area has a triangular shape. In geometry F the inlet and outlet are placed at an angle of 45°. In geometries G, H, and I, the inlet and outlet are placed in line with the channels. Geometry H contains a small extra space at the outlet side of the channels, whereas geometry

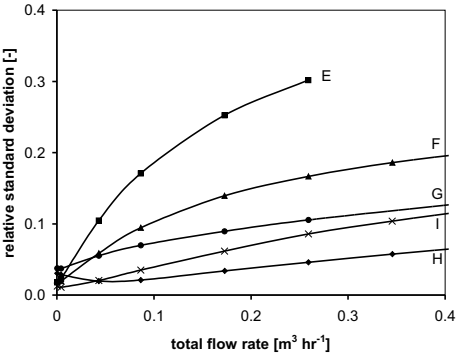

Figure 5.10: Relative standard deviation of the flow distribution as a function of the total gas flow rate for the five plate geometries depicted in Figure 5.9.

I contains extra space at both sides of the channels.

The results of these five cases are shown in Figure 5.10. At low flow rate the relative standard deviation of the five cases increases in the order I $<$ F $<$ E $<$ H $<$ G, ranging from 1 to 4%. However, above a transitional flow rate of 0.005 m^3 hr^{-1} the relative standard deviation increases fast for cases E and F. The decrease in flow distribution quality at higher flow rates is due to an overshoot of the bottom channels and excessive flow through channels further from the inlet, caused by inertia of the gas. The other three cases, G, H, and I, all show improved behavior at higher flow rates, meeting the design target of $\sigma_r < 10\%$ at a flow rate of 0.12 m^3 hr^{-1}. In the latter three cases the position of the inlet directs the flow towards the bottom channels, increasing the flow through these channels. Geometry H produces the best results, as flow through the bottom channels is further promoted by the extra space at the end of these channels. This effect is reduced in case I with extra space also at the beginning of the top channels. As geometry H is not symmetrical like the other geometries, a minimum relative standard deviation is observed at 0.06 m^3 hr^{-1}. At this flow rate the inertia effect counterbalances the asymmetry of the geometry.

These cases show that it is important to consider the fluid flow rate when designing a microchannel reactor for even flow distribution. Moreover, the plate geometry can be optimized for a specific fluid flow rate by adjusting the extra space at the outlet of the bottom channels as is shown in case H.

5.5 Conclusions

The distribution of fluid flow over a set of microchannels was calculated using a three-dimensional laminar CFD model. A simplified description of the channel region, by introducing an artificial viscosity, reduced the calculation time by a factor of 7 compared to a model using an exact representation of the channels. Simulations showed that, depending on the inlet velocity, two flow regimes exist. At low flow rates, below 30 m s^{-1}, the flow distribution is completely determined by wall friction and the distribution's relative standard deviation is independent of flow rate. At flow rates above a transitional velocity, which value is geometry dependent, inertia effects start to influence the flow distribution. Doubling the cross-sectional area of the inlets and outlets and doubling the length of the channels reduced the flow distribution's standard deviation by a factor of 4 and 1.7, respectively. The best results were obtained for a case with inlets and outlets in-line with the channels and asymmetrical flow distribution chambers, case H, with a relative standard deviation of 3% at a flow rate of 0.12 m^3 hr^{-1}.

Nomenclature

C_{drag}	drag coefficient
d_p	plate distance
F	flow rate
n	number of channels
p	pressure
$\mathbf{v}$	gas velocity
μ	viscosity
σ_r	relative standard deviation

Acknowledgements

The authors gratefully acknowledge the European Commission for funding the Micro Reactor Technology for Hydrogen and Electricity (MiRTH-e) project within the Fifth Framework Programme under contract number ENK6-2000-00110. Furthermore, we would like to acknowledge the contributions of our

project partners: Vania Cominos and Chistian Hofmann of the Institut für Mikrotechnik Mainz GmbH (IMM, Germany) and Paul Cobden of the Energy Research Center of the Netherlands (ECN).

Bibliography

[1] W. Ehrfeld, V. Hessel, and H. Löwe. *Microreactors: new technology for modern chemistry*. Wiley-VCH, Weinheim, Germany, 2000.

[2] K. F. Jensen. Microreaction engineering — is small better? *Chem. Eng. Sci.*, 56:293–303, 2001.

[3] H. Kestenbaum, A. Lange de Oliveira, W. Schmidt, F. Schüth, W. Ehrfeld, K. Gebauer, H. Löwe, T. Richter, D. Lebiedz, I. Untiedt, and H. Züchner. Silver-catalyzed oxidation of ethylene to ethylene oxide in a microreaction system. *Ind. Eng. Chem. Res.*, 41:710–719, 2002.

[4] E. V. Rebrov, S. A. Duinkerke, M. H. J. M. de Croon, and J. C. Schouten. Optimization of heat transfer characteristics, flow distribution, and reaction processing for a microstructured reactor/heat-exchanger for optimal performance in platinum catalyzed ammonia oxidation. *Chem. Eng. J.*, 93: 201–216, 2003.

[5] M. Janicke, A. Holzwarth, M. Fichtner, K. Schubert, and F. Schüth. A microstructured catalytic reactor/heat exchanger for the controlled catalytic reaction between H_2 and O_2. *Stud. Surf. Sci. Catal.*, 130:437–442, 2000.

[6] G. Veser. Experimental and theoretical investigation of H_2 oxidation in a high-temperature catalytic microreactor. *Chem. Eng. Sci.*, 56:1265–1273, 2001.

[7] S. Walter, G. Frischmann, R. Broucek, M. Bergfeld, and M. Liauw. Fluid dynamics in microchannel reactors. *Chem. Ing. Tech.*, 71:447–455, 1999.

[8] M. K. Bassiouny and H. Martin. Flow distribution and pressure drop in plate heat exchangers – I. *Chem. Eng. Sci.*, 39:693–700, 1984.

[9] M. K. Bassiouny and H. Martin. Flow distribution and pressure drop in plate heat exchangers – II. *Chem. Eng. Sci.*, 39:701–704, 1984.

[10] S. H. Choi, S. Shin, and Y. I. Cho. The effect of area ratio on the flow distribution in liquid cooling module manifolds for electronic packaging. *Int. Comm. Heat Mass Transfer*, 20:221–234, 1993.

[11] J. M. Commenge. *Réacteurs Microstructurés: Hydrodynamique, Thermique, Transfert de Matière et Applications aux Procédés*. PhD thesis, Institut National Polytechnique de Lorraine, Nancy, France, 2001.

[12] J. M. Commenge, L. Falk, J. P. Corriou, and M. Matlosz. Optimal design for flow uniformity in microchannel reactors. *AIChE J.*, 48:345–358, 2002.

[13] E. R. Delsman, E. V. Rebrov, M. H. J. M. de Croon, J. C. Schouten, G. J. Kramer, V. Cominos, T. Richter, T. T. Veenstra, A. van den Berg, P. D. Cobden, F. A. de Bruijn, C. Ferret, U. d'Ortona, and L. Falk. MiRTH-e:

Micro Reactor Technology for Hydrogen and Electricity. In M. Matlosz, W. Ehrfeld, and J. P. Baselt, editors, *Proceedings of the Fifth International Conference on Microreaction Technology*, pages 268–274. Springer Verlag, Berlin, Germany, 2001.

[14] A. Beskok, G. E. Karniadakis, and W. Trimmer. Rarefaction and compressibility effects in gas microflows. *Trans. ASME, J. Fluids Engng.*, 118: 448–456, 1996.

[15] Y. Asako, T. Pi, S. E. Turner, and M. Faghri. Effect of compressibility on gaseous flows in micro-channels. *Int. J. Heat Mass Transfer*, 46:3041–3050, 2003.

[16] R. B. Bird, W. E. Steward, and E. N. Lightfoot. *Transport Phenomena*. John Wiley & Sons, New York, USA, 2nd edition, 2002.

The influence of differences between microchannels on microreactor performance

6

This chapter has been published as:

E.R. Delsman, M.H.J.M. de Croon, G.D. Elzinga, P.D. Cobden, G.J. Kramer, and J.C. Schouten. The influence of differences between microchannels on microreactor performance. *Chem. Eng. Technol.*, 28:367–375, 2005.

Abstract

Microstructured reactors most often contain a large number of micrometer-sized, parallel channels, instead of a large undivided reaction volume. Individual microchannels behave as plug-flow reactors without significant axial dispersion and with excellent heat and mass transfer properties. However, since the reaction takes place in a large number of parallel channels, it is important that all channels provide equal residence time and amount of catalyst volume. These issues depend not only on the flow distributor design, but also, for example, on the manufacturing tolerances. Correlations are derived to express the conversion of a multichannel microreactor explicitly as a function of the variance of a number of reactor parameters, viz. the channel flow rate, the channel diameter, the amount of catalyst in a channel, and the channel temperature. It is shown that the influence of flow maldistribution on the overall reactor conversion is relatively small, while the influence of variations in the channel diameter and the amount of catalyst coating are more pronounced. The model outcomes are also compared to experimental results of two microreactors with different catalyst distributions, which shows that the presented method is able to provide a quick, though rough, estimation of the influence of differences between channels on microreactor performance.

6.1 Introduction

Microreactors are miniaturized chemical reaction systems, which contain reaction channels with a typical diameter of 10–500 µm, see for example Figure 6.1. The small channel dimensions lead to a relatively large surface area-to-volume ratio and increased driving forces for heat and mass transport [1–3]. Microreactors are especially suited for fast reactions with a large heat effect, where they allow for nearly isothermal conditions at high reactant concentrations, which is not possible in large scale equipment [4, 5]. The possibility of fast mixing of reactants and fast heating and cooling of the reaction mixture, enables precise control of reaction time, improving the yield of reaction intermediates and reducing by-product formation [6–10].

However, there are also problems to be solved. Due to the small volume of a single channel, many parallel channels have to be used to obtain sufficient production, which makes uniform distribution of the reaction mixture over thousands or even millions of channels necessary [11]. Since flow maldistribution can affect the reactor performance [12, 13], several authors have presented design studies of flow distribution manifolds [14–17]. Commenge [18] went a step further and developed a model to quantify the effect of a given flow distribution on the resulting residence time distribution of a compete microreactor consisting of many channels. He found that the flow distribution over the individual microchannels had little effect on the apparent residence time distribution of the reactor. However, besides the design of the

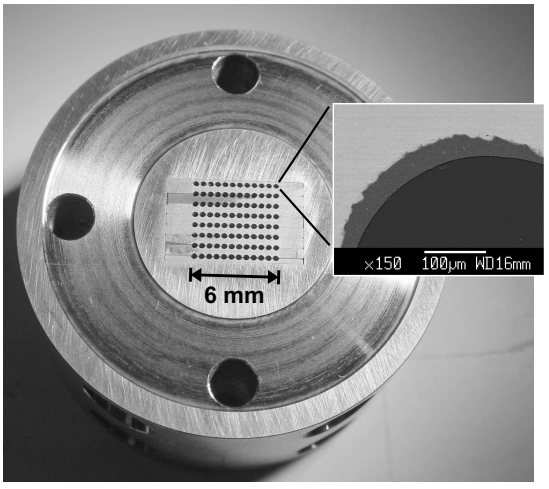

Figure 6.1: Example of a microreactor containing 96 microchannels with a diameter of 400 µm and a length of 1.5 cm. The inlay shows a detail of a microchannel coated with a 35 µm thick catalyst layer.

flow distributor, also manufacturing tolerances on, for example, the diameter of the microchannels and the applied amount of catalyst coating, and issues like channel blockage influence the flow distribution [8, 19].

In this paper a method is presented to predict the influence of flow maldistribution and manufacturing imperfections on the performance of a microreactor containing a large number of parallel channels. With this method limits can be defined on what flow distribution and manufacturing tolerances are acceptable for a specific microreactor application. In the method, a variable system parameter, for example the channel diameter, whose influence on the reactor performance is studied, is treated as a random parameter with a specific mean value and standard deviation. A standard plug-flow reactor model is used to specify the relationship between this parameter and the conversion or selectivity in a single microchannel. Finally, a summation over an infinite number of these microchannels provides a relationship between the variable system parameter and the overall microreactor performance.

In the first part of this paper, the method is explained in detail for a first order heterogeneously catalyzed reaction, performed in a microreactor with a variable channel diameter. Correlations are derived to express pressure drop, channel flow rate and residence time, and the conversion of a multichannel microreactor as a function of the mean channel diameter and its standard deviation. In the second part of the paper, the method is applied to a number of cases, showing the influence of variations in channel diameter, catalyst coating thickness, and temperature on the conversion and selectivity of a microreactor. Finally, the method predictions are compared to experimental results with specially prepared microreactors that contain differences in the amount of catalyst coating per set of channels.

6.2 Method description

6.2.1 Assumptions

In the method a number of assumptions is made:

1. The number of channels is large, i.e. more than 30. In general this is a reasonable assumption, since microreactors may contain hundreds to thousands of channels.
2. The deviations from the mean value of a parameter, e.g. the channel diam-

eter, are considered to be small compared to that mean value; typically the relative variance is smaller than 0.02.

3. The flow through the channels is a developed laminar flow owing to the low Reynolds number ($Re_d \approx 1$) and long channel length/diameter ratio ($L/d \approx 100$).
4. The flow distribution over the microchannels is not influenced by the flow distribution manifolds, which implies that the pressure drop is equal for all channels.
5. The axial dispersion in the microchannels is negligible and no radial concentration profile exists, which allows for a plug-flow model to be used to describe the reactor conversion.

Raja et al. [20] formulated criteria for the applicability of a plug-flow model for a monolith reactor:

$$\frac{d}{L} \ll Re_d Sc \ll \frac{L}{d} \tag{6.1}$$

with d the diameter and L the length of a channel, Re_d the Reynolds number based on the channel diameter, and Sc the Schmidt number. The left end of the equation defines a criterion for neglecting axial dispersion. The right end defines a criterion for neglecting radial concentration variations. For a gas phase microreactor usually both criteria are satisfied. For a liquid phase reactor, unless the channel diameter is very small (< 10 µm), radial concentration gradients might exist, due to the slower liquid-phase diffusion.

6.2.2 Pressure drop

The pressure drop over a set of parallel channels is a function of both the mean channel diameter and the variance of the diameter, as a result of the non-linear relation between pressure drop and channel diameter. The total volumetric flow rate through the reactor ($F_{V,\mathrm{tot}}$) can be expressed as a function of the pressure drop (Δp) and the channel diameter (d_i):

$$F_{V,\mathrm{tot}} = \sum_i F_{V,i} = \sum_i A_{\perp,i}\, v_i = \sum_i \left(\frac{\pi}{4} d_i^2 \cdot \frac{\Delta p}{32 \mu L} d_i^2 \right) = \frac{\pi \Delta p}{128 \mu L} \sum_i d_i^4 \tag{6.2}$$

with $A_{\perp,i}$ the cross sectional area and v_i the fluid velocity in channel i, μ the fluid viscosity, and L the channel length.

When d_i is expressed as the sum of the mean channel diameter and the deviation from the mean value, i.e. $d_i = \bar{d} + \epsilon_i$, the summation in the last part

of equation (6.2) can be rewritten as:

$$\sum_i d_i^4 = \sum_i (\bar{d} + \epsilon_i)^4 = \sum_i \bar{d}^4 \left(1 + 4\frac{\epsilon_i}{\bar{d}} + 6\frac{\epsilon_i^2}{\bar{d}^2} + 4\frac{\epsilon_i^3}{\bar{d}^3} + \frac{\epsilon_i^4}{\bar{d}^4}\right)$$
$$= n\bar{d}^4 \left(1 + 6\frac{\sigma^2}{\bar{d}^2} + \mathcal{O}^3\right) \tag{6.3}$$

with n the number of channels and σ the standard deviation of the channel diameter. The number of channels is assumed to be large (typically larger than 30), so that the sample standard deviation is equal to the population standard deviation, i.e. $\sigma = \sum_i \epsilon_i^2/n$. The summation of ϵ_i is dropped from the equation, since it is zero by definition. If the distribution of the channel diameters is symmetric around the mean value, the summation of ϵ_i^3 is also zero, which then results in fourth order precision of the approximation.

Combining equations (6.2) and (6.3) gives an expression for the pressure drop as a function of the mean channel diameter and its variance:

$$\Delta p = \frac{128\mu F_{V,\text{tot}} L}{\pi \sum_i d_i^4} \approx \frac{128\mu F_{V,\text{tot}} L}{\pi n \bar{d}^4 \left(1 + 6\hat{\sigma}_d^2\right)} \tag{6.4}$$

with $\hat{\sigma}_d$ the relative standard deviation of the channel diameter ($\hat{\sigma}_d = \sigma_d/\bar{d}$). This equation shows that a variation of the channel diameter results in a decrease in the total pressure drop, when the total flow rate is kept constant. Although the channel diameter is present to a fourth order in the pressure drop equation, a small variation on the channel diameter does not result in a large difference in the pressure drop. For example, a standard deviation of 10% on the channel diameter results in a pressure drop that is only 6% lower than in the case of identical channels. However, the effect on the flow rate of individual channels is much larger.

6.2.3 Channel flow rate

The molar flow rate of a component A through a channel with a variable channel diameter and without a reaction taking place, can be described as:

$$F_{\text{A0},i} = C_{\text{A0}} F_{V,i} = C_{\text{A0}} \frac{\pi \Delta p}{128\mu L} d_i^4 = \frac{C_{\text{A0}} F_{V,\text{tot}}}{n(1 + 6\hat{\sigma}_d^2)} \cdot \frac{d_i^4}{\bar{d}^4} \tag{6.5}$$

with C_{A0} the concentration of component A at the inlet of the reactor. Since the channel flow rate scales with the channel diameter to the fourth power, relative deviations in the flow rate are larger than relative deviations in the channel diameter. The relative standard deviation of the channel flow rates can be estimated, for $\epsilon_i \ll \bar{d}$, by expanding $(\bar{d} + \epsilon_i)^4$ like is shown in the third part of equation (6.3). When all terms higher than first order in ϵ_i are neglected, the factor 4 in front of ϵ_i indicates that (relative) deviations in the channel flow rate are four times larger than deviations in the channel diameter. When the channel diameters are assumed to be normally distributed with mean $\bar{d}$ and $\hat{\sigma}_d = 0.1$, then 95% of the channels will have a flow rate between 39 and 193% of the average flow through the channels.

6.2.4 Reactor conversion

The influence of a variable channel diameter on the conversion of a microreactor is found by first developing an equation for the conversion of a single microchannel and then extending the equation to a set of microchannels. As an example, a heterogeneous first order reaction A $\rightarrow$ B is considered with rate constant k (mol kg_{cat}^{-1} s^{-1}). The microchannel conversion is described by a plug-flow reactor model. Using equation (6.5) for the inlet flow rate of a single channel, and assuming the catalyst to be equally distributed over all channels, the molar flow rate of A at the exit of the channel, $F_{Ae,i}$ (mol s^{-1}), can be expressed as:

$$F_{Ae,i} = F_{A0,i} e^{-k \cdot W_{cat}/F_{A0,i}} = \frac{F_{A0,tot}}{n(1+6\hat{\sigma}_d^2)} \frac{(\bar{d}+\epsilon_i)^4}{\bar{d}^4} e^{-k\tau_0(1+6\hat{\sigma}_d^2)\frac{\bar{d}^4}{(\bar{d}+\epsilon_i)^4}} \tag{6.6}$$

with W_{cat} the total amount of catalyst in the reactor and τ_0 the reactor's space time ($\tau_0 = W_{cat}/F_{A0,tot}$). The conversion in 95% of the channels of a reactor with $k\tau_0 = 2$ and $\hat{\sigma}_d = 0.1$, varies between 59 and 99%.

The overall reactor conversion, X, can be calculated by taking the sum of $F_{Ae,i}$ for all channels. This is not straight-forward, since the individual channel diameters, and thus the ϵ_i's, are not known. Therefore, a Taylor expansion is used, which introduces the sum of the deviations and the sum of squares of

the deviations instead of the individual deviations:

$$X = 1 - \frac{\sum_i F_{\mathrm{Ae},i}}{F_{\mathrm{A0,tot}}} = 1 - \frac{nF_{\mathrm{Ae},i}(\epsilon_i = 0)}{F_{\mathrm{A0,tot}}} - \frac{1}{F_{\mathrm{A0,tot}}} \left.\frac{\mathrm{d}F_{\mathrm{Ae},i}}{\mathrm{d}\epsilon_i}\right|_{\epsilon_i=0} \sum_i \epsilon_i - \frac{1}{2F_{\mathrm{A0,tot}}} \left.\frac{\mathrm{d}^2F_{\mathrm{Ae},i}}{\mathrm{d}\epsilon_i^2}\right|_{\epsilon_i=0} \sum_i \epsilon_i^2 - \cdots \quad (6.7)$$

This transformation considerably simplifies matters. Since the sum of deviations of the channel diameter is zero, the first derivative term can be removed from the equation. Moreover, the sum of squares of ϵ_i is equal to n times the variance of the channel diameter, which can therefore be introduced into the equation. Since ϵ_i is assumed to be much smaller than $\bar{d}$, higher order terms are neglected. Substituting equation (6.6) into (6.7) leads to the following result:

$$X = 1 - \frac{\mathrm{e}^{-k\tau_0(1+6\hat{\sigma}_d^2)}}{1+6\hat{\sigma}_d^2} - \frac{12\left[1+k\tau_0\left(1+6\hat{\sigma}_d^2\right)+\frac{4}{3}(k\tau_0)^2\left(1+6\hat{\sigma}_d^2\right)^2\right]\mathrm{e}^{-k\tau_0(1+6\hat{\sigma}_d^2)}}{1+6\hat{\sigma}_d^2} \frac{\sum_i \epsilon_i^2}{2n\bar{d}^2}, \quad (6.8)$$

which, after replacing $\sum_i \epsilon_i^2/n$ with the variance of the channel diameter, leads to

$$X = 1 - \frac{1+6\hat{\sigma}_d^2\left[1+k\tau_0\left(1+6\hat{\sigma}_d^2\right)+\frac{4}{3}(k\tau_0)^2\left(1+6\hat{\sigma}_d^2\right)^2\right]}{1+6\hat{\sigma}_d^2}\mathrm{e}^{-k\tau_0(1+6\hat{\sigma}_d^2)}. \quad (6.9)$$

In the calculation of the second derivative of F_{Ae} in equation (6.7), the standard deviation, $\hat{\sigma}_d$, is assumed to be independent of ϵ_i, which is the case when the number of channels is large.

Equation (6.9) describes the influence of variations of the channel diameter on the conversion in a microreactor as a function of the Damköhler number, $k\tau_0$, of the reactor. In Figure 6.2 the conversion is plotted against the Damköhler number for both an ideal microreactor and a microreactor with variations in the channel diameter ($\hat{\sigma}_d = 0.1$). The figure shows that, although the conversion in individual channels can vary considerably, the effect on the total reactor conversion is smaller. The lower conversion in channels with a larger flow rate is partly compensated by a higher conversion in channels with a lower flow rate. Due to the non-linear relation between the channel diameter and the flow rate, the effects do not cancel completely and a decrease in reactor conversion is observed.

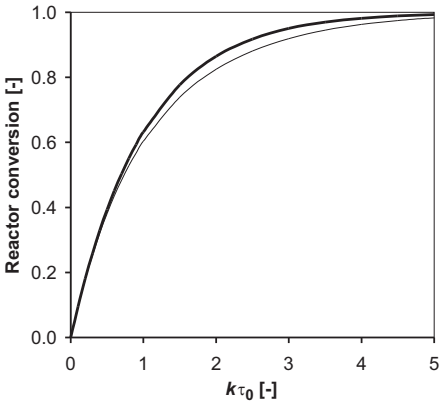

Figure 6.2: Influence of channel diameter variations on the reactor conversion; ideal reactor (thick line), reactor with $\hat{\sigma}_d = 0.1$ (thin line).

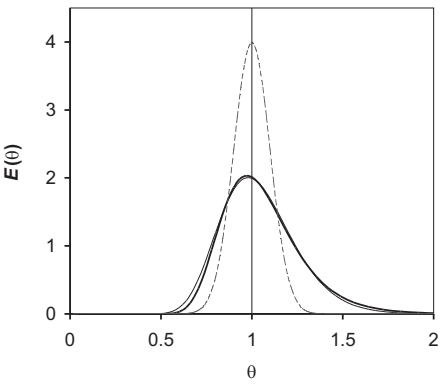

Figure 6.3: Scaled residence time distribution (thick line) of a microreactor with a variable channel diameter with $\hat{\sigma}_d = 0.1$ (dashed line); the residence time distribution of a vessel with axial dispersion and a Péclet number of 50 is indicated as the thin line [21].

6.2.5 Residence time

The residence time of a fluid in a microchannel also varies between the channels when the channel diameter is variable. The residence time in a single channel is a function of both the channel flow rate and the channel volume and can be expressed as:

$$\tau_i = \frac{V_i}{F_{V,i}} = \frac{\frac{\pi}{4} d_i^2 L \cdot 128 \mu L}{\pi d_i^4 \Delta p} = \frac{V_0}{F_{V,\text{tot}}} \frac{n\bar{d}^4(1+6\hat{\sigma}_d^2)}{n\bar{d}^2 \cdot d_i^2} = \tau_0(1+6\hat{\sigma}_d^2) \cdot \frac{\bar{d}^2}{d_i^2} \quad (6.10)$$

with V_0 the total channel volume of a perfect microreactor, of which all channels have a diameter $\bar{d}$, and τ_0 the residence time of the perfect microreactor.

Since the residence time varies between the channels, a tracer pulse at the inlet of the microreactor will be broadened, as would be the case for a tubular reactor with dispersion. Although the dispersion mechanisms are different, the extent of peak broadening in a microreactor and a tubular reactor with dispersion can be compared, which makes it possible to calculate an approximate Péclet number for the microreactor case. In a first approximation, the relative standard deviation in the residence time is two times the relative standard de-

viation in the channel diameter. Since the relative variance of the residence time is approximately equal to $2/Pe_r$ [21], this leads to:

$$\hat{\sigma}_\tau^2 \approx (2\hat{\sigma}_d)^2 \approx \frac{2}{Pe_r} \quad \rightarrow \quad Pe_r \approx \frac{1}{2\hat{\sigma}_d^2} \tag{6.11}$$

with Pe_r the reactor Péclet or Bodenstein number. The residence time distribution in a microreactor with $\hat{\sigma}_d = 0.1$ is thus comparable to a tubular reactor with axial dispersion and a Péclet number of 50. In Figure 6.3 the distribution of the scaled residence time, $\theta = \tau/\bar{\tau} = \tau/\tau_0(1 + \hat{\sigma}_d^2)$, is compared to the residence time distribution in a vessel with axial dispersion and $Pe_r = 50$.

6.3 Several applications of the method

6.3.1 Reactor conversion

The method described in the previous section can be used to estimate the performance of a multi-channel microreactor as a function of variations in various reactor parameters. Table 6.1 shows formulas for the channel flow rate, the channel residence time, and the reactor conversion in six different cases, including, for reference, an ideal microreactor with all identical channels (case A). In all cases plug-flow behavior in the channels and first order kinetics are assumed, although the method can also be applied to different kinetics. The relative deviation from the ideal reactor conversion (ξ) is plotted for the various cases in Figure 6.4 as a function of the Damköhler number ($k\tau_0$), where

$$\xi = \frac{X}{X_{\text{ideal}}} \,. \tag{6.12}$$

The relative standard deviation of the variable system parameter is 0.1 for cases B–E. For case F a lower value of 0.01 is used, since the effect of temperature variations is more pronounced than in the other cases and temperature variations are usually much smaller than 10%.

Influence of the flow distribution

Case B is a case where all channels are identical, but the inlet flow rate per channel varies, for example as a result of flow maldistribution introduced by the flow distribution manifolds. As is shown in Figure 6.4, the influence of

Table 6.1: Channel flow rate and residence time, and overall reactor conversion for a selection of cases: ideal microreactor (A), ideal channels, but variation on flow distribution (B), variation on channel diameter, heterogeneous case (C) and homogeneous case (D), variation on coating thickness (E), and variation on temperature (F). Parameter definitions: $\alpha = 2\bar{h}/\bar{d}$ and $\gamma = E_a/(R\bar{T})$.

case	$F_{A0,i}$	$(k\tau)_i$	$X(\widetilde{k\tau}, \hat{\sigma})$, where $\widetilde{k\tau} = (k\tau)_i(\epsilon_i = 0)$
A	$\bar{F}_{A0}$	$k\tau_0$	$1 - e^{-\widetilde{k\tau}}$
B	$\bar{F}_{A0} + \epsilon_i$	$k\tau_0 \frac{\bar{F}_{A0}}{\bar{F}_{A0} + \epsilon_i}$	$1 - \left(1 + \frac{1}{2}(\widetilde{k\tau})^2 \hat{\sigma}_F^2\right) e^{-\widetilde{k\tau}}$
C	$\frac{\bar{F}_{A0}}{1 + 6\hat{\sigma}_d^2} \frac{(\bar{d} + \epsilon_i)^4}{\bar{d}^4}$	$k\tau_0(1 + 6\hat{\sigma}_d^2) \frac{\bar{d}^4}{(\bar{d} + \epsilon_i)^4}$	$1 - \frac{1 + 6\hat{\sigma}_d^2 \left[1 + \widetilde{k\tau} + \frac{4}{3}(\widetilde{k\tau})^2\right]}{1 + 6\hat{\sigma}_d^2} e^{-\widetilde{k\tau}}$
D	$\frac{\bar{F}_{A0}}{1 + 6\hat{\sigma}_d^2} \frac{(\bar{d} + \epsilon_i)^4}{\bar{d}^4}$	$k\tau_0(1 + 6\hat{\sigma}_d^2) \frac{\bar{d}^2}{(\bar{d} + \epsilon_i)^2}$	$1 - \frac{1 + 6\hat{\sigma}_d^2 \left[1 + \frac{5}{6}\widetilde{k\tau} + \frac{1}{3}(\widetilde{k\tau})^2\right]}{1 + 6\hat{\sigma}_d^2} e^{-\widetilde{k\tau}}$
E	$\frac{\bar{F}_{A0}}{1 + \frac{\alpha^2 \hat{\sigma}_W^2}{(1-\alpha)^2}} \left(\frac{\bar{W} - \alpha(\bar{W} + \epsilon_i)}{\bar{W} - \alpha\bar{W}}\right)^2$	$k\tau_0 \left(1 + \frac{\alpha^2 \hat{\sigma}_W^2}{(1-\alpha)^2}\right) \frac{\bar{W} + \epsilon_i}{\bar{W}} \left(\frac{\bar{W} - \alpha\bar{W}}{\bar{W} - \alpha(\bar{W} + \epsilon_i)}\right)^2$	$1 - \frac{1 + \frac{\alpha^2 \hat{\sigma}_W^2}{(1-\alpha)^2} \left[1 + \widetilde{k\tau} + \frac{1}{2}(\widetilde{k\tau})^2 \left(\frac{1+\alpha}{\alpha}\right)^2\right]}{1 + \frac{\alpha^2 \hat{\sigma}_W^2}{(1-\alpha)^2}} e^{-\widetilde{k\tau}}$
F	$\frac{\bar{F}_{A0}}{1 + 3\hat{\sigma}_T^2} \frac{\bar{T}^2}{(\bar{T} + \epsilon_i)^2}$	$k_0\tau_0(1 + 3\hat{\sigma}_T^2) \frac{\bar{T} + \epsilon_i}{\bar{T}} e^{\gamma \frac{\epsilon_i}{\bar{T} + \epsilon_i}}$	$1 - \frac{1 + 3\hat{\sigma}_T^2 \left[1 + \frac{2}{3}\widetilde{k\tau}\left(1 + \gamma - \frac{1}{4}\gamma^2\right) + \frac{1}{6}(\widetilde{k\tau})^2(1+\gamma)^2\right]}{1 + 3\hat{\sigma}_T^2} e^{-\widetilde{k\tau}}$

small differences in the flow rate per channel on the overall reactor conversion is small. Since the effect of small variations in the channel flow rates on the conversion is nearly linear, the higher conversion in channels with a lower flow rate compensates for the channels with a higher flow rate. This result does not imply that a proper design of the flow distribution manifolds is not important: a bad design can actually result in large flow deviations ($\hat{\sigma}_F > 0.3$), which do have an affect on reactor performance [12]. The method presented here is useful in defining a limit on what flow distribution is to be considered adequate and beyond which point improvements in the flow distributor no longer have an effect on the reactor performance.

Influence of the channel diameter

Cases C and D describe the influence of a variation on the microchannel diameter on the reactor conversion. Case C, which is the case also described in the previous section, represents a heterogeneous reaction case, with equal amounts of catalyst present in each channel. Case D describes a homogeneous reaction case, where both the channel flow rate and the channel volume, i.e. the reaction volume, depend on the channel diameter. The effect of variations in the channel diameter is much larger in case C than in case D. In the homogeneous case D, channels with a larger flow rate also have a larger reaction volume, which reduces the effect on the reactor conversion. Moreover, the variations in the channel diameter result in a larger mean channel volume compared to a reactor with all identical channels, which also explains the increased conversion ($\xi > 1$) at low Damköhler numbers ($k\tau_0 < 0.5$). The combination of both effects makes that in the case of a homogeneous reaction, the conversion is only slightly affected by variations in the channel diameter. For the heterogeneous case, however, variations in the channel diameter do affect the reactor conversion, with a maximum effect at $k\tau_0 = 1.5$.

Influence of the amount of catalyst

Case E also describes a heterogeneous reaction. In this case the diameters of the microchannels are equal, whereas the amount of catalyst (W) varies between the channels. The catalyst is applied as a coating on the channel wall. Variations in the amount of catalyst results in variations in the catalyst coating thickness, which in turn influences the diameter of the open channel and thus

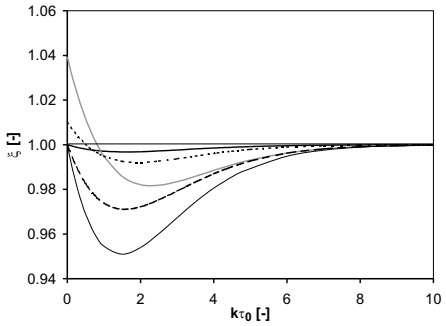

Figure 6.4: Influence of variations ($\hat{\sigma} = 0.1$) between channels on the reactor conversion: case B (thick line), case C (thin line), case D (dotted line), case E (dashed line, $\alpha = 0.5$), and case F (gray line, $\hat{\sigma} = 0.01$, $\gamma = 30$).

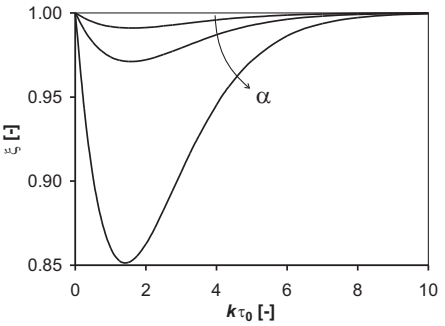

Figure 6.5: Influence of the parameter α on the conversion in microreactor case E, with $\hat{\sigma}_W = 0.1$; α = 0.25, 0.5, 0.75.

the channel flow rate. The formulas for the flow rate and space time are shown in Table 6.1. A parameter α is introduced, which is the average volume fraction of catalyst coating in the channels. The space time τ_0 (in $\mathrm{kg_{cat}\ s\ mol^{-1}}$) is the total amount of catalyst divided by the total molar flow rate of the reacting component A.

Variations in the amount of catalyst coating might be expected to have a pronounced effect on the conversion, since channels with the smallest amount of catalyst will receive the largest amount of flow. However, Figure 6.4 shows that, for α = 0.5, the influence of variations in the amount of catalyst is smaller than the influence of variations in the channel diameter (case C). When the volume fraction of catalyst is low, variations in the amount of catalyst do not influence the channel flow rate, and the channel conversion, as much as variations in the channel diameter. Figure 6.5 shows the influence of the parameter α on the reactor conversion for $\hat{\sigma}_W = 0.1$. For small values of α the influence of variations in the amount of catalyst are moderate, but for higher values their influence is pronounced. This puts a practical limit on the volume fraction of catalyst that can be coated in a channel depending on the accuracy of the used coating process. For example, if for a coating process $\hat{\sigma}_W = 0.1$, then the volume fraction of catalyst in the microchannels should be limited to 60% to avoid deviations in the microreactor conversion larger than 5%.

Influence of the temperature

In the last case we present here, case F, the channel diameter and the amount of catalyst per channel are equal for all channels, but the temperature varies between the channels. The temperature affects both the molar gas flow rate in a channel and the reaction rate coefficient. The temperature dependence of the flow rate is dependent on the type of fluid, which in this case is a gas. It is assumed that the viscosity of the gas is proportional to the temperature T and that the density is proportional to $1/T$. Assuming Arrhenius behavior, the reaction rate coefficient is proportional to $\exp[-\gamma(\bar{T}/T_i)]$, with $\gamma = E_a/(R\bar{T})$, where E_a is the activation energy and R the gas constant. Since the heat transfer in microchannels is very effective, it is assumed that the gas temperature equals the channel temperature. It is also assumed that a single channel has a uniform temperature along its length. These considerations lead to the formulas presented in Table 6.1.

The temperature has a much larger influence on the reactor conversion than, for example, the channel diameter. This is not directly visible in Figure 6.4, since a ten times lower relative standard deviation is used in case F than for the other cases. However, relative temperature differences are usually not very large, especially in microreactors. The used relative standard deviation of 1% corresponds, for a reactor at 250 °C, with variations of $\pm$ 10 °C. The influence of temperature deviations on the conversion is dependent on the activation energy of the reaction. Figure 6.6 shows the influence of the parameter γ on the reactor conversion. The influence of the temperature increases with an increase in the parameter γ, which means for reactions with a high activation energy and/or a low reaction temperature. Since the deviations are largest at low Damköhler numbers, care must be taken when using microreactors for kinetic studies at fractional conversions.

6.3.2 Reactor selectivity

One of the benefits of microreactors is the possibility to accurately control the residence time, also for short millisecond residence times [11]. In a consecutive reaction scheme, this allows for the reaction to be stopped at a point where the yield of an intermediate product is highest. In this section the influence of variations in channel diameter (case C) on the yield of an intermediate in a

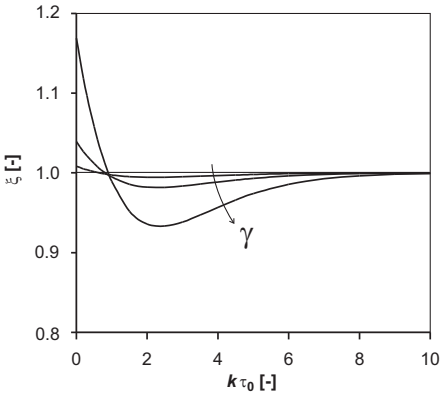

Figure 6.6: Influence of the parameter γ on the conversion in microreactor case F with $\hat{\sigma}_T = 0.01$; γ = 15, 30, and 60.

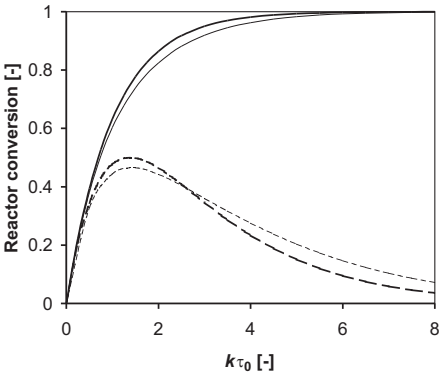

Figure 6.7: Conversion of component A (full lines) and yield of component B (dashed lines) as a function of the residence time for an ideal reactor (thick lines) and a non-ideal microreactor with $\hat{\sigma}_d = 0.1$ and $K = 0.5$ (thin lines).

consecutive reaction scheme is studied. The reaction system is:

$$\mathrm{A} \xrightarrow{k_1 C_\mathrm{A}} \mathrm{B} \xrightarrow{k_2 C_\mathrm{B}} \mathrm{C} \tag{6.13}$$

where k_1 and k_2 are the first order reaction rate coefficients for the formation of B and C. Both reactions are first order in the reactant. Assuming plug-flow behavior in the reaction channels, the yield of B in a random channel is

$$Y_{\mathrm{B},i} = \frac{F_{\mathrm{Be},i}}{F_{\mathrm{A0},i}} = \frac{1}{K-1}\left(\mathrm{e}^{-k_1\tau_i} - \mathrm{e}^{-Kk_1\tau_i}\right) \tag{6.14}$$

with $K = k_2/k_1$. For heterogeneously catalyzed reactions with the catalyst equally distributed over the channels, which vary in diameter, the yield of B is found to be

$$Y_\mathrm{B} = \frac{1}{K-1}\cdot\left\{\frac{\mathrm{e}^{-\widetilde{k_1\tau}} - \mathrm{e}^{-K\widetilde{k_1\tau}}}{1+6\hat{\sigma}_d^2} + \frac{6\hat{\sigma}_d^2}{1+6\hat{\sigma}_d^2}\cdot\right.$$
$$\left.\cdot\left[\left(1+\widetilde{k_1\tau}+\tfrac{4}{3}(\widetilde{k_1\tau})^2\right)\mathrm{e}^{-\widetilde{k_1\tau}} - \left(1+K\widetilde{k_1\tau}+\tfrac{4}{3}(K\widetilde{k_1\tau})^2\right)\mathrm{e}^{-K\widetilde{k_1\tau}}\right]\right\} \tag{6.15}$$

with $\widetilde{k_1\tau} = k_1\tau_0(1 + 6\hat{\sigma}_d^2)$.

The results are plotted in Figure 6.7 for a case where K = 0.5 and $\hat{\sigma}_d = 0.1$. Compared to an ideal microreactor, the maximum yield of component B is lower, comparable to the case of a plug-flow reactor with dispersion. Appropriate design of the reactor and sufficiently precise manufacturing methods are thus required to fulfill the promise of microreactors to the fullest. In this example, the maximum yield of component B is decreased from 50% to 46%, as a result of the variable channel diameter with $\hat{\sigma}_d = 0.1$.

6.4 Comparing model and experiment

6.4.1 The experiment

An experiment has been performed to test the proposed method. In the experiment a microreactor is used, which contains a stack of exchangeable microstructured plates [22]. The microstructured plates each contain forty channels of semi-circular cross-section with a radius of 250 µm and a length of 5 cm. The channel walls are coated with a Pt-Co/Al_2O_3 catalyst, which is a catalyst for the preferential oxidation of carbon monoxide in a hydrogen-rich gas stream. On the catalyst, oxygen reacts with CO and H_2 to form CO_2 and H_2O. This reaction is used to remove carbon monoxide from a hydrocarbon reformate stream before it can be used to feed a fuel cell [23].

The experiment consists of two microreactor runs, each with two coated microstructured plates. In the first run, the two plates were coated with approximately equal amounts of catalyst, viz. 127 and 132 mg ($\hat{\sigma}_W = 0.02$). In the second run, the two plates were coated with different amounts of catalyst, viz. 100 and 144 g ($\hat{\sigma}_W = 0.2$). The catalyst distribution over the channels is thought to be uniform on a single plate. In both runs, the two plates were installed in the microreactor and tested for several hours at a temperature of 150 °C, using a simulated reformate gas mixture containing 0.5% CO, 0.5% O_2, 19% CO_2, 37% H_2, 15% H_2O, and balance N_2. The flow rate was adjusted to provide equal space time in both experiments, which was 1.25 mg_{cat} min ml_{gas}^{-1}.

The results of the experiment is presented in Figure 6.8, where the conversion for the two microreactors is plotted as a function of the time-on-stream. The reactor with equal amounts of catalyst on the plates (♦) shows both a

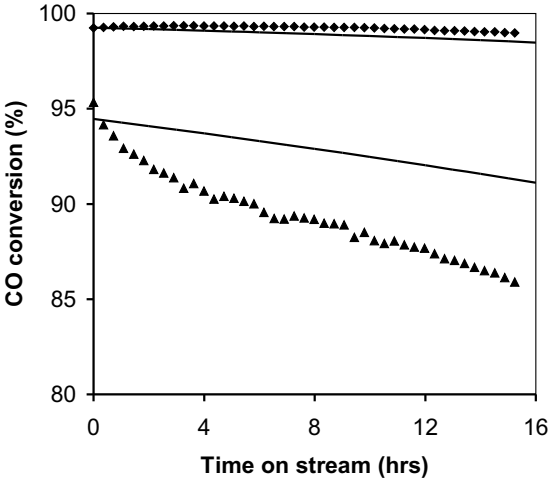

Figure 6.8: CO conversion in two eighty channel microreactors; one with an approximately equal amount of catalyst in the channels, $\hat{\sigma}_W = 0.02$ (♦), and one with a maldistribution in catalyst loading, $\hat{\sigma}_W = 0.2$ (▲). The lines represent the model results.

higher initial activity and a lower deactivation rate, as compared to the reactor with the different catalyst plates (▲). The catalyst maldistribution thus has a significant negative effect on the performance of the microreactor system.

6.4.2 The model

Since in the experiment the amount of catalyst is varied, the results are described using the model case E. Several kinetic mechanisms have been developed for this reaction with varying reaction orders in both oxygen and carbon monoxide [23]. We assume here that the reaction is first order in oxygen, zero order in carbon monoxide, and has a constant selectivity of oxygen to carbon dioxide of 50%. Since oxygen and carbon monoxide are fed at equal rates, their concentrations remain equal throughout the reactor. The reaction rate of carbon monoxide is then described by the first order power law

$$-r_{\mathrm{CO}} = k \cdot C_{\mathrm{O_2}} = k \cdot C_{\mathrm{CO}} \tag{6.16}$$

with k the reaction rate constant and $C_{\mathrm{O_2}}$ and C_{CO} the gas-phase concentrations of oxygen and carbon monoxide.

The catalyst deactivation is assumed to be exponential with respect to time and independent of the species concentrations. Therefore, the deactivation is incorporated in the conversion equation (case E, Table 6.1) by multiplying the reaction rate constant k with $\exp(-k_{\mathrm{d}}t)$, with k_{d} the rate constant for deacti-

vation and t the time-on-stream. The term $\widetilde{k\tau}$ in the conversion equation then becomes:

$$\widetilde{k\tau} = k\tau_0 \left(1 + \frac{\alpha^2 \hat{\sigma}_W^2}{(1-\alpha)^2}\right) \mathrm{e}^{-k_\mathrm{d} t} . \tag{6.17}$$

The mean catalyst volume fraction in the channels (α) is calculated to be 0.64 in both microreactors using a density of the catalyst coating of 1 g ml^{-1}. The relative standard deviation ($\hat{\sigma}_W$) of the first reactor with equal catalyst plates is 0.02, and for the second reactor, which has two different catalyst plates, $\hat{\sigma}_W = 0.2$.

The model results are included in Figure 6.8 as two lines. The reaction and deactivation rate constants are manually adjusted to get an approximate accordance between the experimental and model results. The used values in both cases are $k\tau_0 = 5$ and $k_\mathrm{d} = 0.01$ hr^{-1}. The model lines do not represent a perfect fit of the experimental data, which is, at least partly, due to the simplified description of the reaction and deactivation kinetics used. However, the model does predict the lower conversion and higher deactivation rate found in the experiment for the reactor with the higher variation in catalyst coating thickness. This shows that the presented method is able to provide a quick, though rough, estimation of the influence of variations in manufacturing parameters on the performance of a microreactor.

6.5 Conclusions

A method is presented to estimate the effect of differences between individual microchannels on the performance of a multichannel microstructured reactor. Based on elementary statistics, equations are derived that give the reactor conversion explicitly as a function of the variance of a number of reactor parameters, viz. the channel flow rate, the channel diameter, the amount of catalyst in a channel, and the channel temperature. A comparison between several cases with variations ($\hat{\sigma} = 0.1$) in different reactor parameters shows that the influence of flow maldistribution on the overall reactor conversion is small (effect on conversion $< 0.5\%$), while the influence of variations in channel diameter and amount of catalyst coating are more pronounced (a 3–5% lower conversion). It is also shown that the maximum yield of an intermediate reaction species is decreased by almost 10% as a result of variations in the microchannel diameter. Comparison of the model to an experiment with

two microreactors, which have different catalyst distributions, shows that the model is able to predict the observed differences in reactor conversion and apparent catalyst deactivation rate.

Nomenclature

Roman symbols

$A_\perp$	channel cross-sectional area
C_{A0}	inlet concentration of component A
d_i	diameter of channel i
$\bar{d}$	mean channel diameter
$\mathcal{D}$	diffusion coefficient
$E(\theta)$	expectance of the scaled residence time
E_a	activation energy
F_{A0}	molar inlet flow rate of component A
F_{Ae}	molar flow rate at channel exit
F_V	volumetric flow rate
k	reaction rate coefficient
k_d	deactivation rate coefficient
K	ratio of reaction rate constants (k_2/k_1)
L	channel length
n	number of channels
p	pressure
Pe_r	reactor Péclet number ($vL/\mathcal{D}$)
R	gas constant
Re_d	Reynolds number ($\rho v d/\mu$)
Sc	Schmidt number ($\mu/\rho\mathcal{D}$)
t	time-on-stream
T	temperature
v	fluid linear velocity
V	channel volume
W_{cat}	catalyst mass
X	conversion
Y_B	yield of component B (F_{Be}/F_{A0})

Greek symbols

α	mean volume fraction of catalyst in the channels
γ	Arrhenius number (E_a/RT)
ϵ	deviation from the mean value
θ	scaled residence time ($\tau/\bar{\tau}$)
μ	fluid viscosity
ξ	conversion deviation (X_{real}/X_{ideal})

ρ	fluid density
σ	standard deviation
$\hat{\sigma}_x$	relative standard deviation of parameter 'x' ($\sigma_x/\bar{x}$)
τ	reactor residence or space time
τ_0	residence or space time of the ideal reactor

Subscripts

A, B	of component A, B
d	channel diameter
F	channel flow rate
i	channel number
r	reactor
T	channel temperature
tot	total
W	catalyst mass
τ	residence time

Acknowledgement

The authors gratefully acknowledge funding from the European Commission for the Micro Reactor Technology for Hydrogen and Electricity (MiRTH-e) project under the 'Energy, Environment and Sustainable Development' Programme, contract number ENK6-CT-2000-00110. Furthermore, Vania Cominos and Christian Hofmann of the Institut für Mikrotechnik Mainz GmbH are acknowledged for supplying the microreactor used in the experiments.

Bibliography

[1] H. Löwe and W. Ehrfeld. State-of-the-art in microreaction technology: concepts, manufacturing and applications. *Electrochim. Acta*, 44:3679–3689, 1999.

[2] K. F. Jensen. Microreaction engineering — is small better? *Chem. Eng. Sci.*, 56:293–303, 2001.

[3] V. Hessel, S. Hardt, and H. Löwe. *Chemical Micro Process Engineering — Fundamentals, Modelling and Reactions*. Wiley-VCH, Weinheim, Germany, 2004.

[4] H. Kestenbaum, A. Lange de Oliveira, W. Schmidt, F. Schüth, W. Ehrfeld, K. Gebauer, H. Löwe, T. Richter, D. Lebiedz, I. Untiedt, and H. Züchner. Silver-catalyzed oxidation of ethylene to ethylene oxide in a microreaction system. *Ind. Eng. Chem. Res.*, 41:710–719, 2002.

[5] N. de Mas, A. Günther, M. A. Schmidt, and K. F. Jensen. Microfabricated multiphase reactors for the selective direct fluorination of aromatics. *Ind. Eng. Chem. Res.*, 42:698–710, 2003.

[6] H. Kummradt, U. Koop, and J. Stoldt. Experiences with the use of microreactors in organic synthesis. In W. Ehrfeld, editor, *Proceedings of the Third International Conference on Microreaction Technology*, pages 181–186. Springer, Berlin, Germany, 2000.

[7] V. Skelton, G. M. Greenway, S. J. Haswell, P. Styring, and D. O. Morgan. Micro-reactor synthesis: synthesis of cyanobiphenyls using a modified Suzuki coupling of an aryl halide and aryl boronic acid. In W. Ehrfeld, editor, *Proceedings of the Third International Conference on Microreaction Technology*, pages 235–242. Springer, Berlin, Germany, 2000.

[8] J. Antes, D. Boskovic, H. Krause, S. Loebbecke, N. Lutz, T. Tuercke, and W. Schweikert. Analysis and improvement of strong exothermic nitrations in microreactors. *Chem. Eng. Res. Des.*, 81:760–765, 2003.

[9] R. Maurer and A. Renken. Dehydrogenation of methanol to anhydrous formaldehyde in a microstructured reactor system. *Chem. Eng. Res. Des.*, 81:730–734, 2003.

[10] E. V. Rebrov, S. A. Duinkerke, M. H. J. M. de Croon, and J. C. Schouten. Optimization of heat transfer characteristics, flow distribution, and reaction processing for a microstructured reactor/heat-exchanger for optimal performance in platinum catalyzed ammonia oxidation. *Chem. Eng. J.*, 93: 201–216, 2003.

[11] O. Wörz, K.-P. Jäckel, T. Richter, and A. Wolf. Microreactors—a new efficient tool for reactor development. *Chem. Eng. Technol.*, 24:138–142, 2001.

[12] A. K. Heibel, F. J. Vergeldt, H. van As, F. Kapteijn, J. Moulijn, and T. Boger. Gas and liquid distribution in the monolith film flow reactor. *AIChE J.*, 49:3007–3017, 2003.

[13] H. Hirata and M. Hori. Gas-flow uniformity and cell performance in a molten carbonate fuel cell stack. *J. Power Sources*, 63:115–120, 1996.

[14] S. H. Choi, S. Shin, and Y. I. Cho. The effect of area ratio on the flow distribution in liquid cooling module manifolds for electronic packaging. *Int. Comm. Heat Mass Transfer*, 20:221–234, 1993.

[15] J. M. Commenge, L. Falk, J. P. Corriou, and M. Matlosz. Optimal design for flow uniformity in microchannel reactors. *AIChE J.*, 48:345–358, 2002.

[16] Y. Chen and P. Cheng. Heat transfer and pressure drop in fractal tree-like microchannel nets. *Int. J. Heat Mass Transfer*, 45:2643–2648, 2002.

[17] E. R. Delsman, A. Pierik, M. H. J. M. de Croon, G. J. Kramer, and J. C. Schouten. Microchannel plate geometry optimization for even flow distribution at high flow rates. *Chem. Eng. Res. Des.*, 82:267–273, 2004.

[18] J. M. Commenge. *Réacteurs Microstructurés: Hydrodynamique, Thermique,*

Transfert de Matière et Applications aux Procédés. PhD thesis, Institut National Polytechnique de Lorraine, Nancy, France, 2001.

[19] C. Amador, A. Gavriilidis, and P. Angeli. Flow distribution in different microreactor scale-out geometries and the effect or manufacturing tolerances and channel blockage. *Chem. Eng. J.*, 101:379–390, 2004.

[20] L. L. Raja, R. J. Kee, O. Deutschmann, J. Warnatz, and L. D. Schmidt. A critical evaluation of Navier–Stokes, boundary-layer, and plug-flow models of the flow and chemistry in a catalytic-combustion catalyst. *Catal. Today*, 59:47–60, 2000.

[21] G. F. Froment and K. B. Bischoff. *Chemical reactor analysis and design*. Wiley, Chichester, USA, 2nd edition, 1990.

[22] V. Cominos, V. Hessel, C. Hofmann, G. Kolb, H. Löwe, R. Zapf, E. R. Delsman, M. H. J. M. de Croon, and J. C. Schouten. Fuel processing in micro-reactors for low power fuel cell applications. In *Proc. of the 27th Int. Exhibition-Congress on Chemical Engineering, Environmental Protection and Biotechnology (ACHEMA 2003)*, page 9. Frankfurt, Germany, 2003.

[23] M. J. Kahlich, H. A. Gasteiger, and R. J. Behm. Kinetics of the selective CO oxidation in H_2-rich gas on Pt/Al_2O_3. *J. Catal.*, 171:93–105, 1997.

Comparison between conventional fixed-bed and microreactor technology

7

This chapter is submitted for publication as:

E.R. Delsman, B.J.P.F. Laarhoven, M.H.J.M. de Croon, G.J. Kramer, and J.C. Schouten. Comparison between conventional fixed-bed and microreactor technology. *Chem. Eng. Res. Des.*, submitted.

Abstract

Advances in microreactor technology have made production of chemicals in microstructured reactors possible. The question now rises whether microreactors can compete with or replace current conventional reactors in production processes. In order to answer this question, a comparative study is performed between microreactor technology and conventional reactor technology for the case of methanol fuel processing for portable power generation. The study is limited to the chemical reactor devices of the fuel processor: a reformer–burner (RefBurn) reactor, with coupling of endo- and exothermal reactions, and a preferential oxidation reactor with integrated heat exchangers (ProxHeatex device), which shows integration of reaction and heat exchange. Detailed system designs are made for 100 W_e and 5 kW_e power output, which are evaluated on four comparison criteria: system volume, insulation volume, system weight, and required catalyst mass. Fixed criteria are used for reactor conversion, maximum reactor temperature, and pressure drop. On both levels of power output, the RefBurn and ProxHeatex microstructured devices outperform the conventional systems, resulting in smaller and lighter reactor devices.

7.1 Introduction

Microreactors are miniaturized chemical reaction systems, which contain parallel reaction channels with a typical diameter of 10–500 µm. A solid catalyst may be present as a coating on the channel walls. The small channel dimensions of microreactors result in an increased surface area-to-volume ratio and increased driving forces for heat and mass transport [1–3]. Microreactors thus provide a benefit when the reaction rate in conventional reactors is limited either by mass transport to the catalyst or through an interface, or by heat transport to or from the reaction zone. When no heat and mass transport limitations are present, microreactors may not be the best choice, since in that case reaction or catalyst volume is important, which is generally smaller in microreactors than in conventional reactors. Another benefit of microreactors is the ability to safely carry out reactions in the explosive regime, which can open up new reaction pathways or can avoid the use of large dilution streams [4]. Finally, microreactors offer the possibility to replace large batch vessels filled with possibly dangerous chemicals by small continuous flow reactors, also allowing for on-site and on-demand production [5]. However, small reactors do not necessarily need to be microstructured unless additional benefits are offered.

As microreactors are becoming of interest to industry, the question rises whether microreactors can actually compete with conventional production processes. We attempt to address this question by presenting a comparative case study between conventional fixed-bed reactor technology and microreactor technology. Instead of making a comparison on general terms, as was demonstrated by Commenge [6] to be very educational with respect to the potential capabilities of microreactors, the comparison in this paper is limited to a selected case. Although this limits the validity of the results, it does enable us to go into more detail and make a fairer and more thorough comparison. The selected case is derived from the European Union funded project MiRTH-e [7]. Within this project a portable microstructured fuel processor is developed to convert methanol into fuel cell grade hydrogen to fuel a 100 W_e proton exchange membrane fuel cell. The combination of fuel container, fuel processor, and fuel cell provides an alternative power source, for example, to replace battery packs in portable electronic equipment.

The methanol fuel processor consists of three units: a fuel vaporizer, a

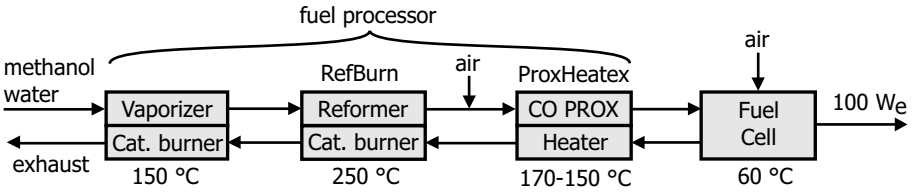

Figure 7.1: Schematic drawing of the MiRTH-e fuel processor–fuel cell system [7]. The system consists of a vaporizing unit, a reformer–burner (RefBurn) device, a preferential oxidation device with integrated heat exchangers (ProxHeatex), and a proton exchange membrane fuel cell.

reformer–burner (RefBurn) device, and a preferential oxidation reactor–heat exchanger (ProxHeatex) device, see Figure 7.1. In the fuel vaporizer, a liquid methanol–water mixture is vaporized before it enters the RefBurn device, where methanol and steam react to form carbon dioxide and hydrogen. The hydrogen-rich reformate gas contains approximately 0.5% carbon monoxide, which should be removed down to 10 ppm to prevent poisoning of the fuel cell anode catalyst. Therefore, in the ProxHeatex device, carbon monoxide is oxidized with a small quantity of air. The clean hydrogen-rich gas is fed to the fuel cell to generate electricity. The fuel cell exhaust stream still contains about 5% of hydrogen and is fed back into the system to recover heat from the exothermic carbon monoxide oxidation and to generate the heat required for the endothermic methanol–steam reforming reaction and the fuel vaporization.

We limit this comparative study to the catalytic reactor devices, viz. the RefBurn and ProxHeatex devices. Next to the 100 W_e scale for portable electronics, the same exercise is repeated on the 5 kW_e scale to observe whether the comparison of the two reactor technologies is scale dependent. A power output of 5 kW_e is a typical power output of auxiliary power units, which are used for automotive and domestic power applications. A description of the RefBurn and ProxHeatex devices will be given in the next section, together with the design objectives and constrains. Thereafter, the strategy used for comparing the two technologies will be presented. Next, a detailed description is given of the used design strategies for the conventional and microreactor technology designs. In total eight reactor designs are made for two devices (RefBurn and ProxHeatex), with two technologies (microreactor and fixed-bed reactor technologies), and on two scales (100 W_e and 5 kW_e). Finally, the sys-

Table 7.1: Reactions involved in methanol fuel processing.

Methanol steam reforming	$CH_3OH + H_2O \rightarrow CO_2 + 3H_2$	$\Delta H = +49\ \frac{kJ}{mol}$	(7.1)
Methanol decomposition	$CH_3OH \rightarrow CO + 2H_2$	$\Delta H = +90\ \frac{kJ}{mol}$	(7.2)
Water gas shift	$CO + H_2O \rightleftarrows CO_2 + H_2$	$\Delta H = -41\ \frac{kJ}{mol}$	(7.3)
Carbon monoxide oxidation	$CO + \frac{1}{2}O_2 \rightarrow CO_2$	$\Delta H = -283\ \frac{kJ}{mol}$	(7.4)
Hydrogen burning	$H_2 + \frac{1}{2}O_2 \rightarrow H_2O$	$\Delta H = -242\ \frac{kJ}{mol}$	(7.5)

tem designs are compared to answer the question which reactor technology is most suitable for the production of fuel cell grade hydrogen from methanol on the scales considered.

7.2 Process description and design criteria

7.2.1 RefBurn device

In the RefBurn device, a methanol–steam reformer is coupled to a catalytic burner. In the methanol–steam reforming process, hydrogen and carbon dioxide are produced. The reformer feed consists of a methanol–water vapor (molar ratio 1:2), superheated to 150 °C. The reforming is carried out over the BASF K3–110 $Cu/ZnO/Al_2O_3$ catalyst [8] at 250 °C. This temperature is also used as the maximum temperature in the catalyst bed, since deactivation of the catalyst occurs at temperatures exceeding 250 °C. Three reactions play a role (reactions (7.1), (7.2), and (7.3) in Table 7.1), as described in detail by Peppley et al. [8, 9]. The heat required for the endothermal reforming reaction is provided by catalytically burning the excess hydrogen from the fuel cell at the burner side of the device over a $Pt/\gamma\text{-}Al_2O_3$ catalyst (reaction (7.5) in Table 7.1). Since hydrogen burning is much faster than the reforming reaction, distribution of the heat generated by the burner over the complete reactor is an issue in the design of the RefBurn device [10].

The design target for the RefBurn reactor is a required methanol conversion of 99%. Since methanol decomposition and water gas shift are slow compared to the reforming reaction, only the methanol–steam reforming reaction is included in the reactor design model. The actual methanol conversion rate

(R_{MeOH}) is described by a first order power law as

$$-R_{\mathrm{MeOH}} = \eta_{\mathrm{cat}}(d_{\mathrm{cat}}, T) \cdot 5.5 \cdot 10^{10} \cdot \mathrm{e}^{\frac{-90\mathrm{kJ/mol}}{RT}} \cdot C_{\mathrm{MeOH}} \quad \mathrm{mol\ m_{cat}^{-3}\ s^{-1}} \qquad (7.1)$$

where η_{cat} is the catalyst effectiveness factor, R the gas constant, T the reforming temperature, and C_{MeOH} the methanol concentration. The catalyst effectiveness factor is included in the calculations and is a function of the catalyst pellet diameter or catalyst coating thickness and the temperature of the catalyst. The density of the catalyst pellets is taken to be 2100 kg m^{-3} with an average pore diameter of 10 nm. Diffusion in the catalyst is described by Knudsen diffusion. A value of 0.4 is used for the porosity of the fixed-beds. No kinetic model is used to describe the heat production by the catalytic burner. Hydrogen is assumed to react instantaneously after entering the reactor. Since the required amount of burner catalyst is small compared to the amount of reformer catalyst, its influence on the reactor size and weight is neglected and its exact amount is not calculated.

7.2.2 ProxHeatex device

The reformate gas that enters the ProxHeatex device is assumed to contain carbon monoxide in a concentration of 0.5% and to be free of methanol. In the ProxHeatex device, the carbon monoxide concentration is reduced to 10 ppm, to prevent poisoning of the fuel cell anode catalyst, by oxidation with a small quantity of air. Both CO and hydrogen oxidation occur (reactions (7.4) and (7.5) in Table 7.1). A selective catalyst is used to reach the required CO conversion of 99.8% and to avoid excessive hydrogen oxidation. The preferential oxidation (Prox) catalyst considered in this paper is the Pt-Ru/α-Al_2O_3 catalyst, which has been developed at the Energy Research Center of the Netherlands [11]. The selectivity of the catalyst is close to 50%. The reactor temperature is controlled at a maximum temperature of 170 °C near the inlet and decreases to 140-155 °C towards the outlet by using the fuel cell exhaust gas to remove the produced reaction heat. In this way a high catalyst activity in the first part of the reactor is combined with increased selectivity in the second part. The rate of carbon monoxide oxidation is calculated using the rate equation from Kahlich et al. [12] with the kinetic parameters refitted to the data of de Wild et al. [11] for the Pt-Ru catalyst. For an equimolar feed of carbon monoxide and oxygen, and assuming a selectivity of oxygen towards carbon dioxide of

50%, the observed reaction rate is described by:

$$-R_{CO} = \eta_{cat}(d_{cat}, T, C_{CO}) \cdot 5 \cdot 10^{10} \cdot e^{\frac{-80 kJ/mol}{RT}} \cdot C_{CO}^{0.4} \quad \text{mol m}_{cat}^{-3}\,\text{s}^{-1} \tag{7.2}$$

with η_{cat} the catalyst effectiveness factor, which is in this case dependent on the diameter of the catalyst pellets or the catalyst coating, the temperature, and the carbon monoxide concentration. T is the reactor temperature and C_{CO} the carbon monoxide concentration. The density of the catalyst pellets is taken to be 2000 kg m^{-3} with an average pore size of 0.3 µm. Due to the large pore diameter, gas phase diffusion was used to describe the diffusion in this catalyst.

Next to the cooled preferential oxidation reactor, the ProxHeatex device also incorporates two heat exchangers: a high temperature heat exchanger to cool down the reformate gas from 250 °C to about 160 °C, and a low temperature heat exchanger to cool down the cleaned reformate gas from 150 °C to 60 °C (the operating temperature of the fuel cell). The heat exchangers provide for maximum heat recovery, which is important for a high fuel processing efficiency. The combined fuel cell anode and cathode exhaust stream is used as coolant, as is shown in Figure 7.1. The heat exchangers are designed to reach a temperature approach between the two gases at the cold end of the heat exchangers, of 5 and 1 °C for the high and low temperature heat exchanger, respectively. The complete coolant stream is used in the low temperature heat exchanger. Before entering the reactor and subsequently the high temperature heat exchanger, a part of the coolant stream is bypassed. The bypass fraction is adjusted during the calculations to control the maximum reactor temperature at 170 °C.

7.2.3 Flow rates

The inlet gas flow rates are based on the aspired electrical output, 100 W_e and 5 kW_e, and fuel efficiency, 35% based on the lower heating value of methanol, of the fuel processor–fuel cell system. The fuel cell efficiency is taken to be 50% with respect to converting hydrogen into electricity, which leads to an aspired efficiency of the fuel processor itself of 70%. These considerations lead to the list of flow rates and allowed heat losses, which is presented in Table 7.2. The gas phase properties and diffusion constants were estimated using the Aspen® property estimation routine [13]. Microtherm® is used as the insulat-

Table 7.2: Fixed design parameters for the RefBurn and ProxHeatex devices based on a 100 W_e fuel cell. Flow rates and heat losses for the 5 kW_e case are 50 times larger.

Design parameter	RefBurn	ProxHeatex
Process gas flow rate (g s^{-1})	0.027	0.030
Burner gas flow rate (g s^{-1})	0.15	0.15
Maximum temperature (°C)	250	170
Required conversion (%)	99	99.8
Operating pressure (bar)	1	1
Pressure drop reactors (kPa)	5	5
Pressure drop heat exchangers (kPa)		2.5
Heat loss (W)	5	5

ing material for all devices, which has a heat conductivity of 0.025 W m^{-2} K^{-1} and a density of 400 kg m^{-3}.

7.3 Comparison strategy

The comparison between microreactor and conventional technology will be based on the RefBurn and ProxHeatex devices of the MiRTH-e fuel processor. In the RefBurn device an endothermal and an exothermal reaction are coupled, as is shown in Figure 7.2. The ProxHeatex unit consists of one reactor where an exothermal reaction is cooled by a gas, and two gas-to-gas heat exchangers. Before making a comparison between conventional and microreactor technologies for these systems, the two technologies need to be defined. Tubular fixed bed reactors are used for both conventional reactors, since they provide integration of reaction and heat transfer, they are feasible on a small scale, and design equations for them are widely available. The two conventional heat exchangers are designed as compact plate-fin heat exchangers (CPFHXs), which are the first choice for gas-to-gas heat exchange. A microreactor system is defined in this paper as a system constructed as a stack of microstructured metal plates, which are shown in Figure 7.3. The catalysts are applied as a coating on the channel walls. The microstructured RefBurn device consists of an alternating stack of reformer and burner plates. The microstructured ProxHeatex device integrates the cooled preferential oxidation

reactor and the two heat exchangers in a single stack of plates, as is shown in Figure 7.4.

The comparison for the RefBurn and Prox reactors is aimed at showing how differences in construction and in heat and mass transfer characteristics of the two reactor technologies influence the required size and weight of the reactors. In the comparison, reactor conversion, maximum temperature in the reactor, pressure, pressure drop, and heat loss are kept equal for the conventional and microstructured systems, see Table 7.2. In this case, the heat transfer characteristics will determine the temperature gradient in the reactor and thus the average catalyst temperature. This directly affects the amount of catalyst needed to obtain the required conversion. The required amount of catalyst is also influenced by mass transfer limitations in the catalyst pellets or coatings. Differences in mass and volume of the final systems are also expected to result from differences in the construction of the devices. Construction parameters for the conventional reactors are the thickness of the tube and shell walls, tube pitch, and the size of flow headers. For the microsystem, the thickness of the plates and the fins between the channels, and the size of the flow distribution chambers are important.

The design of both systems is based on dedicated reactor modelling and on fixed design standards, as described in the Heat Exchanger Design Handbook [14] for a conventional shell-and-tube heat exchanger and in our earlier paper [15] for a microstructured reactor. The influence of the non-uniform axial and radial temperature distribution in the fixed-bed reactors is assessed using a two-dimensional pseudo-homogeneous model [16]. Dedicated models, developed at our laboratory [15, 17], are used to design the microreactor systems. Mass transfer resistances are expected in the form of internal diffusion limitations in the catalyst pellets and coated layers. The influence of internal diffusion limitations is included in these models through incorporation of a catalyst effectiveness factor, as shown above in equations (7.1) and (7.2). The assumption is made that the coated catalysts are identical in activity, density, and pore size to the material in the catalyst pellets.

The conventional CPFHXs are designed based on the information provided in the Heat Exchanger Design Handbook [18]. The microstructured heat exchangers are designed using the method outlined in our earlier paper [15]. Since CPFHXs and microstructured heat exchangers are similar in construction and channel sizes, similar results are expected from the compar-

ison. However, the microsystem design has the advantageous possibility of straight-forward integration of the heat exchangers with the preferential oxidation reactor in a single stack of plates, leading to a decrease in required insulation volume. Both conventional and microstructured heat exchangers are designed using a one-dimensional heat transfer model, which includes external heat losses and longitudinal conduction of heat through the heat exchanger material. This is necessary due to the small size of the heat exchangers. The exact operating conditions of the heat exchangers differ slightly between the cases, caused by differences in outlet gas temperatures of the preferential oxidation reactor and required fraction of coolant flow. Furthermore, the microsystem calculations include, next to heat losses to the environment, also heat transfer to the adjacent preferential oxidation reactor. The design target is a required temperature approach between the gases at the cold end of the heat exchangers, which is kept equal for conventional and microstructured systems.

The specification of the comparison criteria is guided by the intended application of the fuel processor systems. In order to compete with battery packs for portable electronics and auxiliary power generation, the system should fulfill certain technical and economical requirements. For example, compactness and low weight are more important for a portable fuel processor than in the design of a large chemical plant. Therefore, the designs will be compared on system and insulation volume, required amount of catalyst, and total weight. A list of comparison criteria is shown, next to the design criteria, in Table 7.3. The table also contains a number of criteria, which are not evaluated in this study, like the production costs, transient behavior, and ease of operation. Although these criteria will also be important in a decision between these technologies for this application, no reliable information is available to assess them quantitatively.

All designs are made for 100 W_e and 5 kW_e power output, corresponding to the requirements for portable electronic equipment and auxiliary power units, respectively. This offers the possibility to get information on the scale dependence of the technology comparison. Therefore, scaling factors are calculated based on the calculated system volumes and weights. The scaling factor (β) for the system volume is defined by:

$$\beta \cdot \ln \frac{5\ \mathrm{kW}}{100\ \mathrm{W}} = \ln \frac{V(5\ \mathrm{kW})}{V(100\ \mathrm{W})} \tag{7.3}$$

Table 7.3: Comparison criteria MiRTH-e fuel processing case.

Used as design variable	*Evaluated*	*Not evaluated*
Reactor conversion	System volume	Mass production costs
Temperature approach	Insulation volume	Fouling
Operating temperature	System weight	System life time
Operating pressure	Catalyst mass	Ease of operation
Pressure drop		Transient behavior
Heat loss		Sensitivity for fluctuations

with V the calculated system volume for the indicated power output. Similarly, a second scaling factor is calculated based on the system weights.

7.4 Conventional system design

7.4.1 Design principles

The conventional system is designed according to the lay-out shown in Figure 7.2. It is divided into two parts comparable to the two microdevices explained in the subsequent section. The system designs are equal for both 100 W_e and 5 kW_e scale. Both reactors are designed as tubular fixed-bed reactors. In the RefBurn reactor, the reformer catalyst bed is positioned on the shell side and the burner catalyst is coated on the inside of the tubes. At the burner side a coated catalyst is used to avoid excessive hot-spot formation on the burner side. Consequently, the comparison will mainly be focussed on the reformer side. In the Prox reactor, the preferential oxidation catalyst is placed in the tubes. Low-height fins are used on the outside of the tubes to increase heat transfer to the coolant gas flowing on the shell side. Aluminium is chosen as construction material for the Prox reactor, due to its high thermal conductivity and low density. Carbon steel is chosen for the RefBurn reactor, since aluminium is not suitable for temperatures above 250 °C.

The two heat exchangers are designed as compact plate-fin heat exchangers (CPFHXs), which are well-suited for gas-to-gas applications. CPFHXs consist of thin plates, which have fins or spacers sandwiched between them to increase the heat transfer surface and to give structural support to the plates. The heat exchangers are made of stainless steel, since longitudinal heat con-

duction is reduced by the low thermal conductivity of stainless steel.

The reactors are designed according to the design strategy and correlations for a shell-and-tube heat exchanger [14]. For the fixed-bed regions of the reactors, i.e. the shell side for the RefBurn reactor and the tube side for the Prox reactor, heat transfer parameters are calculated using the correlations from Yagi et al. [19, 20]. The temperature and conversion profiles in the fixed-beds are calculated numerically with a two-dimensional pseudo-homogeneous model [16], in which heat and mass transfer are accounted for in both axial and radial directions. Axial heat conduction by the reactor tubes and external heat loss, which are both considerable on the reactor scales considered, are also included in the models. The model equations are shown in Table 7.4, where equations (7.4) and (7.5) are the energy and mass balances for the fixed-bed, and equations (7.6) and (7.7) describe heat transfer in the tubes, and the burner or coolant gas, respectively. The reaction rates are described by the power-law rate equations (7.1) and (7.2). Internal catalyst diffusion limitations are accounted for by calculating the catalyst effectiveness factor as a function of the reactor position. The calculations are performed using the Femlab® [21] finite element solver. The volumes of the reactors are minimized using the fixed criteria for pressure drop, conversion, and the maximum catalyst temperature (Table 7.2). Finally, the required volume of insulating material is calculated, based on the allowed heat loss.

The design of the CPFHXs is also based on a minimization of the system volume. A combination of plate length, width, and distance is chosen, as well as the number of passes for both heat exchange fluids, to comply to the targets for pressure drop and heat exchange efficiency. The latter is also influenced by longitudinal heat conduction in the plates and fins. A plate thickness of 0.1 mm is chosen, which provides sufficient mechanical strength for an operating pressure of 1.5 bar [22]. The heat exchange efficiency of the CPFHXs is calculated with a one-dimensional model for conventional heat exchangers, in which the temperature is calculated along the exchanger length. The model is extended by including axial heat conduction in the metal plates and external heat losses, which are both important in small-scale heat exchangers. The model equations are of a form equal to equations (7.6) and (7.7) in Table 7.4. The Heat Exchanger Design Handbook [18] is used to obtain reasonable sizings and heat transfer parameters.

Table 7.4: Model equations for the conventional fixed-bed reactors; $\underline{k}_e$: effective bed conductivity, T: temperature, c_p: heat capacity, $\underline{G}$: mass flux, ΔH: reaction enthalpy, R_V: volumetric reaction rate, ρ_r: gas density, $\underline{D}$: diffusivity, ω, M: mass fraction and molar weight of the reacting species, V_t: tube volume, κ_t: tube heat conductivity, z: axial coordinate, UA: heat transfer coefficient multiplied by heat transfer surface. The subscripts denote (b) the catalyst bed, (r) the reformate gas, (t) the tube wall, (bc) the burner or coolant gas, and (ex) the external environment.

Bed temperature	$\nabla \cdot (-\underline{k}_e \nabla T_b) + c_p \underline{G}_r \cdot \nabla T_b = \Delta H \cdot R_V$	(7.4)
Bed conversion	$\nabla \cdot (-\rho_r \underline{D} \nabla \omega) + \underline{G}_r \cdot \nabla \omega = M \cdot R_V$	(7.5)
Tube temperature	$-V_t \kappa_t \frac{d^2 T_t}{dz^2} = UA_b(T_b - T_t) - UA_{bc}(T_t - T_{bc}) - UA_{ex}(T_t - T_{ex})$	(7.6)
Burner/coolant gas temperature	$c_p G_{bc} \frac{dT_{bc}}{dz} = UA_{bc}(T_t - T_{bc})$	(7.7)

7.4.2 Conventional RefBurn reactor

The conventional reformer–burner reactor is designed as a tubular fixed-bed reactor with the methanol reforming catalyst packed at the shell side and the hydrogen burning catalyst applied as a coating on the inside surface of the tubes. The burner catalyst is put on the inside of the tubes to facilitate an equal distribution of the burner gas to all tubes and to establish a homogeneous heating of the reformer catalyst bed. The burner catalyst is applied as a coating to the tube wall to ensure good heat transfer to the tubes and to avoid hot spots on the burner side of the reactor. Consequently, the reformer catalyst is packed in the shell side of the heat exchanger. The catalyst bed does not fill the complete shell, as shown in Figure 7.2, to allow for equal distribution of the reformer feed gas over the catalyst bed. The required header space at the inlets and outlets of the reformer and burner gases is set at 25% of the shell diameter, leading to a total additional length of the reactor equal to one shell diameter.

The used design procedure is as follows:

1. Tube diameter and pitch are chosen as well as the amount of catalyst and

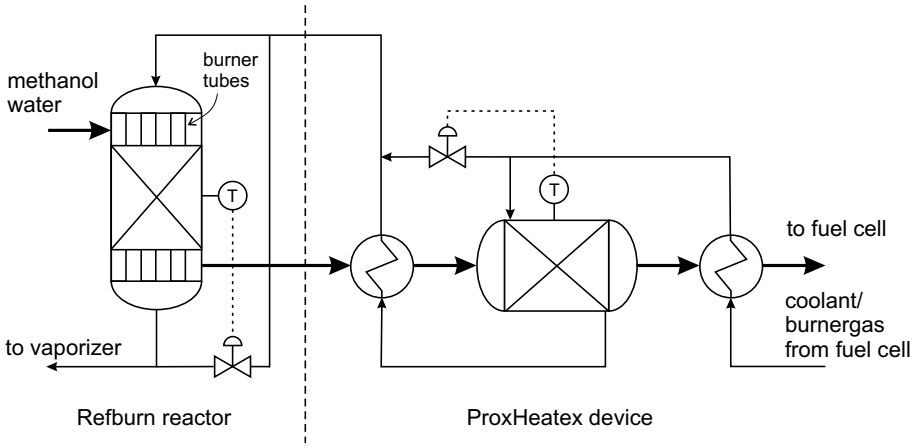

Figure 7.2: Schematic drawing of the conventional system design. The RefBurn reactor consist of a packed bed of reformer catalyst through which tubes run, which are coated on the inside with a burner catalyst. In the Prox reactor the catalyst is packed inside the tubes, where the outside of the tubes contain low-height fins to promote heat transfer to the coolant gas.

its pellet diameter. A triangular tube configuration is used. The tube pitch is chosen large enough to allow at least eight catalyst particles on the hydrodynamic diameter of an empty shell cross-section.

2. The bed length and the resulting shell diameter and number of burner tubes are determined from the allowed pressure drop on the reformer side. The burner side pressure drop is much lower than the allowed pressure drop in all cases.
3. The total reactor volume is then calculated by including inlet and outlet flow distribution headers.
4. Heat and mass transfer parameters are calculated as input for the numerical reactor model using correlations from Taborek [14], Froment and Bischoff [16], and Yagi and Kunii [20].
5. The required burner gas flow rate and reactor temperature and conversion are calculated using two coupled models for the catalyst bed and the burner tubes. As a simplification only a single tube is modelled. The shell-side catalyst bed is modelled using a two-dimensional model of an annular packed bed around a single burner tube. The longitudinal temperature profile in the burner tubes and the heat transfer to the burner gas is described by a one-dimensional model.

Table 7.5: Specifications of the conventional RefBurn and preferential oxidation (Prox) reactor designs.

Design parameter	RefBurn reactor		Prox reactor	
	100 W_e	5 kW_e	100 W_e	5 kW_e
Construction material	steel	steel	aluminium	aluminium
Pellet diameter (mm)	0.4	1.0	0.4	1.3
Tube diameter[a] (mm)	2 (0.5)	2 (0.5)	8 (0.5)	12 (0.7)
Tube pitch (-)	2	2.5	1.25	1.25
Fixed-bed length (cm)	5.2	19	2.2	7.5
Number of tubes	56	974	4	35
Shell diameter[a] (cm)	2.8 (3)	15 (4)	3.2 (3)	11 (4)
Reactor volume (dm^3)	0.091	7.0	0.061	1.7
Insulation volume (dm^3)	0.28	1.1	0.10	0.11
Catalyst mass (g)	30	3500	4.1	280
Total mass (kg)	0.53	17	0.084	1.5
Mean bed temperature (°C)	235	222	155	151
Mean cat. effectiveness (%)	79	57	98	83

[a]Internal diameter, value between brackets is the wall thickness

6. The calculated methanol conversion and maximum reactor temperature are compared to their respective design criteria and the steps are repeated to find the design that meets the design criteria and has the smallest system volume.

The resulting design specifications of the conventional RefBurn reactors are shown in Table 7.5.

7.4.3 Conventional ProxHeatex device

The conventional ProxHeatex device (Figure 7.2) consists of three separate units: a fixed-bed reactor and two CPFHXs. The reactor itself is a tubular fixed-bed reactor with the catalyst packed inside the tubes to ensure equal residence time of the reformate gas and optimal heat removal from the catalyst bed. The outside of the tubes is cooled by preheating the burner gas, which flows at the shell side. The shell-side heat transfer is increased by using low-height fins on the outer surface of the tubes and by using baffles in

the shell. The fins used are 1 mm high, 0.2 mm wide, and are spaced 0.8 mm apart. In this configuration, the heat transfer resistance on the inside and outside surfaces of the tubes are of comparable magnitude. Aluminium is chosen as construction material to increase temperature uniformity and to reduce the reactor weight. The full coolant flow is used in the low-temperature heat exchanger, while in the reactor and high-temperature heat exchanger a fraction of the coolant flow is used to control the reactor temperature.

The following procedure is used for the reactor volume minimization:

1. Values are chosen for the catalyst mass and its pellet diameter, and the tube diameter, allowing at least eight catalyst particles within the tube diameter.
2. The allowed pressure drop in the tubes determines the tube length and the number of tubes. The shell-side pressure drop is much lower than the criterion of 5 kPa for both power output scales (Table 7.2).
3. The shell diameter is calculated based on a triangular tube configuration with a tube pitch of 1.25. A rectangular tube configuration is used for the 100 W_e case. The total length of the reactor is calculated by adding flow headers with a length of one-third of the shell diameter.
4. Heat and mass transfer coefficients are calculated based on the reactor geometry using correlations from Taborek [14], Froment and Bischoff [16], and Yagi and Kunii [20].
5. The carbon monoxide conversion, the temperature distribution in the reactor, and the required coolant gas flow rate are calculated using numerical simulations. The packed bed is modelled with a cylindrical two-dimensional model of a single reactor tube. The temperature of the tube wall and the coolant gas are calculated using a separate one-dimensional model. Both models are solved simultaneously.
6. New values are chosen in step 1 to satisfy the temperature and conversion criteria and minimizing the reactor volume.

The detailed specifications of the reactor designs are shown in Table 7.5.

The two compact heat exchangers are designed using stainless steel as construction material, since on these small scales axial heat transport is an important factor. The low thermal conductivity of stainless steel reduces its adverse effect. The design procedure of the CPFHXs is:

1. The number of plates for both sides and the width and length of the plates are chosen. A fixed plate and fin thickness of 0.1 mm, and a fin spacing of 10 fins/cm are used, providing sufficient mechanical strength.

Table 7.6: Specifications of the CPFHX designs of the conventional ProxHeatex device.

Design parameter	100 W_e				5 kW_e			
	HT HEx[a]		LT HEx		HT HEx		LT HEx	
	ref	cool	ref	cool	ref	cool	ref	cool
Number of passes	5	12	6	12	16	39	8	15
Plate spacing (mm)	0.29	0.20	0.16	0.23	0.53	0.40	0.9	1.4
Width & Height (mm)	5.6		5.7		30		30	
Length (mm)	61		22		60		65	
Unit volume (cm^3)	2.8		1.3		71		130	
Insulation volume (cm^3)	30		8		10		16	
Total mass (g)	13		4.5		130		130	

[a]HT HEx = high temperature heat exchanger, LT HEx = low temperature heat exchanger, ref = reformate side, cool = coolant side

2. The plate spacings are then determined by the allowed pressure drop.
3. Heat transfer coefficients and the amount of axial heat conduction are calculated and used in a one-dimensional counter-current heat exchanger model to calculate the outlet temperatures of the heat exchanger.
4. The heat exchanger volume is calculated by including flow headers with a total length of half the plate width.
5. The input values are adjusted to comply to the outlet temperature criteria for a minimal heat exchanger volume.

The detailed specifications of the resulting CPFHXs designs are shown in Table 7.6.

7.5 Microreactor system design

7.5.1 Design principles

The microreactor systems are constructed from stacks of thin plates. In these plates microstructures, are made to form flow distribution chambers and the microchannels. Heat exchangers are created by alternated stacking of two mirror images of the plates as is shown in Figure 7.3. A solid catalyst is incorporated by applying it as a coating onto the channel walls. In this way the

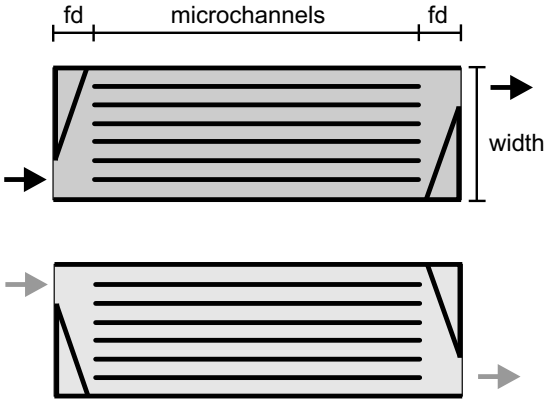

Figure 7.3: Schematic drawing of the microstructured plates. Plates contain flow distribution chambers (fd) and microchannels. Alternating stacking of the mirror images of the microstructured plates creates a heat exchanger.

pressure drop is kept low and effective heat transfer can take place between the catalyst and the metal wall. After stacking, the plates are joint together using laser welding or diffusion bonding. A proper design of the flow distribution chambers, and using a ratio of channel length over plate width larger than two, ensure that the flow is equally distributed over the individual microchannels [23]. In all microreactor designs, the length of the flow distribution areas and the diameter of the inlet and outlet tubes are set at one-third of the width of the plate. The external surface area is minimized by dividing the channels over a number of plates in such a way as to make the width of the plates equal to the resulting stack height. When the plate width becomes larger than half of the channel length (required for an even flow distribution), the reactor is divided into a number of identical reactors, which are placed side-by-side to minimize the external surface area.

The iterative design procedure of the microdevices consists of four steps, leading to a design that fulfils the design criteria with a minimum system volume:

1. A channel width, an amount of catalyst, and a coating thickness are chosen.
2. The number of channels and the channel height and length are calculated to incorporate all the catalyst and to comply to the pressure drop criteria for both gasses. The plate thickness is calculated based on a calculation of the maximum material stresses [22]. The total length of the plates is calculated by adding additional length for the flow distribution chambers.
3. Heat and mass transfer parameters are calculated based on the reactor geometry, which serve as input for the numerical reactor models.
4. The temperature profile in the reactors and heat exchangers and the conver-

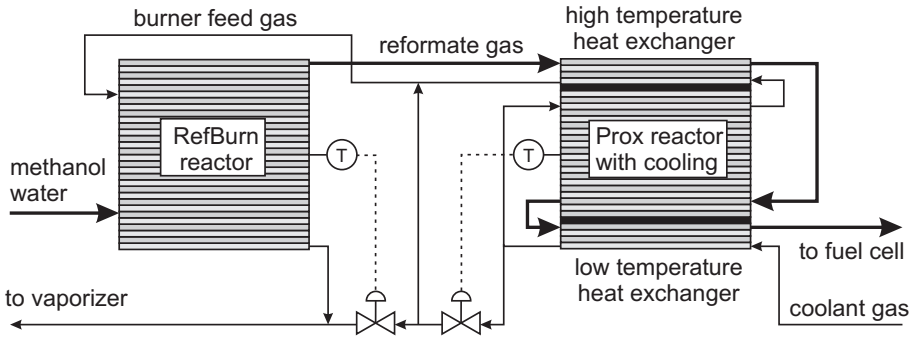

Figure 7.4: Lay-out of the microstructured RefBurn and ProxHeatex devices. The microdevices consist of two types of alternatingly stacked plates. The ProxHeatex device integrates a cooled reactor and two heat exchangers.

sion of the reactors is calculated by dedicated microreactor models. Based on the results, new values are chosen in step 1.

The heat transfer simulations for the microsystem designs are performed using Femlab [21]. The two-dimensional model developed by Delsman et al. [17], is used to calculate the temperature profile and the reaction conversions for the RefBurn device. In this model, the fluid and metal temperatures are assumed to be uniform in the direction perpendicular to the microstructured plates. The ProxHeatex device is designed using a model consisting of three coupled one-dimensional sub-models [15]. This model calculates the longitudinal temperature profiles of the Prox reactor and heat exchangers and the reactor conversion simultaneously. The microreactor model equations contain similar contributions as the equations for the conventional reactors listed in Table 7.4. The reaction conversions are calculated using the power-law rate equations (7.1) and (7.2). Diffusion limitations inside the catalyst coating are accounted for by calculating the catalyst effectiveness factor as a function of reactor position.

7.5.2 RefBurn microreactor

Carbon steel reformer and burner plates are used for the RefBurn microreactor, see Figure 7.4. The plate geometry of the reformer and burner plates is identical, only differing in channel cross-section and the number of channels. Twice as many reformer plates are used as burner plates. The optimal

Table 7.7: Specifications of the reformer–burner microreactor designs.

Design parameter	100 W_e		5 kW_e	
	ref[a]	burn[a]	ref	burn
Number of plates	96	48	348	174
Units in parallel	4	4	4	4
Channels per plate	30	30	143	143
Open channel height (µm)	40	70	91	160
Channel length (cm)	2.3	2.3	12	12
Coating thickness (µm)	100	–	100	–
Reactor material	carbon steel		carbon steel	
Reactor size (w×h×l cm^3)	3.5×3.5×3.5		16×16×16	
Reactor volume (dm^3)	0.043		4.3	
Insulation volume (dm^3)	0.098		0.56	
Catalyst mass (g)	19		1700	
Total mass (kg)	0.21		12	
Mean bed temperature (°C)	247		228	
Mean cat. effectiveness (%)	75		86	

[a] ref = reformate side, burn = burner side

designs, which comply to the design criteria and have a minimum system volume, are found using the procedure described in the previous subsection. A two-dimensional reactor model is used to calculate the temperature distribution on the microstructured plates. Characteristics of the resulting reactor designs are shown in Table 7.7.

7.5.3 ProxHeatex microdevice

The ProxHeatex microdevice, like its conventional counterpart, consists of two heat exchangers and a cooled reactor. However, in the microdevice the reactor and the heat exchangers are stacked on top of each other separated by a layer of insulation material, see Figure 7.4. The width of all plates is kept equal to be able to integrate the individual parts in a single stack. The reactor section contains aluminium plates to increase the temperature uniformity. The heat exchangers contain stainless steel plates, in this case to reduce the axial conduction through the plate material. The reactor part contains twice

Table 7.8: Specifications of the preferential oxidation microreactor designs.

Design parameter	100 W_e		5 kW_e	
	ref[a]	cool[a]	ref	cool
Reactor material	aluminium		aluminium	
Number of plates	6	3	64	32
Units in parallel	1	1	3	3
Channels per plate	12	12	67	67
Open channel height (µm)	120	210	110	240
Channel length (cm)	5.0	5.0	5.0	5.0
Coating thickness (µm)	200	–	200	–
Reactor size (w×h×l cm^3)	1.5×0.5×7.1		7.7×5.0×8.7	
Reactor volume (dm^3)	0.005		0.34	
Insulation volume (dm^3)	0.026[b]		0.026[b]	
Catalyst mass (g)	3.2		170	
Total mass (kg)	0.020		0.60	
Mean bed temperature (°C)	158		156	
Mean cat. effectiveness (%)	82		83	

[a] ref = reformate side, cool = coolant side

[b] This figure represents the insulation volume of the complete ProxHeatex device including the heat exchangers.

as many reformate side as coolant side plates. A one-dimensional model is used for the design, which can calculate the temperature distribution in all device parts simultaneously. This is needed to correctly account for the heat exchange between the device parts through the separating insulation layers. Specifications are shown in Table 7.8 for the reactor designs and in Table 7.9 for the heat exchanger designs.

7.6 Comparison system designs

Figures 7.5 and 7.6 show the calculated system and insulation volumes, the required amounts of catalyst, and the overall system weights for the conventional and microstructured RefBurn and ProxHeatex devices for the 100 W_e and 5 kW_e cases, respectively. The details of the designs are presented in Tables 7.5–7.9. The results show that the microreactor designs are smaller and

Table 7.9: Specifications of the heat exchanger designs of the ProxHeatex microdevices.

Design parameter	100 W_e				5 kW_e			
	HTEX		LTEX		HTEX		LTEX	
	ref[a]	cool[a]	ref	cool	ref	cool	ref	cool
Number of plates	1	2	1	3	5	10	8	22
Inlets per plate	1	1	1	1	3	3	3	3
Channels per plate	12	12	12	12	67	67	67	67
Channel height (mm)	0.32	0.43	0.31	0.36	0.51	0.71	0.36	0.45
Channel length (mm)	30	30	50	50	63	63	63	63
Unit size (w×h×l mm^3)	15×1.4×41		15×1.7×61		77×11×82		77×15×82	
Unit volume (cm^3)	0.87		1.5		67		91	
Unit mass (g)	2.4		4.3		110		170	

[a] ref = reformate side, cool = coolant side

lighter than the conventional designs on both scales studied, although the relative difference becomes smaller at the larger scale. This is also shown by the calculated scaling factors (equation 7.3), which are listed in Table 7.10. The scaling factors are larger for the microreactor systems than for the conventional systems, which means that the system volume and weight increase faster for the microsystems than for the conventional systems, when the power output scale is increased. On the 100 W_e scale, the required insulation volume is relatively large: more than two times the system volume. On this scale, the specific external surface area of the devices becomes large, which makes external heat loss an important factor. On the 5 kW_e scale, external heat losses are already much less important, with the insulation volume being only one-tenth of the system volume.

7.6.1 The RefBurn device

The required amount of reformer catalyst is determined by the average temperature of the catalyst and the catalyst effectiveness. Both parameters are included in Tables 7.5, 7.7, and 7.8. Since a design constraint is put on the maximum temperature in the reactor, the average reactor temperature and thus the required amount of catalyst is determined by the heat transfer properties of the reactor. In both conventional and microreactor designs, all the burner heat is produced at the beginning of the catalyst bed. In both cases, this heat needs to be distributed over the complete length of the reactor by convection of the

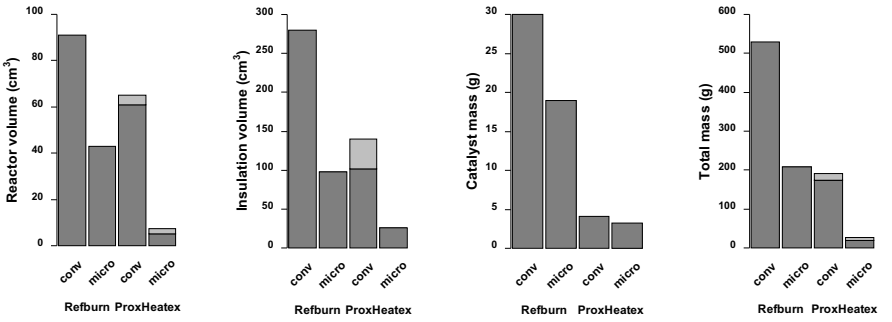

Figure 7.5: Design results for the quantified comparison criteria for a power output of 100 W_e for the conventional (conv) and microreactor (micro) designs. Light gray parts in the ProxHeatex graphs indicate the fraction related to the two heat exchangers.

gases and by longitudinal heat conduction through the reactor tubes or the microstructured plates. The difference between the two technologies is that an additional heat transfer resistance is present in the fixed-bed reactors in the form of a radial heat transport resistance, leading to a lower average catalyst temperature for the conventional reactors as compared to the microreactors.

The catalyst effectiveness is related to the catalyst pellet diameter for the conventional reactors and to the catalyst coating thickness for the microreactors. For a fixed-bed reactor, the catalyst pellet diameter has a strong influence on the bed pressure drop. This means that on a larger scale, when the bed length increases, a larger pellet diameter is required to comply to the pressure drop criterion. However, an increased pellet diameter increases the mass transfer resistance in the pellet, leading to a reduced catalyst effectiveness, and consequently to an increased amount of required reformer catalyst. In a microreactor system, the catalyst coating thickness and pressure drop are unrelated, which leads to a scale independent catalyst coating thickness. The results show that, for the 100 W_e RefBurn reactor, the catalyst effectiveness factor is comparable for both technologies, since the pellet diameter is small for the fixed-bed design on this scale. On the 5 kW_e scale, the pellet diameter in the conventional system is larger, leading to a lower catalyst effectiveness. The catalyst effectiveness increases for the microreactor with increasing scale, although the coating thickness remains constant, due to the lower reaction

Table 7.10: Scaling factors for the conventional (conv) and microreactor (micro) systems based on the 100 W_e and 5 kW_e designs. The system volume does not include insulation, the system weight does.

	RefBurn device		Prox reactor		Heat exchangers	
	conv	micro	conv	micro	conv	micro
system volume	1.1	1.2	0.9	1.1	1.0	1.1
system weight	0.9	1.0	0.6	0.9	0.7	1.0

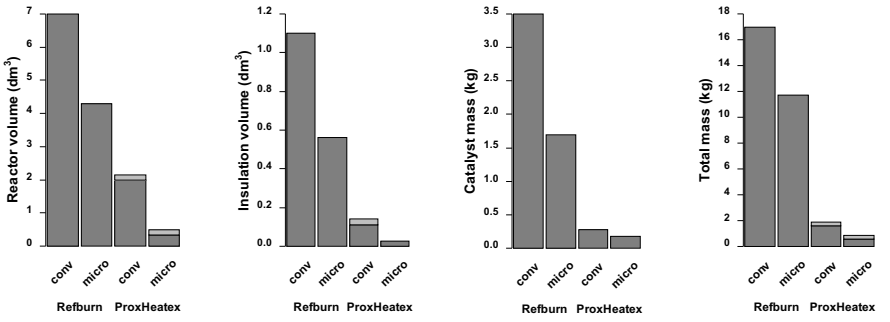

Figure 7.6: Design results for the quantified comparison criteria for a power output of 5 kW_e for the conventional (conv) and microreactor (micro) designs. Light gray parts in the ProxHeatex graphs indicate the fraction related to the two heat exchangers.

rate caused by the lower average catalyst temperature.

The total reactor volume is determined by the required amount of reformer catalyst and by the volume fraction of catalyst in the reactors. Apart from the catalyst, the conventional reactors contain tubes, a shell wall, and flow headers. For the microreactors, the metal plates, the flow channels, and the flow distribution chambers add to the reactor volume. The catalyst volume fraction is, on the two scales studied, 16 and 25% for the conventional reactors, and 22 and 20% for the microreactors, for the output scales studied. This shows that the conventional reactors become less efficient in storing catalyst on smaller scales, while the microreactors become more efficient. This is also indicated by the higher scaling factors of the microreactors compared to the conventional designs, which show that, going to a smaller scale, the size decrease is larger for the microreactors than for the conventional reactors. Although the differences between the two technologies are smaller on the 5 kW_e scale

than on the 100 W_e scale, the RefBurn microreactors are smaller and lighter than their conventional equivalents on both scales studied. On these scales, a smaller system volume also provides an additional advantage, since a smaller reactor requires less insulation material.

7.6.2 The ProxHeatex device

The required amount of catalyst for the preferential oxidation reactors, like for the RefBurn reactors, is determined by the average catalyst temperature and effectiveness. However, in the Prox reactor, a decreasing temperature profile is required as opposed to isothermal conditions in the RefBurn device. Therefore, heat does not have to be distributed completely over the length of the reactor, but heat has to be transferred to a coolant gas, which flows co-current for the conventional reactors and counter-current for the microreactors. The average catalyst temperatures of the micro Prox reactors are in this case comparable to those of the conventional reactors. Another difference with the RefBurn reactor is that the catalyst effectiveness is higher in the Prox reactors, due to the lower reaction rate and larger catalyst pores of the Prox catalyst. Consequently, the difference in the required amount of catalyst between the conventional and microreactor designs is smaller for the Prox reactors than it is for the RefBurn device.

However, the difference in reactor volume between the two technologies is larger for the Prox reactor than for the RefBurn reactor. This is caused by a large difference in the fraction of catalyst in the Prox reactors. The catalyst fraction in the reactor is higher for the Prox microreactors (30 and 25%) than for the RefBurn microreactors, due to the thicker catalyst coatings. The conventional Prox reactors, however, contain a very low volume fraction of catalyst: 3 and 8% for the 100 W_e and 5 kW_e designs, respectively. This is caused by the poor heat transfer to the coolant gas in the conventional reactors, which make the use of low-height fins on the tubes necessary. The use of these fins increases the reactor volume by about 50%. An additional factor for the 100 W_e conventional design is the need for only four catalyst tubes, which do not fit in a shell as efficiently as is possible for a large number of tubes.

Comparison of the individual heat exchangers of the ProxHeatex device is complicated by the differences in operating conditions, since the heat exchangers are separate in the conventional design, but integrated with the re-

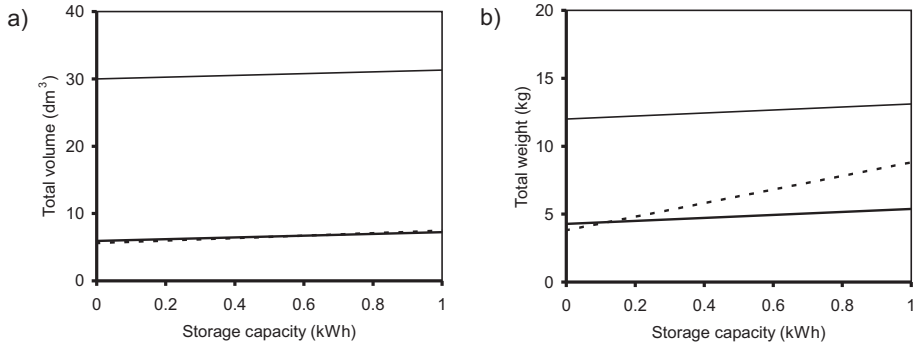

Figure 7.7: Total system volume (a) and weight (b) for three 100 W fuel cell systems: a PEMFC [24] with metal hydride canisters [25] (dotted line), a DMFC [26] with a methanol tank (thin line), and a PEMFC with fuel processor and a methanol tank (thick line).

actor in the microstructured design. As a consequence, the micro heat exchanger designs are influenced by heat transfer to the adjacent reactor and by a fixed plate width, which is determined by the width of the reactor, while the conventional heat exchangers are not. These disadvantages are compensated by a reduction in the amount of insulation needed for the ProxHeatex device. Nevertheless, comparing the designs shows that the difference between conventional and micro technology is smaller for the heat exchangers than for the reactors, which is expected, since compact plate-fin heat exchangers and microstructured heat exchangers are similar in construction.

7.6.3 Comparison to existing fuel cell systems

The total volume and mass of the RefBurn and ProxHeatex units added together are 0.17 dm^3 and 0.24 kg, respectively, for a 100 W_e fuel processor, and 5.4 dm^3 and 13 kg for a 5 kW_e fuel processor. How do these numbers compare with real fuel cell systems? Figure 7.7 shows the size and weight of three different 100 W_e fuel cell systems: a H_2 fuelled proton exchange membrane fuel cell (PEMFC) with a metal hydride canister (50% efficiency), a direct methanol fuel cell (DMFC) with a methanol tank (16% efficiency), and a PEMFC with a fuel processor and a methanol/water tank (35% efficiency). Data regarding the size and weight of the fuel cells and storage tanks are obtained from commercially available units [24–26] and scaled to 100 W. The size and weight of

a real fuel processor are estimated to be twice the calculated size and weight of the two reactor devices.

The figure shows that a PEM fuel cell system is smaller and lighter than a DMFC system and that the fuel processor unit is relatively small and light compared to the two fuel cell systems. However, it is expected that fuel cells will still become considerably smaller within the next years. For example, Toshiba has already shown a direct methanol fuel cell prototype for a notebook computer that weighs only 1 kg and has a power output of 20 W [27], but has not yet commercialized this product. The use of a fuel processor shows no advantage in system size over hydrogen storage in metal hydrides, but does show a benefit when comparing system weight. However, the question will be to what extent the weight advantage of using a fuel processor will outweigh the added costs and complexity of a fuel processor system.

7.7 Conclusions

System designs of the RefBurn reactor and ProxHeatex device are compared for conventional fixed-bed reactor technology and microreactor technology on 100 W_e and 5 kW_e power output scales. The fixed-bed reactors are designed using a two-dimensional pseudo-homogeneous model including heat transfer resistances in the catalyst bed and at the tube walls and including mass transfer resistance in the catalyst pellets. The microreactors are designed using dedicated microreactor models including heat conduction in the microstructured plates and mass transfer limitations in the coated catalyst layer. Fixed criteria are used for reactor conversion, maximum reactor temperature, and pressure drop. In this way, differences in heat and mass transfer characteristics will show up as differences in the required catalyst mass and ultimately in the system's size and weight.

On both power output scales studied, the microreactor designs outperform the conventional designs, leading to lower reactor volumes and weights. The scaling factors of the reactor volume and weight are larger for the microreactor systems as for the conventional systems, indicating that at larger scales fixed-bed reactors will ultimately outperform the microreactor designs. The designs are specifically made for a fuel processor system for portable power generation, which asks for small-scale, highly integrated reactors, which limits the validity of the results to this specific case. However, this study does

show that microreactor technology may be a viable alternative for conventional reactors for the design of small-scale reactors in which heat exchange is important. Furthermore, the use of a fuel processor and fuel cell system shows a clear weight benefit over other fuel cell systems in applications where a large energy storage capacity is required.

Nomenclature

Abbreviations

burn	burner side
cool	coolant side
DMFC	direct methanol fuel cell
HTEX	high temperature heat exchanger
LTEX	low temperature heat exchanger
PEMFC	proton exchange membrane fuel cell
Prox	preferential oxidation
ProxHeatex	preferential oxidation – heat exchanger device
ref	reformate side
RefBurn	reformer – burner device

Symbols

A	heat transfer surface (m^2)
c_p	heat capacity (J mol^{-1} K^{-1})
C_{CO}	carbon monoxide concentration (mol m^{-3})
C_{MeOH}	methanol concentration (mol m^{-3})
d_{cat}	diameter of catalyst pellet/layer (m)
$\underline{D}_e$	effective diffusivity (m^2 s^{-1})
$\underline{G}_r$	reformate gas mass flux (kg m^{-2} s^{-1})
ΔH	reaction enthalpy (J mol^{-1})
$\underline{k}_e$	effective bed conductivity (W m^{-1} K^{-1})
M	molar mass (kg mol^{-1})
R	gas constant (J mol^{-1} K^{-1})
R_{CO}	rate of carbon monoxide oxidation (mol m_{cat}^{-3} s^{-1})
R_{MeOH}	rate of methanol reforming (mol m_{cat}^{-3} s^{-1})
R_V	volumetric reaction rate (mol m^{-3} s^{-1})
T	reaction temperature (K)
U	heat transfer coefficient (W m^{-2} K^{-1})
V	system volume (m^3)
β	scaling factor (-)
η_{cat}	catalyst effectiveness factor (-)
κ_t	thermal conductivity of the tube material (W m^{-1} K^{-1})

ρ	density (kg m^{-1})
ω_{CO}	mass fraction of CO (-)

Acknowledgement

The authors gratefully acknowledge funding from the European Commission for the Micro Reactor Technology for Hydrogen and Electricity (MiRTH-e) project under the 'Energy, Environment and Sustainable Development' Programme, contract number ENK6-CT-2000-00110.

Bibliography

[1] H. Löwe and W. Ehrfeld. State-of-the-art in microreaction technology: concepts, manufacturing and applications. *Electrochim. Acta*, 44:3679–3689, 1999.

[2] K. F. Jensen. Microreaction engineering — is small better? *Chem. Eng. Sci.*, 56:293–303, 2001.

[3] V. Hessel, S. Hardt, and H. Löwe. *Chemical Micro Process Engineering — Fundamentals, Modelling and Reactions*. Wiley-VCH, Weinheim, Germany, 2004.

[4] H. Kestenbaum, A. Lange de Oliveira, W. Schmidt, F. Schüth, W. Ehrfeld, K. Gebauer, H. Löwe, T. Richter, D. Lebiedz, I. Untiedt, and H. Züchner. Silver-catalyzed oxidation of ethylene to ethylene oxide in a microreaction system. *Ind. Eng. Chem. Res.*, 41:710–719, 2002.

[5] J. Antes, D. Boskovic, H. Krause, S. Loebbecke, N. Lutz, T. Tuercke, and W. Schweikert. Analysis and improvement of strong exothermic nitrations in microreactors. *Chem. Eng. Res. Des.*, 81:760–765, 2003.

[6] J. M. Commenge. *Réacteurs Microstructurés: Hydrodynamique, Thermique, Transfert de Matière et Applications aux Procédés*. PhD thesis, Institut National Polytechnique de Lorraine, Nancy, France, 2001.

[7] E. R. Delsman, E. V. Rebrov, M. H. J. M. de Croon, J. C. Schouten, G. J. Kramer, V. Cominos, T. Richter, T. T. Veenstra, A. van den Berg, P. D. Cobden, F. A. de Bruijn, C. Ferret, U. d'Ortona, and L. Falk. MiRTH-e: Micro Reactor Technology for Hydrogen and Electricity. In M. Matlosz, W. Ehrfeld, and J. P. Baselt, editors, *Proceedings of the Fifth International Conference on Microreaction Technology*, pages 268–274. Springer Verlag, Berlin, Germany, 2001.

[8] B. A. Peppley, J. C. Amphlett, L. M. Kearns, and R. F. Mann. Methanol–steam reforming on $Cu/ZnO/Al_2O_3$. part 1: The reaction network. *Appl. Catal. A: Gen.*, 179:21–29, 1999.

[9] B. A. Peppley, J. C. Amphlett, L. M. Kearns, and R. F. Mann. Methanol–steam reforming on $Cu/ZnO/Al_2O_3$. part 2: A comprehensive kinetic model. *Appl. Catal. A: Gen.*, 179:31–49, 1999.

[10] C. Horny, L. Kiwi-Minsker, and A. Renken. Micro-structured string-reactor for autothermal production of hydrogen. *Chem. Eng. J.*, 101:3–9, 2004.

[11] P. J. de Wild, M. J. F. M. Verhaak, and D. F. Bakker. *Catalysts for the selective oxidation of carbon monoxide in hydrogen-containing gases*, 2000. International Patent WO 00/17097.

[12] M. J. Kahlich, H. A. Gasteiger, and R. J. Behm. Kinetics of the selective CO oxidation in H_2-rich gas on Pt/Al_2O_3. *J. Catal.*, 171:93–105, 1997.

[13] Aspen Technology Inc. *Aspen Plus®, version 11.1*. Cambridge, USA, 2001.

[14] J. Taborek. *Heat Exchanger Design Handbook*, chapter 3.3 Shell-and-Tube Heat Exchangers: Single-Phase Flow. Begell House, Inc., New York, 1998.

[15] E. R. Delsman, M. H. J. M. de Croon, A. Pierik, G. J. Kramer, P. D. Cobden, C. Hofmann, V. Cominos, and J. C. Schouten. Design and operation of a preferential oxidation microdevice for a portable fuel processor. *Chem. Eng. Sci.*, 59:4795–4802, 2004.

[16] G. F. Froment and K. B. Bischoff. *Chemical reactor analysis and design*. Wiley, Chichester, USA, 2nd edition, 1990.

[17] E. R. Delsman, M. H. J. M. de Croon, G. J. Kramer, P. D. Cobden, C. Hofmann, V. Cominos, and J. C. Schouten. Experiments and modelling of an integrated preferential oxidation – heat exchanger microdevice. *Chem. Eng. J.*, 101:123–131, 2004.

[18] R. L. Webb. *Heat Exchanger Design Handbook*, chapter 3.9 Compact Heat Exchangers. Begell House, Inc., New York, 1998.

[19] S. Yagi and N. Wakao. Heat and mass transfer from wall to fluid in packed beds. *AIChE Journal*, 5:79–85, 1959.

[20] S. Yagi and D. Kunii. Studies on heat transfer near wall surface in packed beds. *AIChE Journal*, 6:97–104, 1960.

[21] Comsol AB. *Femlab®, version 2.3b*. Stockholm, Sweden, 2003.

[22] W. Beitz and K.-H. Küttner, editors. *Dubbel: Handbook of Mechanical Engineering*. Springer-Verlag, London, UK, 1994. English ed. B. J. Davies, transl. M. J. Shields.

[23] E. R. Delsman, A. Pierik, M. H. J. M. de Croon, G. J. Kramer, and J. C. Schouten. Microchannel plate geometry optimization for even flow distribution at high flow rates. *Chem. Eng. Res. Des.*, 82:267–273, 2004.

[24] Ball Aerospace & Technologies Corp. PPS-100 PEM fuel cell (100 W, 5.6 dm^3, 3.8 kg). http://www.ballaerospace.com/pps100.html, 2005.

[25] Ovonic Hydrogen Systems LLC. Model 85G250 metal hydride canister (1.3 kWh, 2.4 dm^3, 6.5 kg). http://www.ovonic-hydrogen.com/-products/portable.htm, 2005.

[26] SFC Smart Fuel Cell AG. SFC A50 direct methanol fuel cell (50 W, 15 dm^3, 6 kg). http://www.smartfuelcell.com/en/produkte/sfc_a50.html, 2005.

[27] Toshiba Corporation. Direct Methanol Fuel Cell for portable PCs (20 W, 0.83 dm^3, 0.9 kg). http://www.toshiba.co.jp/about/press/2003_03/-pr0501.htm, 2003.

8 Conclusion

Conclusions

Microreactors are miniaturized chemical reaction systems, which contain reaction channels with a typical diameter of 10 to 500 µm. The small channel dimensions of microreactors result in a relatively large surface area-to-volume ratio and increased driving forces for heat and mass transport, which makes microreactors especially suited for performing fast reactions with a large heat effect. Microreactors also show large promise in the development of miniature chemical devices, where several unit operations are integrated with microstructured sensors and actuators to form a micro chemical plant. These miniaturized chemical devices offer opportunities for small scale fuel processing and portable power generation, for example to replace battery packs in laptops and mobile phones. In a fuel processor, a liquid or gaseous fuel, like methanol or methane, is converted to hydrogen, which is then used in a fuel cell to generate electricity. Such a system offers a five to tenfold improvement in energy storage capacity compared to state-of-the-art batteries.

In this study, a 100 W-electric methanol fuel processor is designed, based on a pinch analysis, that consists of three microstructured, heat-integrated devices in series: a vaporizer–exhaust gas cooler, a reformer–burner, and a preferential oxidation–heat exchanger device. The calculated efficiency of the conversion of primary fuels to electricity for low-power applications, is 20% for the studied fuel processor and fuel cell system, which is in-between the efficiency for batteries (40%) and for combustion engines (10%). The methanol production process contributes most to the overall exergy loss of the methanol fuel processor and fuel cell process (55%), compared to 20% for the fuel processor and 25% for the fuel cell itself.

The design and manufacture of two prototype microdevices provided increased understanding of microreactor modelling and design. It was found that the flow distribution chambers are not only important for flow equipartition, but they also significantly influence the heat transfer characteristics. Furthermore, the heat exchanger efficiency is negatively affected by axial heat conduction through the heat exchanger material, favoring low-conductive materials for the construction of micro heat exchangers. Moreover, heat losses to the environment, also through the connective tubing, and insulating adjacent parts of the device operating at different temperature levels, provide specific challenges for microreactor design, due to the small geometric dimensions involved. The final microdevice that was constructed, was able to reduce the carbon monoxide concentration in a hydrogen-rich methanol reformate gas from 0.5% to 10 ppm, the level required for a proton exchange membrane fuel cell. The device integrates two heat exchangers and a reactor–heat exchanger in a single device with a volume and mass of only 60 cm^3 and 150 g, respectively, and reaches a heat recovery of 90%.

A modelling approach was developed for the design of the microstructured reactor–heat exchanger device that divides the modelling effort into modelling of the fluid flow, to establish equipartition of the flow over the individual channels, and modelling of the heat transfer, to establish the desired temperature profile in the heat exchangers and reactor and to avoid temperature differences between the channels. The calculation time of the heat transfer models was drastically reduced by using a volume averaging approach for describing the convective heat transport by the flowing gases and the conductive heat transport in the microstructured plates. The modelling approach proved well-suited for the design of a microstructured reactor–heat exchanger and provided an accurate prediction of the experimentally determined temperature profiles in the manufactured microdevice.

The three-dimensional fluid dynamics simulations of the distribution of fluid flow over a set of parallel microchannels showed that two distinct flow regimes exist depending on the gas inlet velocity. At low flow rates the flow distribution is completely determined by wall friction and the distribution's relative standard deviation is independent of the flow rate. At flow rates above a transitional velocity, which value is geometry dependent, inertia effects start to influence the flow distribution. Although the flow regime is laminar in all cases studied, the significant entrance flow effects prohibit the use

of a two-dimensional model. An improved microchannel plate design is obtained by reducing the plate width, by maximizing the width of the inlets and outlets, and by situating the inlets and outlets in-line with the channels.

Based on elementary statistics, equations were derived that express the microreactor conversion explicitly as a function of the variance of a number of channel parameters, viz. the channel flow rate, the channel diameter, the amount of catalyst in a channel, and the channel temperature. These equations allow for the quick estimation of the influence of flow maldistribution and manufacturing tolerances on the ultimate performance of a microreactor. In general, the influence of small variations in the channel flow rate and channel diameter on the reactor conversion is limited, since a lower conversion in one part of the channels is compensated by a higher conversion in the other channels. However, for variations in the catalyst coating thickness and in the channel temperature, the effect on the reactor conversion is significant ($> 10\%$).

Finally, conventional fixed-bed reactor technology and microreactor technology were compared in a design study, which shows that, on 100 W_e and 5 kW_e power output scales, the microreactor designs of the reformer–burner reactor and the preferential oxidation device outperform the conventional designs, leading to lower reactor volumes and weights. The total volume of both reactor devices can be reduced to 55 cm^3 for the 100 W_e and 5 dm^3 for the 5 kW_e output scale. Since the designs were specifically made for a fuel processor system for portable power generation, which requires small-scale, highly integrated reactors, the validity of the results is limited. However, this study does show that microreactor technology may be a viable alternative for conventional reactors for the design of small-scale reactors in which heat exchange is important.

Outlook

Fuel cell systems are a promising alternative for battery systems and combustion engines for supplying portable power. However, looking at the overall energy efficiency, fuel cells do outperform combustion engines, but cannot compete with the state-of-the-art batteries. Nevertheless, since fuel cells combine the energy storage capacity of combustion engine systems with the noise and pollution levels of batteries, fuel cells are interesting for specific applica-

tions, for example in auxiliary power units in trucks or sailing yachts, or in autonomous battery recharging units. At the moment, direct fuel cell systems seem to be favored above a fuel processor and fuel cell combination, since it avoids the added complexity of the fuel processor. Both direct hydrogen and methanol fuel cell systems are being developed. The success of these technologies will depend on the development of an efficient and safe hydrogen storage method and on how much the performance of the direct methanol fuel cell can be increased.

Microreactors are more expensive than most conventional reactors and their use involves additional risks, like pore plugging, corrosion or erosion of the reactor material, and a lack of experience with their long-term operation. Therefore, microreactors will only be introduced successfully, when they offer a clear benefit, for instance when a marked improvement in selectivity and yield can be obtained, as a result of the extreme mixing or nearly perfect temperature control in microreactors, or by allowing operation within the explosive regime. However, many reactions, especially those used in fine chemistry, are too slow for a microreactor to be an interesting option, although examples exist where the reaction rate was significantly increased by allowing the reaction to proceed at a much higher temperature than would be possible in a large stirred vessel. Other areas where microreactors offer interesting possibilities are in the improvement of process safety, by replacing large vessels of dangerous chemicals by small microreactors, and in the development of small-scale chemical process units, like a stand-alone nitrous oxide generation and destruction unit for hospital use. Definitely, due to their unique properties, microreactors are a valuable addition to the chemical engineering toolbox.

A large part of this thesis is devoted to the development of microreactor design models. Since most previous microreactor work focusses on building prototypes only, much work remains to be done on microreactor modelling. In the area of fluid dynamics modelling, it is necessary to develop models to describe the distribution of fluid flow over multiple microstructured plates, which might then lead to the development of a general-use multi-scale architecture for the distribution of fluid flow over a multitude of microchannels. Furthermore, the presented heat transfer models should be expanded to three dimensions also including the effect of heat transfer in the connecting tubing. The manufacture of new microreactor prototypes will remain important for validation of the modelling work and for the identification of practical obsta-

cles. In particular, the choice in different construction materials, and thus the choice in heat conductivity, should be increased. Furthermore, work should be done on the integration of these different materials in a single device and on developing ways to insulate device parts that operate at different temperatures.

Dankwoord / Word of thanks

Met dit boekje komt er een einde aan een lange tijd die ik in Eindhoven heb doorgebracht, zowel voor mijn promotieonderzoek als in mijn scheikundestudie daarvoor. Ik zal met weemoed terugdenken aan een tijd waarin ik onnoemelijk veel mensen heb leren kennen en die met recht als een van de mooiste van mijn leven zal zijn. Omdat ik mijn promotie nooit had kunnen afronden zonder de hulp van vele mensen, wil ik hen hier graag bedanken.

Als eerste mijn directe begeleiders, Mart de Croon en Jaap Schouten. Mart, we hebben veel tijd samen doorgebracht, discussiërend, formules afleidend, discussiërend. Behalve van je enorme kennis op het gebied van reactorkunde en wiskunde, heb ik ook dankbaar gebruik mogen maken van je standvastige goedgehumeurdheid, je kookkunsten en je wijnkamer. Jaap, jou wil ik bedanken voor de manier waarop je mij hebt leren schrijven en presenteren (komma), en me hebt laten ontdekken dat zelfstandig onderzoek doen niet alleen te maken heeft met experimenteren en rekenen, maar ook met plannen en keuzes maken. Hier wil ik ook Gert Jan Kramer niet ongenoemd laten, die mij, steeds wanneer hij bij de werkbesprekingen aanwezig was, scherp wist te houden door zijn vinger op een aantal zwakke plekken te leggen.

This project would not have been possible without the contributions and enthusiasm of all MiRTH-e project partners. I want to address a special thanks to Vania Cominos, Christian Hofmann, and Volker Hessel, who have used all their fine skills, knowledge, and resources to design and fabricate the microreactor prototypes for this project. Also a special thanks to Paul Cobden and Gerard Elzinga, who have invested a large amount of time to overcome the problems associated with the coating of etched microstructured plates and to apply the catalyst coatings to the hundreds of microchannel plates. In addition I want to thank Theo Veenstra, Cédric Ferret, Frank de Bruijn, Umberto d'Ortona, and Laurent Falk, for their inputs during the project meetings and the good atmosphere during lunches, dinners, and bar-visits. Finally, the

European Commission is gratefully acknowledged for funding the MiRTH-e project.

Wat is onderzoek zonder een goede ondersteuning? Daarom wil ik Jovita Moerel, Hans Huisman, Herbert Fiedler, Paul Aendenroomer, en de overige mensen bij de GTD bedanken voor het uitwerken, bouwen en onderhouden van een prachtige experimentele opstelling. Verder ook Anton Bombeeck, Frank Grootveld, Madan Bindraban en Chris Luijk voor de technische ondersteuning vanuit de groep. Dank ook aan Marlies Coolen-Kuppens voor haar analysespecialisme, Ton Sommen voor de adsorptiemetingen, Wim Groenland voor de koffie en Denise Tjallema-Dekker voor haar ondersteuning en aansporingen tijdens de afronding van het proefschrift. Verder wil ik Evgeny Rebrov bedanken voor zijn betrokkenheid aan het begin van het project en Krzysztof Ptasinski voor de samenwerking tijdens het afstudeerproject van Charles Uju en het omwerken van de resultaten tot een artikel.

Graag bedank ik hier ook Els en Bruce voor hun mentale ondersteuning en hun hulp bij het managen van eerst mijzelf en daarna het project.

Een alinea wil ik zeker ook wijden aan de mensen die een groot deel van het werk hebben gedaan, te weten alle afstudeerders, Mark, Arno, Jolmer, Charles, Anke en Bart, en mijn enige stagair Remco. Bedankt voor jullie inzet en doorzettingsvermogen, en de gezelligheid op het lab en in de koffiekamer. Ik hoop dat ik jullie iets heb kunnen leren. In ieder geval heb ik veel van jullie geleerd.

Verder wil ik ook Jos Noijen en Madan Bindraban bedanken, die mij op het laatste moment uit de brand geholpen hebben met het ontwerpen van de kaft.

Dat ik een geweldige tijd heb gehad in Eindhoven is vooral ook te danken aan mijn collega's: Poul, Mies, Vikrant, Karen, Jeroen, Keshav, Evgeny, John, Jozef, Ben, Eric, Ilias, Charl, Vinit, Yogi, Maurice en Oki. Naast gezelligheid op het werk was er ook gezelligheid buiten het werk op cursussen, congressen, vakgroepsuitjes, bruiloften en partijen, Lagaan, etentjes, cricket, vodka en kaviaar.

Ook wil ik mijn vrienden niet vergeten die gezorgd hebben en nog altijd zorgen voor de broodnodige afleiding: Armin en Jürgen voor onze prachtige

vakanties naar de bergen en samen met Roger en Maurice voor Chinezen en Catan. Meine lieben Stiefelfreunden, die nicht nur gut spaß machen können, aber auch immer ein guter Schalldeckel gewesen sind. Mechiel, Tatiana, Heck, Jeroen, Robbert, Erik en Jim, die naast Saskia's vrienden ook mijn vrienden zijn geworden, de Horn-groep, iedereen van het laagste volleybalteam van Hajraa, Groove Connexion, mijn oud-huisgenoten en oud-oud-huisgenoten.

Pa, Ma, Joost en Martin, bedankt voor jullie liefde, steun en humor. Ook al zie ik jullie veel te weinig, het zijn altijd mooie momenten als we weer bij elkaar zijn. Zoals het klokje... Tevens wil ik Saskia's ouders bedanken, aangezien ik ook altijd bij hen terecht heb gekund. En Martijn: veel succes in je nieuwe leventje.

Mijn grootste dank gaat uit naar Saskia. Je bent me altijd blijven steunen en je hebt me er op de moeilijke momenten doorheen getrokken. Zonder jouw vertrouwen in mij was ik nooit zo ver gekomen.

Erik Delsman

31 maart 2005

List of Publications

Journal publications

1. E. R. Delsman, M. H. J. M. de Croon, G. D. Elzinga, P. D. Cobden, G. J. Kramer, and J. C. Schouten. The influence of differences between microchannels on microreactor performance. *Chem. Eng. Technol.*, 28:367–375, 2005.
2. E. R. Delsman, C. U. Uju, M. H. J. M. de Croon, , J. C. Schouten, and K. J. Ptasinski. Exergy analysis of an integrated fuel processor and fuel cell system. *Energy Int. J.*, 2005. Submitted for publication.
3. E. R. Delsman, B. J. P. F. Laarhoven, M. H. J. M. de Croon, , G. J. Kramer, and J. C. Schouten. Comparison between conventional fixed-bed and microreactor technology for a portable hydrogen production case. *Chem. Eng. Res. Des.*, 2005. Submitted for publication.
4. E. R. Delsman, M. H. J. M. de Croon, G. J. Kramer, P. D. Cobden, C. Hofmann, V. Cominos, and J. C. Schouten. Experiments and modelling of an integrated preferential oxidation – heat exchanger microdevice. *Chem. Eng. J.*, 101:123–131, 2004.
5. E. R. Delsman, A. Pierik, M. H. J. M. de Croon, G. J. Kramer, and J. C. Schouten. Microchannel plate geometry optimization for even flow distribution at high flow rates. *Chem. Eng. Res. Des.*, 82:267–273, 2004.
6. E. R. Delsman, M. H. J. M. de Croon, A. Pierik, G. J. Kramer, P. D. Cobden, C. Hofmann, V. Cominos, and J. C. Schouten. Design and operation of a preferential oxidation microdevice for a portable fuel processor. *Chem. Eng. Sci.*, 59:4795–4802, 2004.
7. M. H. J. M. de Croon, E. R. Delsman, P. van Male, E. V. Rebrov, and J. C. Schouten. Challenging prospects for micro structured reaction architectures (2). *NPT Procestechnologie*, 5:23–24, 2003.

Conference proceedings

1. E. R. Delsman, C. U. Uju, M. H. J. M. de Croon, , J. C. Schouten, and K. J. Ptasinski. Exergy analysis of an integrated fuel processor and fuel cell system. In R. Rivero, L. Monroy, R. Pulido, and G. Tsatsaronis, editors, *Proceedings of the 17th International Conference on Efficiency, Costs, Optimization,*

Simulation and Environmental Impact of Energy and Process Systems (ECOS 2004), pages 669–677. Guanajuato, Mexico, 2004.

2. E. R. Delsman, M. H. J. M. de Croon, C. Hofmann, V. Cominos, P. D. Cobden, G. J. Kramer, and J. C. Schouten. Development of a microstructured preferential co oxidation reactor – heat exchanger device for a portable methanol fuel processor. In A. Varma, B. Subramanian, and K. Vandenbussche, editors, *Proceedings of the 18th International Symposium on Chemical Reactor Engineering (ISCRE-18),* Session 2, no. 2. Chigaco, USA, 2004.
3. V. Cominos, V. Hessel, C. Hofmann, G. Kolb, H. Löwe, R. Zapf, E. R. Delsman, M. H. J. M. de Croon, and J. C. Schouten. Selectve oxidation in a microreactor for low power fuel cell applications. In *Proceedings of the 226th ACS National Meeting*, CATL-043. New York, USA, 2003.
4. E. R. Delsman, C. Hofmann, V. Cominos, P. D. Cobden, M. H. J. M. de Croon, and J. C. Schouten. Design of an integrated microstructured reactor – heat exchanger: a selective co oxidation device for a portable fuel processor. In *Proceedings of the 7th International Conference on Microreaction Technology (IMRET 7)*, pages 74–76. Lausanne, Switzerland, 2003.
5. E. R. Delsman, M. H. J. M. de Croon, and J. C. Schouten. Miniaturization of a co preferential oxidation device for small scale fuel cell applications. In Paper presented at the *Netherlands Process Technology Symposium (NPS 4)*. Veldhoven, the Netherlands, 2003.
6. V. Cominos, V. Hessel, C. Hofmann, G. Kolb, H. Löwe, R. Zapf, E. R. Delsman, M. H. J. M. de Croon, and J. C. Schouten. Fuel processing in micro-reactors for low power fuel cell applications. In *Proc. of the 27th Int. Exhibition-Congress on Chemical Engineering, Environmental Protection and Biotechnology (ACHEMA 2003)*, page 9. Frankfurt, Germany, 2003.
7. E. R. Delsman, C. Hofmann, V. Cominos, P. D. Cobden, T. T. Veenstra, A. van den Berg, M. H. J. M. de Croon, and J. C. Schouten. Integration of selectve co oxidation and heat exchange in a microstructured reactor as part of a portable fuel processor. In *Proceedings of the 3rd International Symposium on Multifunctional Reactors (ISMR 3)*, pages 242–245. Bath, United Kingdom, 2003.
8. E. R. Delsman, E. V. Rebrov, M. H. J. M. de Croon, J. C. Schouten, G. J. Kramer, V. Cominos, T. Richter, T. T. Veenstra, A. van den Berg, P. D. Cobden, F. A. de Bruijn, C. Ferret, U. d'Ortona, and L. Falk. MiRTH-e: Micro Reactor Technology for Hydrogen and Electricity. In M. Matlosz, W. Ehrfeld, and J. P. Baselt, editors, *Proceedings of the Fifth International Conference on Microreaction Technology*, pages 268–274. Springer Verlag, Berlin, Germany, 2001.

About the author

Erik Delsman was born in Amsterdam on June 12th, 1976. He obtained his 'VWO' highschool certificate at the Dr. Mollercollege in Waalwijk in 1994, after which he continued his education at the Eindhoven University of Technology for a study in chemical engineering. In 2000 he obtained his M.Sc. degree, cum laude, on the topic of 'Modelling the Micellarly Catalyzed Epoxidation of Propylene' in the group of prof.dr.ir. J.T.F. Keurentjes. In the same year he started his Ph.D. Research at the Laboratory of Chemical Reactor Engineering of the Eindhoven University of Technology, under supervision of dr. M.H.J.M. de Croon and prof.dr.ir. J.C. Schouten. In January 2005 Erik accepted a position as technology development engineer at GE Advanced Materials in Bergen op Zoom.